

2007

Studies of laser-based, solid freeform fabrication and coating processes using nanoscale and functionally-graded materials

Rajeev Madhavan Nair
Iowa State University

Follow this and additional works at: <http://lib.dr.iastate.edu/rtd>



Part of the [Mechanical Engineering Commons](#)

Recommended Citation

Madhavan Nair, Rajeev, "Studies of laser-based, solid freeform fabrication and coating processes using nanoscale and functionally-graded materials" (2007). *Retrospective Theses and Dissertations*. 15491.
<http://lib.dr.iastate.edu/rtd/15491>

This Dissertation is brought to you for free and open access by Iowa State University Digital Repository. It has been accepted for inclusion in Retrospective Theses and Dissertations by an authorized administrator of Iowa State University Digital Repository. For more information, please contact digirep@iastate.edu.

**Studies of laser-based, solid freeform fabrication and coating processes using nanoscale
and functionally-graded materials**

by

Rajeev Madhavan Nair

A dissertation submitted to the graduate faculty
in partial fulfillment of the requirements for the degree of

DOCTOR OF PHILOSOPHY

Major: Mechanical Engineering

Program of Study Committee:
Pal Molian (Major Professor)
Abhijit Chandra
Shankar Subramaniam
Pranav Shrotriya
Frank Peters

Iowa State University

Ames, Iowa

2007

Copyright © Rajeev Madhavan Nair, 2007. All rights reserved.

UMI Number: 3259433



UMI Microform 3259433

Copyright 2007 by ProQuest Information and Learning Company.
All rights reserved. This microform edition is protected against
unauthorized copying under Title 17, United States Code.

ProQuest Information and Learning Company
300 North Zeeb Road
P.O. Box 1346
Ann Arbor, MI 48106-1346

Dedication

I dedicate this dissertation to my mother Mrs. Ratnakutty Amma and father Mr. Madhavan Nair. Without their patience, understanding, support, and most of all love, the completion of this work would not have been possible.

TABLE OF CONTENTS

LIST OF FIGURES	vii
LIST OF TABLES	xii
ACKNOWLEDGEMENTS	xiii
ABSTRACT	xv
CHAPTER 1. Introduction	1
1.1 Dissertation organization	2
CHAPTER 2. Background	4
2.1 Solid Freeform Fabrication	4
2.2 Lasers for Rapid Prototyping	12
2.3 Dies and Molds	14
2.4 Functionally Graded Materials	17
2.5 Nanoparticles	19
CHAPTER 3. Nanoparticle Additive Manufacturing of Ni/H13 Steel Injection Molds	31
3.1 Introduction	31
3.2 Background	33
3.3 Experimental Procedure	35
3.3.1 Materials	35
3.3.2 Mold Design	36
3.3.3 Powder Feeding	37
3.4 NAM Process	38
3.5 Characterization and Testing	40

3.6 Results and Discussion	41
3.6.1 Analysis of Molds	41
3.6.2 Solidification Structures of Molds	43
3.6.3 Composition and Microstructure of Molds	45
3.6.4 Hardness and Corrosion Resistance	47
3.6.5 Injection Molding Data	49
3.7 Conclusions	50
CHAPTER 4. Functionally Graded Mold Inserts by Laser-based Flexible	55
Fabrication: Processing Modeling, Structural Analysis, and Performance	
Evaluation	
4.1 Introduction	55
4.2 Experimental Materials and Methods	58
4.3 Process Modeling	60
4.3.1 Problem description	60
4.3.2 Solution	61
4.4 Results and Discussion	62
4.4.1 The square mold insert fabricated by LBFF	62
4.4.2 Surface thermal gradient profiles of shaped beams	62
4.4.3 Cooling rate	63
4.4.4 Solidification microstructures	63
4.4.5 Performance evaluation	66
4.5 Conclusions	66

CHAPTER 5. Preparation and Characterization of Diamond-like Carbon	80
Coating on Aluminum 6061 T-91 Substrate using Laser Sintering	
5.1 Introduction	81
5.2 Experimental Procedure	84
5.2.1 Aluminum substrate	84
5.2.2 Preparation of Nano-diamond Powders	84
5.2.3 Electrostatic Spray Coating (ESC) Process	86
5.2.4 Laser Sintering Process	88
5.2.5 Measurements and Sample Characterization	91
5.3 Results	91
5.3.1 Effects of Laser Parameters	91
5.3.2 Micro-hardness	92
5.3.3 Fracture toughness	94
5.3.4 Surface Roughness	96
5.3.5 Scratch test	97
5.3.6 Raman Spectroscopy	101
5.3.7 Microstructure & Surface Morphology	105
5.3.8 X-ray Diffraction (XRD)	106
5.4 Discussion	108
5.5 Conclusions	112
CHAPTER 6. Thermal Transport Analysis of Laser Sintering of	120
Nanocrystalline Diamond Powders	
6.1 Introduction	121

6.2	Experimental procedure and results	124
6.3	Thermal energy transport model description	126
6.3.1	Properties of Powder Bed, Substrate and Assist Gas	126
6.3.2	Energy Input Sub-model	130
6.3.3	Heat transfer Sub-model	132
6.3.4	Finite Element Solution Procedures	135
6.4	Results and Discussion	137
6.4.1	One-dimensional steady state results	137
6.4.2	One-dimensional transient state results	141
6.4.3	Stress calculations	147
6.5	Conclusions	148
	CHAPTER 7. General Conclusions and Future Work	155
	APPENDIX A. Laser-Based, Solid Freeform Fabrication Facility	158
	APPENDIX B. Powder Delivery System Design and Powder Delivery Rate	160
	Calibration	
B.1	Design of powder delivery system	160
B.2	Calibration of powder delivery rate	161

LIST OF FIGURES

Figure 2.1	Schematic showing a 3-D model representation, slicing and process planning, and material additive process in SFF	5
Figure 2.2	Window of laser power density and interaction time suitable for material processing applications	14
Figure 2.3	A flow chart showing the process plan for conventional manufacturing of dies and molds	16
Figure 2.4	Comparison of nanocoatings and other commercial coatings	20
Figure 3.1	Schematic of nanoparticle additive manufacturing of two layers	33
Figure 3.2	(A) Nickel nanopowders, (B) A schematic of mold geometry	36
Figure 3.3	A schematic for the NAM process	39
Figure 3.4	(A) Photographs of Ni/H13 steel mold, (B) H13 steel mold	42
Figure 3.5	Scanning Electron Micrographs (SEM) of H13-Nickel nanocomposite gear mold (A) Single clad track, (B) Equiaxed cellular structure at the top, (C) Columnar dendrite in the middle, (D) Fine epitaxial growth at the bottom (interface)	44
Figure 3.6	Optical micrographs of heavily-etched samples showing the cellular-dendrite structures	45
Figure 3.7	Low and high magnification SEM micrographs showing the	46

	dispersion of nanoparticles in the steel matrix	
Figure 3.8	(A) SEM micrograph showing the nanoparticle, (B) EDAX spectrum of the black nanoparticle (solid line)	47
Figure 3.9	Grain structure of nanocomposite mold	47
Figure 3.10	(A) Rockwell hardness C scale for H13 and H13/Ni nano molds, (B) Variation of microhardness with distance from the top surface of single-layer mold of about 0.4 mm	48
Figure 3.11	Weight loss of molds with immersion time in 10% HCl	49
Figure 4.1	Schematic showing the LBFF process	71
Figure 4.2	The meshes used for surface thermal gradient computations for: (A) circular beam (CB), (B) rectangular beam (RB)	72
Figure 4.3	Photo illustrating a square functionally graded mold insert fabricated using LBFF	73
Figure 4.4	Surface thermal gradient profile of: (A) rectangular beam (RB), (B) circular beam (CB)	74
Figure 4.5	Typical microstructures in: (A) H13 layer, (B) Ni/Cr alloy layer, (C) TiC layer	75
Figure 4.6	SEM showing the interfaces of: (A) H13 and Ni/Cr alloy,	76

	(B) TiC and Ni/Cr alloy	
Figure 4.7	SEM of compositional distribution of the FGM interface of: (A) H13 and Ni/ Cr alloy, (B) TiC and Ni/Cr alloy	77
Figure 4.8	Vickers microhardness (1.0 kgf) profile along the mold insert wall thickness starting from outside	78
Figure 5.1	TEM micrographs of the as-received diamond powder, (A) Lower magnification with a selected area diffraction pattern in the upper right hand corner, (B) High magnification micrograph showing the rounded nature of the grains	86
Figure 5.2	(A) Schematic of the ESC Process, (B) Electrostatic spray coater	87
Figure 5.3	Schematic of the direct laser-sintering process	89
Figure 5.4	Micro-hardness of diamond sintered samples	92
Figure 5.5	Optical micrograph of the substrate cross-section with microhardness Indentations	93
Figure 5.6	Vickers microhardness distribution across the cross-section	94
Figure 5.7	Indentation profile with a Vickers probe	95
Figure 5.8	Average surface roughness of laser-processed samples	96
Figure 5.9	Pictures of delamination for sintered and 'as coated' sample	99
Figure 5.10	Friction force of the sintered sample	100
Figure 5.11	Friction force of the 'as-coated' sample	101

Figure 5.12	Raman Spectra of Nano-diamond Powder	102
Figure 5.13	Raman Spectra of Laser-processed Diamond Sample (200 W, 254 mm/s)	104
Figure 5.14	EDS and SEM micrograph of the laser-sintered sample (200 W, 254 mm/s)	105
Figure 5.15	SEM micrographs of the laser-sintered sample (200 W, 254 mm/s) (A) Coating at 50X magnification, (B) At 300X, etch pits can be seen between the coating and the Substrate, (C) Thin layer of coating with an average thickness of 10 μm , (D) Coating at 7,000X	106
Figure 5.16	XRD diffractogram of the sintered sample	107
Figure 6.1	(A) Schematic, (B) SEM micrograph of the transverse section of the coating	125
Figure 6.2	Three-dimensional representations of the thermal model	134
Figure 6.3	Temperature versus depth profile for a one-dimensional steady state analysis (0.0039 s)	138
Figure 6.4	Temperature versus depth profile for the steady state analysis, from just below the interface to the top of the coating (0.0039 s)	138
Figure 6.5	Phase diagram of ultrafine carbon	140
Figure 6.6	Temperature versus depth profile for the transient analysis (0.0039 s)	143
Figure 6.7	Temperature versus depth profile for the transient analysis, from just below the interface to the top of the coating (0.0039 s)	143

Figure 6.8	Temperature versus time curve for a transient ‘convection free’ model	144
Figure 6.9	Temperature versus time curve for forced convection transient model	144
Figure 6.10	Temperature versus depth plot after the revised analysis	146
Figure 6.11	Thermal stresses developed above and below the coating-substrate interface after heating	147
Figure A.1	A schematic of laser-based solid freeform fabrication process	158
Figure B.1	A schematic showing the design of powder delivery system for laser-based flexible fabrication process	161
Figure B.2	A block diagram of powder calibration	162
Figure B.3	Calibrated results of H-13 powder. (Assisting gas, argon, at flow rate of 10 CFH)	163
Figure B.4	Calibrated results of Ni-Cr composite powder. (Assisting gas, argon, at flow rate of 10 CFH)	163
Figure B.5	Calibrated result inconsistency of Ni-Cr composite powder beyond readings 13. (Assisting gas, argon, at flow rate of 10 CFH)	164

LIST OF TABLES

Table 2.1	A list of additive manufacturing processes (RP)	6
Table 2.2	Durability improvements using nanoparticles	20
Table 2.3	Potential Applications of Nanomaterials	24
Table 2.4	Major suppliers of nanopowders	24
Table 2.5	Nanopowder synthesis methods	25
Table 3.1	Comparison of two powder feeding methods	38
Table 3.2	Process parameters for the fabrication	39
Table 4.1	Density, specific heat, and thermal conductivity of H13 steel	79
Table 4.2	Load Settings of ANSYS for surface thermal gradient computation	79
Table 5.1	Composition of various elements in Aluminum 6061-T91	84
Table 5.2	Basic technical characteristics of the diamond nanopowder	86
Table 5.3	Process Parameters for the Fabrication	90
Table 5.4	Scratch test conditions and procedure	98
Table 5.5	Comparison of coating characteristics produced by laser-sintering (current work) and other methods (previous works)	112
Table 6.1	Optimal Process Parameters	125
Table 6.2	Some thermo-physical properties of the powder bed	128
Table 6.3	Thermo-physical properties of aluminum 6061 T-91	129
Table 6.4	Load Settings used in ANSYS for the steady state analysis	136
Table 6.5	Load Settings used in ANSYS for the transient state analysis	137

ACKNOWLEDGEMENTS

I would like to express my sincere thanks to my major professor, Dr. Molian, for his generous help and support during my Ph.D. study. He has been an example of integrity, patience, and straight talk that I hope to live up to. I would also like to thank Dr. Chandra, Dr. Subramaniam, Dr. Shrotriya, and Dr. Peters for accepting to serve on my committee, and providing advices and constructive comments towards the successful completion of my dissertation.

My special thoughts of gratitude go to my parents who have always believed in me. They have been role models for me and I hope to live up to their expectations. My sister Manju has always encouraged and prayed for me and I am deeply indebted to her. My late grandmother Padmakshi Amma was an abode of love and generosity and I thank her for everything.

I would like to thank Dr. Wenping Jiang for his help and advices during my research. Special thanks should also go to Hal Sailsbury of the Metals Development department of Ames lab, who offered unconditional help with equipments in his lab. I would also like to thank the various technicians and researchers who helped me with my research at various points. Special thanks to Larry Couture and Larry Hanft for their input in my research and assistance in providing materials and post-processing, to Jim Dautremont for his assistance in troubleshooting problems with the various equipment in the research laboratory, and Dr. Warren Straszheim for his assistance in helping me with my SEM work.

Hap Steed and Nate Jensen who are system support specialists in the mechanical engineering department were very helpful with computer related problems and I am grateful to them for all their support. I thank all my friends and well wishers for their prayers and thoughts.

Above all, I thank God almighty for his everlasting love, compassion and mercy.

ABSTRACT

The purpose of this body of investigation is to examine the role of nanoscale and functionally-graded materials on the laser processing and performance of freeform parts and coatings. Both laser experiments and thermal transport models were utilized to achieve the end goal with applications targeted to dies, molds and light-weight aluminum structures. Specifically a computer-numerical-controlled, high-power CO₂ laser system with the aid of computer-aided-design models was used to study: 1) nanoscale material additive manufacturing (NAM) process where Ni-nanoparticles are dispersed in H13 steel molten pool in layer-by-layer fashion to produce three-dimensional gear molds; 2) laser-cladding based freeform fabrication (LBFF) process where shaped beam and novel quasi co-axial powder delivery system were used to produce functionally graded H13/Ni-Cr/TiC mold inserts; and 3) laser sintering (LS) of nanocrystalline diamond powders on aluminum alloy substrate to form thick diamond-like carbon coatings for enhanced wear resistance.

In the NAM process, AISI H13 steel micro-powder (70-100 μm), the standard material in the industry for dies and molds, was blended with Ni nano-powder (70-150 nm) in a volumetric ratio of 4:1 and then laser melted under conditions such that only H13 powder was melted and solidified. With the aid of CAD/CAM models and layer-by-layer addition process, gear-shaped molds were fabricated, characterized and tested. Scanning electron microscopy, surface profilometry, Rockwell and Vicker's hardness tests, corrosion test and injection-molding test using polystyrene were used to evaluate the performance of Ni/H13 molds. Results showed that nanoparticle dispersion has distinct improvements on the functional

capability of H13 steel molds to produce precision plastic parts; this is attributed to the role of nanoparticles in enhancing mechanical, chemical and tribological properties.

In the LBFF process, a hollow square-shaped, functionally-graded mold (FGM) insert was designed and built with additive layers of H13 steel, Ni/Cr alloy and TiC using circular and rectangular beam profiles. Finite element numerical methods were applied to determine temperature fields and thermal gradients. The cooling rates were estimated and correlated with secondary dendrite arm spacing. Analysis and characterization of FGM insert revealed nearly full density mold with excellent integrity, favorable microstructures, strong interfaces and high hardness. Strength and dimensional stability of molds were tested in a thermal fatigue environment and compared with baseline H13 steel. Improved strain tolerance, better crack resistance and higher oxidation resistance were the primary benefits of FGM mold.

In LS, nanocrystalline diamond powders (4-8 nm) were sprayed on 6061 aluminum alloy substrates to a nominal thickness of 25 μm by an electrostatic spray method and then laser sintered to consolidate and transform the diamond powder to diamond-like carbon (DLC) for a nominal thickness of 10 μm . Raman spectroscopy and X-ray diffraction analysis confirmed the presence of DLC coatings. Microhardness tests showed an average hardness of 2250 kg/mm^2 (some regions had a hardness of 9000 kg/mm^2) indicative of DLC. Fracture toughness and surface roughness were well within the typical ranges of DLC. Scanning electron microscope analysis revealed a near dense, fairly uniform coating with a flaw-free interface. Scratch tests indicated the ability of DLC coating to carry high loads without delamination. One-dimensional thermal energy transport models were formulated based on

laser energy absorption, thermal properties of diamond and aluminum, heat conduction and convection and solved using finite element ANSYS code. Results guide to a hypothesis that laser sintering of nano-diamond powder takes place in solid state around 800 K followed by densification and phase transition to DLC and coating/substrate interface heating to nearly the melting temperature of aluminum.

The general findings of this study lead to the conclusion that laser processing of nanoparticles and functionally-graded materials is a prudent approach for not only manufacturing of high performance dies, molds and aluminum structures but also a means of offering the design flexibility in part geometry, tolerance and surface finish.

CHAPTER 1. Introduction

The purpose of this research is to investigate different CO₂ laser-based, solid freeform technologies (Nanoparticle additive manufacturing (NAM), Laser based flexible fabrication (LBFF) and Laser sintering (LS)) for producing dies, molds and hard coatings. Dies and molds have extensive applications in manufacturing operations such as injection molding, die-casting, stamping, extrusion and forging. Because die and mold materials such as H-13 (hot work tool steel, chromium type) and P20 (mold steel, chromium type) usually have high hardness (40~60 HRC) and toughness, fabrication of such dies and molds relies heavily on high-speed machining, finishing and electrical discharge machining (EDM); however these processes waste significant amount of material and substantially increase the tooling costs. Solid freeform fabrication (SFF) is proven as an alternative in low volume tooling industry. In contrast to conventional subtractive machining, SFF is a flexible process to fabricate physical models of complex geometry with little material wastage. The versatility of laser aids this technology to become commercially viable. Laser cladding-based SFF is particularly useful for producing functional parts or components.

In another area, thick wear resistant coatings are highly sought after on light weight aluminum substrates. Laser sintering is an ideal process to form uniform dense coatings on such substrates. Aluminum alloys are attractive candidates for numerous structural applications due to their low density and high corrosion resistance. These are also potential substitutes for steels and cast irons. However, the poor wear, fretting and galling resistance and high thermal conductivity of aluminum alloys prevent their widespread application, for

example, in engine applications. It would be a significant advancement if the aluminum surfaces were modified to exhibit high thermal resistance; low friction and high wear resistance. This is particularly advantageous in energy-related manufacturing processes such as injection molding of polymers and composites.

1.1 Dissertation organization

The dissertation is organized into seven chapters and two appendices. Chapter 1 (this chapter) states the objectives of the research and summarizes the studies that are presented in latter chapters. Chapter 2 provides a review of literature on solid freeform fabrication technology, types of lasers for rapid prototyping, dies and molds, functionally-graded materials and nanoparticles. Chapter 3, a paper published in the *Journal of Manufacturing Science and Engineering*, reports the experimental investigations of laser-assisted nanoparticle additive manufacturing process for potentially extending lifetime of dies and molds. In this paper, molds were produced from nickel nanoparticle-dispersed H13 powder beds and their performance were compared against those molds made using H13 powder alone. Spur gear geometry was used as the mold design. Chapter 4, a paper published in the *Journal of Materials Processing Technology*, reviews the current status of die and mold making processes, as well as laser-cladding based solid freeform fabrication technology. It presents a novel design of powder delivery system and experimental/modeling studies of LBFF processing technology for producing functionally-graded molds of hollow square shapes using H13, Ni/Cr composite and TiC powders, and of mechanical property evaluation techniques for testing the functional components. Chapter 5, a paper to be published in *Surface Coatings and Technology*, deals with the laser sintering of nano-diamond powders

on widely used aluminum alloy 6061. Diamond powders were transformed into diamond-like carbon coating through this non-equilibrium, fast process. The coatings were evaluated using scratch, hardness, toughness and surface roughness tests along with sample characterization using Raman spectroscopy, scanning electron microscopy and X-ray diffraction. Chapter 6, another paper submitted to *Surface Coatings and Technology*, presents steady state and transient thermal analysis involved in the diamond powder bed before it transforms to diamond-like carbon. Temperature profiles along the depth of the coating and the substrate as well as the thermal stresses during cooling are calculated and displayed. Chapter 7 summarizes the general conclusions drawn from this body of research, and provides recommendations for future work that could yield better understanding of the phenomena behind the amplification of desired properties in the cases of NAM, LBFF and LS.

Two appendices are attached. One is the description of SFF facility that is available in Mechanical Engineering department. The other describes the design of powder delivery system, powder delivery rate calibration, together with detained uncertainty estimation analysis. Continuous and uniform powder transport is of great importance for the success of LBFF.

CHAPTER 2. Background

Solid freeform fabrication (SFF), also called as rapid prototyping (RP), is a manufacturing technology that generates physical models directly from graphical computer data [1] using a number of processes such as selective laser sintering (SLS). Currently, SFF is entering a new phase where modern materials and manufacturing are used to produce functional geometry that is generally difficult to carry out in traditional manufacturing. This technology fits well in tool industry of small /medium-sized tools such as injection molding molds and die-casting dies [2]. While modest engineering progress has been made in this field since 1990, work on materials, processing, mechanical properties, and quality issues associated with these layer-wise additive processes remains to be addressed. Laser-based flexible fabrication (LBFF) is a SFF process designed to fabricate functionally graded molds and dies with an objective of prolonging the life of dies and molds. Following sections provide an introduction to the development of solid freeform fabrication, lasers for rapid prototyping, dies and molds, and functionally graded and nanoparticle materials.

2.1 Solid Freeform Fabrication

SFF enables speeding up of iterative product development processes. Layer-by-layer manufacturing, the core concept of RP technology, allows fabrication of three-dimensional parts by the addition of materials rather than by the subtraction of material (as in machining) [3,4]. In this layer-wise additive manufacturing process, a computer representation of a designed part is decomposed into slices that provide 2-D dimensional information (Figure 2.1). Although RP can be achieved by use of CNC machining, the term, however, is

generally used in the context of fabricating parts by adding materials. The benefits of RP include: 1) quick tools for visualization and for concept verification due to its capability of producing physical models of designed concept in short time to allow rapid evaluation of manufacturability and design effectiveness; 2) ability to fabricate complex structures that are difficult to be built with traditional techniques; 3) flexibility in automation in process planning and manufacturing; and 4) functional tooling in a short lead-time.

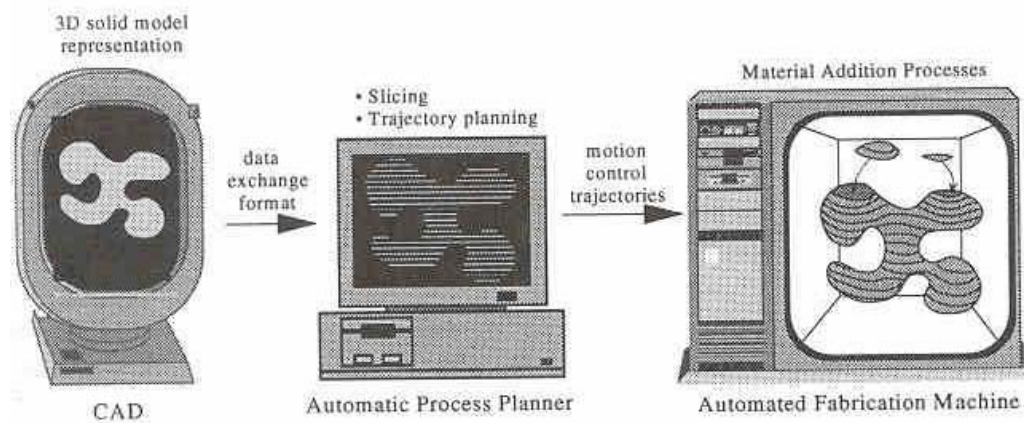


Figure 2.1 Schematic showing a 3-D model representation, slicing and process planning, and material additive process in SFF [5].

Rapid fabrication of near net shape parts is attributed to the absence of fixtures and tooling, the ability to work directly from computer geometric data, and the reduction of number of process steps [6]. It is gaining popularity as a means to significantly reduce the time to market [7]. Since the first RP technology, Stereolithography, or three-dimensional printing, was introduced by 3D systems in 1982, more than 20 different rapid prototyping technologies become available, some of them enjoy commercial success. In terms of the initial form of the materials used, all RP systems can be categorized into liquid-based, powder-based, and solid-

based additive manufacturing processes. An overview of the RP systems is shown in Table 2.1.

Table 2.1 A list of additive manufacturing processes (RP) [1-4]

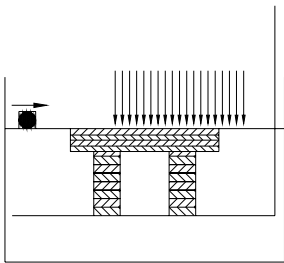
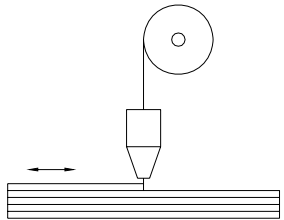
	Process	Configuration	Materials and Process Characteristics
Liquid	Stereo-lithography (SL)		<ul style="list-style-type: none"> – Photo polymers; – Photo-polymerization by laser illumination; – Hazardous effect; – Concept model and virtual rapid prototyping (VRP).
	Fused Deposition Modeling (FDM)		<ul style="list-style-type: none"> – Polymers, wax, metals with binder, and ceramic with binder; – Solidification by cooling; – Concept model, VRP, and limited functional uses.

Table 2.1 (continued)

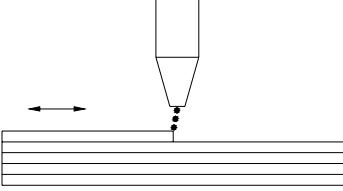
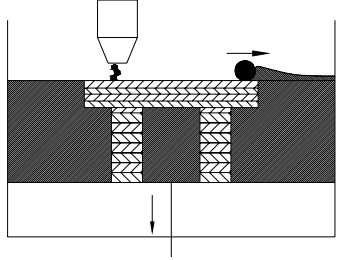
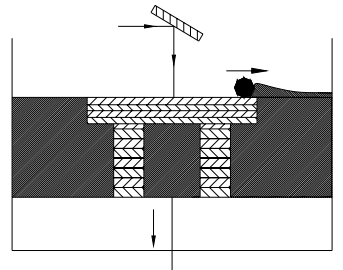
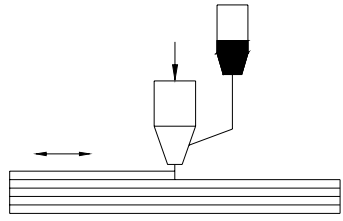
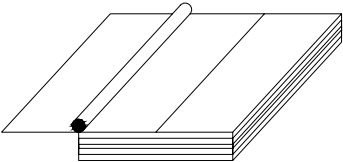
Liquid	Ink Jet Printing (IJP)		<ul style="list-style-type: none"> – Polymers, wax; – Solidification by cooling; – Concept model, VRP, and limited functional use.
Powder	Three Dimensional Printing (3D-P)		<ul style="list-style-type: none"> – Ceramic, metals, polymer, and binder; – No phase change; – Concept model, VRP, and limited functional applications.
	Selective Laser Sintering (SLS)		<ul style="list-style-type: none"> – Polymers, filled polymers, metals with binder; – Laser sintering; – Concept model, VRP, and partially functional use.
	Laser Cladding (LC)		<ul style="list-style-type: none"> – Metallic powders of micro-scale; – Laser melting and solidification by cooling; – Functional applications.

Table 2.1 (continued)

Solid	Laminated Object Manufacture (LOM)		<ul style="list-style-type: none"> – Paper, polymer, polymer foam, ceramics, and metals; – Laser cutting, knife cutting, and heated wire cutting; – No phase change, alignment problem, and material wastage; – Concept model, VRP, functional applications.
-------	---	---	--

Design for SFF affects not only the part surface integrity but also the strength. It is especially important when an over-hanged structure is desired because a viable design can greatly simplify the process with the least requirement of supporting structures and further post processing. Limited work has been done in this area. Functionality, surface roughness, minimal supporting structures and post processing are the control variables for SFF design. Surrogate materials such as photo-polymers, powders, paper, wax, and plastics, and functionally metallic powders are the two major choices for RP. There are some RP systems beginning to build parts on structural materials, although many of the existing RP systems are still using surrogate materials. The functions of prototypes vary significantly depending on the RP process and the materials used for that process. The major application sectors of

RP are in 1) design and analysis; 2) engineering and planning, and 3) tooling and manufacturing (dies and molds). The industries benefiting from RP include, but not limited to, aerospace, automotive, electronics, biomedical, and appliance [8].

RP technology has been used to fabricate concept models, prototypes, and tooling for manufacturing dies and molds [9,10]. However, a significant limitation of RP systems is the use of surrogate materials rather than structural materials to construct prototypes, which are good only for the concept verification, visual prototyping, and limited functional applications. The physical, mechanical, and chemical properties of these surrogates do not allow them to be used for functional prototypes or tooling applications.

Selective laser sintering (SLS) of powder materials is a classical example of SFF that initially seemed to have potential for producing functional prototypes and even for direct tooling fabrication. However, it requires polymer binders or low-melting compounds to become feasible [11-14]. Because SLS just “wets” rather than really melts powder, drawbacks of shrinkage, porosity, and low density exist in components that were fabricated. These drawbacks prevented SLS from competing against conventional CNC milling and EDM for mold and die fabrication, and seriously limited many other real world applications. Recently, SFF systems based on laser-cladding (LC) technology have appeared to correct these deficiencies. LC is a surface engineering technology that creates surfaces of enhanced hardness, wear resistance, or corrosion resistance with minimal dilution. LC technology has been around for some 20 years and mainly has been used for modifying surface properties or repairing damaged surfaces. It basically consists of pneumatically injecting fine powders

through a nozzle into a localized molten pool created by a laser on the substrate surface. Subsequent solidification of the powder on the substrate produces strong, bonded layer. The benefits of LC are 1) fully dense and homogeneous microstructures; 2) low thermal damage to the underlying substrate, 3) reduced grain growth and distortion; 4) non-equilibrium and amorphous structures, and 5) extension of solid solubility of alloying elements. These benefits, in turn, strengthen the tribological and mechanical properties including hardness, strength, wear resistance, corrosion resistance, and toughness. In addition, this process has the potential to remedy the surface defects on die and mold surfaces by re-melting. The commonly used powders are Co- and Ni-based alloys and carbides in micro-size. LC can be used to fabricate 3-D geometry if layers of overlapped-track are built continuously.

LC technology was applied to RP systems [15,16]. Several LC-based RP systems having minor variations were reported. These include 1) laser-engineered net shaping (LENS) from Sandia National Laboratory [17]; 2) direct light fabrication (DLF) from Los Alamos National Laboratory [18,19]; 3) direct metal deposition (DMD) at University of Michigan [20]; 4) shape deposition manufacturing (SDM) at Stanford University [21]; 5) laser direct casting (LDC) at the University of Liverpool [22]; and 6) the high-power, laser-based freeform fabrication process from the Pennsylvania State University [22]. Among all these versions, LENS is the only one having reached sufficient maturity to enter the commercial market (Optomec™ LENS Model 750). It uses a continuous wave (CW) Nd:YAG laser of high power (3 kW) to melt an area on the surface of a metal substrate while a nozzle, being concentric with laser beam, simultaneously delivers metal powder to the molten pool. Layers

are built in a direction perpendicular to the substrate, to increase the part height. The most common application of LENS is the direct fabrication of injection molds [17].

LC-based RP technologies offer flexibility to design with tailored materials and potential in producing components of high performance. However, none of the LC-based RP systems has produced functional parts that are acceptable for industrial applications in terms of relevant standards due to rough surfaces (R_a , higher than 50 μm), low degree of dimensional accuracy (up to one millimeter offset from designed dimensions), and residual stresses existing in the components built by use of existing RP systems. In addition, issues such as design for SFF, material compatibility for complicated multi-materials construction, point-wise deposition of one or more materials to fabricate novel microstructural and macrostructural features, and process modeling remain to be addressed before these new techniques are technically and economically successful for widespread industrial use.

In this work, we have developed a technique, laser-based flexible fabrication (LBFF), to assist in solving these problems. It could be effectively used in creating parts (dies and molds, direct metal prototypes) with configurations such as graded interfaces, designed microstructures, and conformal cooling channels. It could also be used in other industrial applications including die and mold repairing, surface modification, and coatings. LBFF uses shaped laser beams, functionally graded materials, a CW CO_2 laser of 1500 W in rated power, and a computer integrated CNC control system. The shaped beams can fabricate layers of improved surface finish, dimensional tolerance, and reduced dilution among

overlapped gradient layers. The shaped beam profiles produce more uniform temperature gradient than circular beam, and also stretch beam trailing edges to preheat the powders.

2.2 Lasers for Rapid Prototyping

Many RP systems use lasers and beam steering devices in one way or the other to expose photopolymers, cut non-photosensitive materials, sinter particulates, or to melt powder materials [1]. Lasers are stimulated emission devices that generate narrow, intense beams of coherent light in wavelength ranging from ultraviolet to infrared regions. The first industrial laser was introduced in the late 1960s [23]. Lasers, the versatile industrial tools, find wide applications in manufacturing ranging from machining (cutting, drilling, milling, scribing, and marking) and joining (welding, brazing, and soldering) to materials processing (powder synthesis, thin films, and heat treatment) due to their advantages in precision, productivity, flexibility, and automation.

A variety of lasers including solid, liquid, and gas are available. Each specific type of laser is normally identified by the medium that produces the light emission. The basic characteristics of laser beams are 1) energy density (power density), 2) wavelength, 3) coherence, 4) mode and beam diameter, and 5) polarization. Energy density is of great importance in materials processing. Excessive energy density may evaporate materials and create molten surface of high roughness; too low energy density may not melt materials fully and result in insufficient bonding. Wavelength affects the laser beam size and the absorption of a given material. Usually a beam of short wavelength and small divergence produces small spot size. Materials tend to absorb laser beam of short wavelength more efficiently.

The lasers most widely used in industry for material processing are solid-state neodymium-doped yttrium-aluminum-garnet (Nd:YAG) lasers, gas carbon dioxide (CO₂) lasers, and gas excimer lasers, because they have the ability to produce high power outputs and flexibility in controlling laser parameters such as pulse width, power, and wavelength. Nd:YAG laser is the most common member of solid-state lasers with wavelength of 1.06 μm . It can generate CW beams with power ranging from a few milliwatts to over a kilowatt, pulsed beams of average power up to several kilowatts with reasonable efficiency. Nd:YAG laser operates on optical pumping, raising Nd atoms to an excited energy level by means of light from external sources. The major industrial uses of Nd:YAG laser are in metal drilling, spot welding, marking and resistor trimming. Because of its high peak power and short wavelength, and easiness for beam delivery by means of optical fibers, Nd:YAG laser has also found applications in medical field. Carbon dioxide laser, with wavelength ranging from 9 to 11 μm , is one of the most versatile gas lasers. It is called as industrial workhorse because of its ruggedness and reliability. It can run in both CW and pulsed modes. In CW mode, CO₂ laser is capable of producing beam power from well under one watt to several tens kilowatts, while in pulsed mode, it can generate pulses of nanoseconds to milliseconds. Carbon dioxide lasers are pumped by use of electrical discharge, and mainly find applications in cutting, welding, and heat treatment.

Laser power, beam profile and dimensions, and traverse speed are important parameters for materials processing. Beam profiles can be varied using diffractive optics. Usually power density, dwell time, and sometimes also laser wavelength define the processing ranges for specific applications as shown in Figure 2.2.

The availability of computer controlled positioning stages, computer aided design techniques, and versatile laser technology further advances the development of RP systems. The integration of these technologies has already impacted the fabrication of shaped structural materials. The laser-associated RP technology is reducing the use of traditional material removal manufacturing and will eventually be a replacement for subtractive processes to generate functional components such as dies and molds.

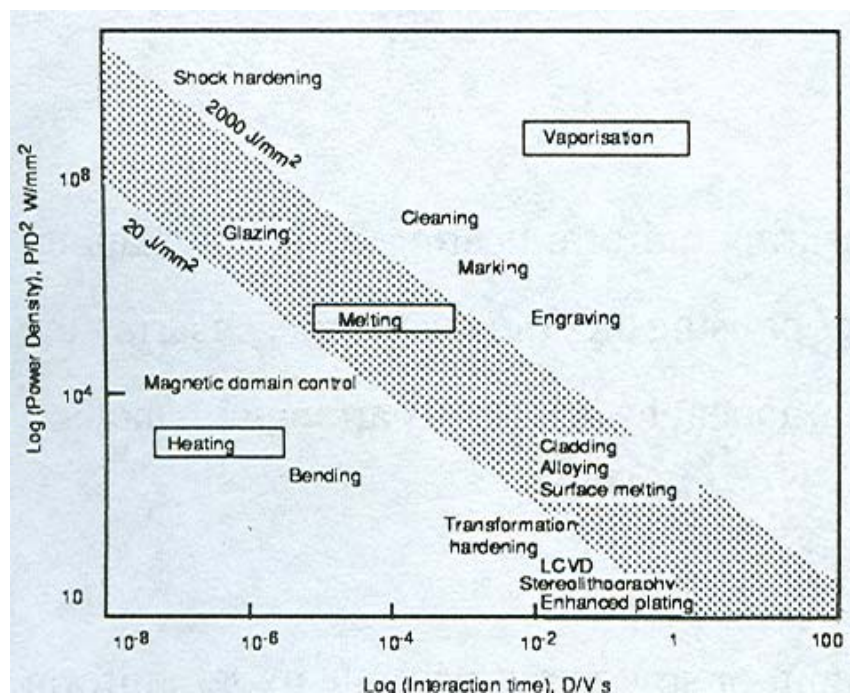


Figure 2.2 Window of laser power density and interaction time suitable for material processing applications [24].

2.3 Dies and Molds

Dies and molds are extensively used in non-ferrous casting (aluminum, zinc, magnesium, and etc.), plastic injection molding, and forming (cold extrusion and hot extrusion, stamping, and forging) industries. The global market for dies and molds is estimated at 65 billion US dollars

[25]. Dies and molds constitute a major portion of costs associated with manufacturing operations such as injection molding, die-casting, stamping, extrusion, and forging. For a company or an industry to survive in today's fiercely competitive market, modern materials and fabrication technologies must be used to shorten the product time to market and produce products of high quality with cost-effectiveness. Dies and molds are becoming standardized in order to ease fabrication and to reduce cost [26]. Often dies and molds are composed of supporting and functional components [25, 26]. Parts with square or round shape, which are readily designed and made, usually serve as bases or supporting blocks for immediate use. The other supporting components are used for alignment, part ejection, and heating or cooling. Functional components, which include die cavity, core insert, and punch, have to be designed specifically to tailor for different applications. The cavity and core inserts for injection molding and die-casting are usually made out of solid blocks of alloy steels. Occasionally, forging dies and injection molds are manufactured by cold or hot hobbing. The widely used materials for dies and molds are hot work tool steel H series (chromium type), mold steel P series (chromium type), among which H13 and P20 are the two most common [27]. The general requirements for die and mold materials are (1) strength and toughness at elevated temperature, (2) mechanical and thermal shock resistance, (3) hardness, and (4) wear resistance [26-28].

Design of dies and molds is generally an iterative process though various CAD/CAM and virtual prototyping (VR) technologies are available to assist or speed up the process. Die and mold design must be closely interactive with processes because design models have to be updated accordingly after any modification to the prototypes. When methods are chosen for

manufacturing mold and die parts, important criteria of feasibility, cost, productivity and quality have to be considered [26]. Usually the conventional fabrication of dies and molds starts with rough machining followed by finishing and tryout processes. Currently milling (CNC, high speed milling) and electrical discharge machining (EDM) are the two major methods used to make most of dies and molds out of wrought tool steel blocks [25,26]. They are classified as subtractive processes. The sequential steps of processing used in traditional die and mold manufacturing are shown in Figure 2.3.

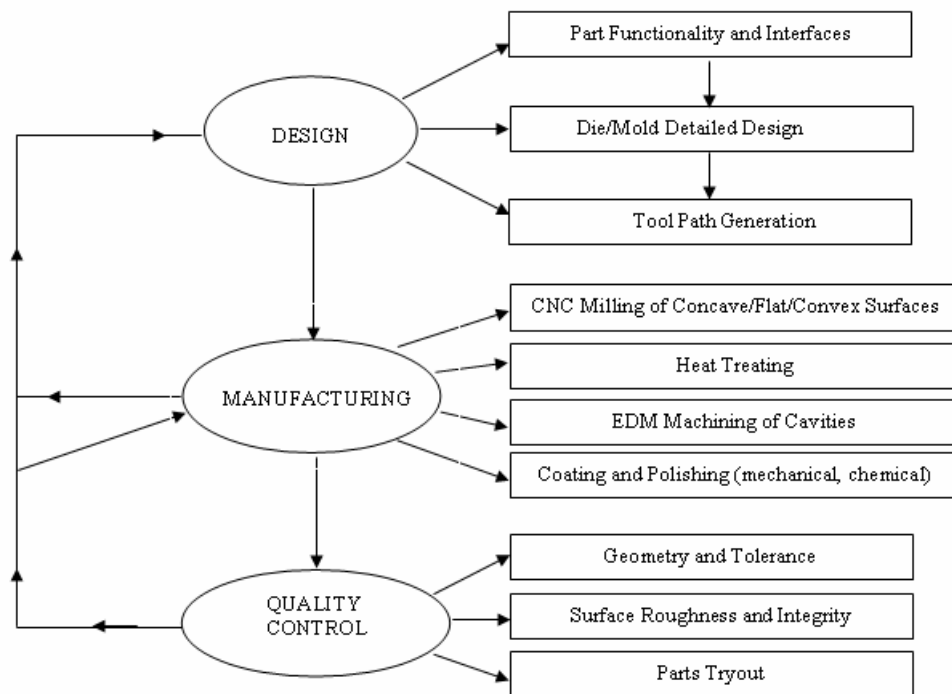


Figure 2.3 A flow chart showing the process plan for conventional manufacturing of dies and molds.

Die and mold machining is a costly and time-consuming process, in which a significant portion of material is wasted. Also, machining does not allow for flexibility in obtaining the

desired tool geometry. For example, conformal cooling channels and holes, which could increase product throughput by some 25% or more, are difficult to produce in traditional machining [29]. In addition, the machined mold often has to be subsequently heat-treated, surface treated or coated to impart the desired microstructure and properties. The heat treatment, if improperly done, causes dimensional instability and generates residual stresses. Study has showed that more than 70% of die failures are attributed to the improper heat-treatment of the steels [30]. Post-treatment operations such as grinding and EDM may damage the surface integrity if not carefully executed because these operations can easily result in tempered layers and soften the surface materials [26]. Alternatives to machining are powder consolidation processes such as hot isostatic pressing (HIP), which uses rapidly solidified powders to produce dies and molds that outperform cast and machined tools. However, the high cost and long lead-time of these processes limit their applications [31].

2.4 Functionally Graded Materials

A functionally graded material (FGM) is a combination of two or more materials in which a gradual transition among microstructures and compositions across the interface exists rather than the distinct junction found in laminated composites or coatings. In a FGM, there is no “gap” of material properties due to its composition and structure gradually changing over volume. Design of FGM’s is to ascertain required properties that one material normally does not have by varied combinations of constituent materials. It is usually represented by the geometry of a FGM with the spatial distribution of its constituent materials, microstructures and properties. Besides functional requirements, compatibility between materials, residual stresses, and component element diffusion at elevated temperatures are also of great concerns

in designing a FGM. Quantitative microstructural analysis methods are helpful in understanding the fundamental relationships between structures and properties. Rules of mixtures, variational approach, micromechanical methods, and empirical approach are usually used to estimate the properties [32].

A variety of processing techniques are available for fabricating of FGMs. These processing methods include powder metallurgy, physical and chemical vapor deposition, plasma spraying, self-propagating high temperature synthesis (SHS), galvanofarming, and the most recently solid freeform fabrication. Basically, most of these methods work on either constructive processing or mass transport mechanism. Constructive processing starts with addition of thin slice of materials on a substrate; and mass transport is closely related to the flow of fluids, the diffusion of molecules or atoms, or the conduction of heat. Usually different processing techniques and conditions result in FGMs exhibiting significantly different microstructures and properties. The characterization of FGMs includes the evaluation of their local microstructures and properties. Determination of size, orientation, and phases of local microstructures can be achieved by means of optical microscopes, scanning electron microscope (SEM), and chemical analysis; and evaluation of properties such as microhardness, thermal conductivity, fatigue behavior, and so on may be measured by use of standardized technique or designed experiment.

The FGM concept has been demonstrated in many engineering applications, including cutting tools, machine parts, and engine components. Typical examples of FGMs are SiC/C, WC/Co, and FeAl/SS. One SFF technique, extrusion freeform fabrication (EFF) with

multiple extruders, has been developed to produce prototype of alumina/NiAl, alumina/stainless steel, and WC/NiAl [33].

2.5 Nanoparticles

Nanoparticles possess unique mechanical (strength, modulus, toughness) and physical (density, thermal expansion, conductivity) properties. They have large surface area-to-volume ratios, large fraction of atoms residing at the interfaces, phonon scattering, quantum effects, small residual pore sizes, and extremely fine grain, phase and domain sizes. They can significantly enhance mechanical properties like an increase in strength, hardness, toughness, and thermal expansion and a decrease in thermal conductivity, stiffness and density [34-36]. Nanoparticle-reinforced dies have longer die life because of higher densities, greater structural integrity, reduced residual stress and lower dilution. Coatings containing nanoparticles have an enormous role to play in applications because of their wear-, erosion-, and abrasion-resistant properties [37]. Nanocoatings have improved hardness and toughness when compared to other commercial coatings as shown in Figure 2.4 below.

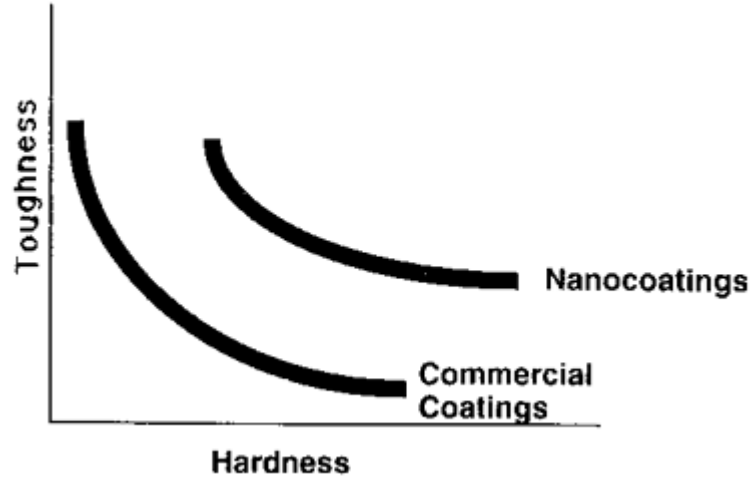


Figure 2.4 Comparison of nanocoatings and other commercial coatings [34].

Table 2.2 shows some beneficial effects of nanoparticles in real-world applications.

Table 2.2 Durability improvements using nanoparticles [34].

Coating Programs	Critical Nanostructure Property	Component/Engine Benefit
Co-WC wear-resistant coating	Increased hardness	5X life
Erosion/moisture-resistant coating for polymer matrix composites	Increase hardness Increases adherence	5X life Higher design allowable
High temperature, crack-resistant coating	Increases strength Interface crack blunting Oxygen impermeable layer	3X life
Advanced thermal barrier coating	Reduced conductivity	+2% thrust/weight -1% fuel consumption

Nanoparticles have proven their values by enhancing environment (catalytic converters), improving energy performance (fuel cells), extending Moore's law (single electron devices) and advancing healthcare (drug delivery). Nanomaterials constitute the largest application

(about 37%) of nanotechnology in the fields of electronics, biomedical, functional materials, human safety and environmental protection, and consumer and diversified products [38, 39]. The total world market for nanomaterials reached an estimated one billion dollar [38-40]. The electronic, magnetic and optoelectronic applications account for nearly 75%; biomedical, pharmaceutical and cosmetic applications account for 16%; and energy, catalytic and structural applications take the remaining 14%, according to the Business Communications Company report [41].

The two major challenges facing nanoparticles are manufacturing and health and worker safety. In manufacturing, the key issues are: 1) lack of cost-effectiveness due to low-level production; 2) large variation in particle size and shape due to the difficulty in controlling the process; and 3) segregation and agglomeration during processing. Conventional techniques that produce nanoparticles share the common drawback of low production rate (grams per hour) at moderate quality, suggesting an enormous need for “high-productivity and high quality” manufacturing techniques, which are central to the commercialization of nanoparticle products. Hence, a major impediment to the use of presently manufactured nanoparticles is the extreme cost (\$100 to \$2000 per kilogram, depending on the type). The other issue that confronts the method of preparation is the control over nanoparticle's size, shape and composition that are necessary to ensure that the nanoparticle will be made to comply with future requirements and be tailored for specific commercial applications. In addition, surfactants and dispersants are used to obtain stable, agglomeration-free nanoparticles. Consequently, the existing manufacturing techniques are being continuously refined while at the same time novel production methods are being invented and developed.

The societal problems of nanoparticles include health, worker safety and education. There were many uncertainties as to the health effects of nanoparticles. For example, nanomaterials can be inhaled and ingested, raising the questions of potential health effects on skins, lungs and brain. Research is needed to better understand the impact of these occupational exposures on workers' health. In the U.S., an estimated 2 million people work with nanoparticles on a regular basis in development, production, and use of nanomaterials or products (based on year 2000 national industry-specific occupational employment estimates by the U.S. Department of Labor's Bureau of Labor Statistics). If growth in nanotechnology-related industries meets expectations, a similar number of additional workers will be required globally. Some critical questions that need to be answered for supporting the responsible development of nanotechnology include: In what ways might employees be exposed to nanomaterials in manufacture and use? In what ways might nanomaterials enter the body during those exposures? Once in the body, where would the nanomaterials travel, and how would they interact physiologically and chemically with the body's systems? Will those interactions be harmless, or could they cause acute or chronic adverse effects? What are appropriate methods for measuring and controlling exposures to nanoparticles and nanomaterials in the workplace?

The commercially important nanoparticulate materials are metal oxides such as SiO_2 , TiO_2 , Al_2O_3 , Fe_2O_3 , ZnO , CeO_2 and ZrO_2 [38, 40]. While silica and iron oxide nanoparticles have a commercial history spanning half a century or more, nanocrystalline TiO_2 , ZnO , CeO_2 and other oxides have recently entered the marketplace. Mixed oxides, such indium-tin oxide ($\text{In}_2\text{O}_3\text{-SnO}_2$ or ITO), antimony-tin oxide (ATO), and titanates (BaTiO_3), are highly sought

after. Other types of nanoparticles such as semiconductors, ceramics (e.g., tungsten carbide) and metals are also under development and available in laboratory- and pilot-scale quantities.

Table 2.3 lists the potential applications of nanomaterials. Most of the cutting edge work in nanomaterials is being done by small companies, many of which have proprietary processes for generating the nanoparticles in highly uniform sizes, shapes and purities. Some of these firms have formed marketing and development alliances with large global chemical and plastics suppliers such as Honeywell and DuPont. Although several companies are involved in the development and production of nanoparticles, the major suppliers can be short listed to about 10, whose products are described in Table 2.4. A variety of processes, shown in Table 2.5 [36, 37, 42-44] suggest that the production rate is quite limited. Chemical and physical vapor phase synthesis's are well-established technologies for large-scale production of metal, metal oxides, and ceramic nanoparticles. However, the challenges for vapor phase synthesis are the control of particle size distribution, *in-situ* formation of hybrid particles and structures, inefficient collection systems, and difficulties in running continuous operations at high throughput and yield. Separation of nanoparticles in solid/liquid and solid/gas is scientifically challenging. Spray pyrolysis, precipitation, crystallization, sol-gel, emulsion polymerization are processes designed to produce complex nanoparticles.

Table 2.3 Potential Applications of Nanomaterials.

Electronics	Displays; Gas sensors; Printing; CMP slurry; Photonics; Inks; Batteries; Fuel cells; Quantum dots
Biomedical	Drug delivery; Gene delivery; Biosensors; MRI contrast agents; Smart polymers; Protein-assisted self-assembly; Biocatalysts; Dental fillings;
Functional	Conducting polymers; Ink-jet inks; Scratch-resistant coatings; UV materials; Packaging films; Lighter/stronger/tougher composites; Cutting tools, and transparent armor materials. catalysts for emissions reduction
Environment	Antiviral and antifungal; Pollution-free air and water; Fire protective apparel Military uniforms. fire retardants; wearable sensors
Consumer	Functional foods; Nutraceuticals; stain-free khaki pants; Paints; Skin care products; Deodorizers; Fragrance; Self-cleaning windows; Tennis balls

Table 2.4 Major suppliers of nanopowders.

Company	Product	Technology	Market
Nanophase Technologies, Inc.	Oxides of Al, Sb, Ce, Cu, Fe and Zn	Vapor condensation	Health care, catalysts, coatings
Kemco International Associates	Oxides of Al, Fe, Ce, Sn, Cr, Ti, etc.	Vapor synthesis	Health care, electronic displays, catalysts
Nanomaterials Research Corporation	Dspersions such as ZnO, SiC etc.	Combustion Synthesis	Electronics, Advanced ceramics
Nanox	Ultrafine ZnO, FeO	Unknown	Cosmetics, coatings
Nanopowder Enterprises	Metals, oxides, carbides, nitrides	Combustion flame, spray forming	Coatings, electronic devices, displays
Altair Technologies	Titanium oxide	Film growth, pigment process	Coatings, catalyst, cosmetics, electronics
Advanced Powder Technolgies, Inc.	Nano-oxide and metal powders	Metal melt atomization	Electronics, advanced ceramics
Nanodyne, Inc.	WC, WC-Co	Solution spray and thermal spray	Coatings, cutting tools
Powdermet	Metal and ceramic powders	Fluidized bed CVD	Coatings, advanced ceramics
NexTech Materials	Ceramics	Chemical Synthesis	Advanced ceramics

Table 2.5 Nanopowder synthesis methods [36, 37, 42-44].

Method	Production rate	Problems
Mechanical milling	1-5 g/hr	Powder contamination
Vapor Condensation	1-5 g/hr	Difficult to control particle morphology
Sputtering	< 5 g/hr	Only 6-8% of particles are < 100 nm
Chemical precipitation	10-50 g/day	Agglomeration and oxidation
Induction Plasma	--	Efficiency is <50%
Microwave plasma	--	Limited precursors, coupling energy to metals is difficult
Combustion synthesis	10-50 g/hr	Difficult to control particle morphology
Laser ablation	<0.1 g/hr	Low energy efficiency
Sol-gel	1-3 g/hr	Additional step of solvent removal

References

1. Jacobs, P. F. (1992). *Rapid Prototyping & Manufacturing: Fundamentals of Stereolithography*. Society of Manufacturing Engineers, Dearborn, MI 48121-0930.
2. Dalgarno, K. W. (2001). Production Grade Tooling via Layer Manufacture. *Rapid Prototyping Journal*, Vol. 7, No. 4, pp. 203-206.
3. Kruth, J. P. (1991). Material Ingress Manufacturing by Rapid Prototyping Techniques. *Annals of the CIRP*, Vol. 42, No. 2, pp. 603-614.
4. Kruth, J. P., Leu, M. C. and Nakagawa, T. (1998). Progress in Additive Manufacturing. *Rapid Prototyping Journal*, Vol. 42, No. 2, pp. 525-540.
5. Beaman, J. J., Barlow, J. W, Bourell, D. L., Crawford, R. H., Marcus, H. L. and McAlea, K. P. (1997). *Solid Freeform Fabrication*, Kluwer Academic Publishers, Boston.
6. Burns, M. (1993). *Automated Fabrication: Improving Productivity in Manufacturing*. Prentice-Hall, Englewood Cliffs, NJ, 1993.

7. Dahotre, N. B. (ed.) (1998). *Lasers in Surface Engineering*. ASM International, Materials Park, OH 44073-0002, 1998.
8. Chua, C. and Leong, K. (1997). *Rapid Prototyping: Principles & Applications in Manufacturing*. John Wiley & Sons (Asia) Pvt. Ltd, Singapore 128909.
9. Hull, C., Feygin, M., Baron, Y., Sanders, R., Sachs, E., Lightman, A. and Wohlers, T. (1995). Rapid Prototyping: Current Technology and Future Potential. *Rapid Prototyping Journal*, Vol. 1, No. 1, pp. 11-19.
10. Kochan, A. (1997). Rapid Prototyping Trends. *Rapid Prototyping Journal*, Vol. 3, No. 4, pp. 150-152.
11. Agarwala, M., Bourell, D., Beaman, J., Marcus, H. and Barlow, J. (1995). Direct Selective Laser Sintering of Metals. *Rapid Prototyping Journal*, Vol. 1, No. 1, pp. 26-36.
12. Subramanian, K., Vail, N., Barlow, J. and Marcus, H. (1995). Selective Laser Sintering of Alumina with Polymer Binders. *Rapid Prototyping Journal*, Vol. 1, No. 2, pp. 24-35.
13. Klocke, F., Celiker, T. and Song, Y. A. (1995). Rapid Metal Tooling. *Rapid Prototyping Journal*, Vol. 1, No. 3, pp. 32-42.
14. Gibson, D. and Shi, P. (1997). Material Properties and Fabrication Parameters in Selective Laser Sintering Process. *Rapid Prototyping Journal*, Vol. 3, No. 4, pp. 129-136.
15. Gerken, J., Haferkamp, H. and Schmidt, H. (1994). Rapid Prototyping/Manufacturing of Metal Components by Laser Cladding. *Proceedings of the 27th International Symposium on Automotive Technology and Automation*, Oct 31-Nov 4, Aachen, Germany, pp. 85-90.

16. Jeng, J. Y., Peng, S. C. and Chou, C. J. (1994). Application of Selective Laser Cladding in Rapid Prototype. *Proceedings of the 27th International Symposium on Automotive Technology and Automation*, Oct 31-Nov 4, Aachen, Germany, pp. 272-279.
17. Keicher, D. M. and Miller, W. D. (1998). LENSTM Moves Beyond RP to Direct Fabrication. *Metal Powder Report*, Vol. 53, No. 12, pp. 26-28.
18. Milewski, J., Lewis, G. K., Thoma, D. J., Keel, G. I. and Nemeç, R. B. (1998). Direct Light Fabrication of a Solid Metal Hemisphere Using 5-axis Powder Deposition. *Journal of Material Processing Technology*, Vol. 75, pp. 165-172.
19. Milewski, J., Lewis, G. K., Fonseca, J. and Nemeç, R. B. (2000). Laser Powder Deposition of a Near Net Shape Injection Mold Core-A Case Study. *Materials and Manufacturing Processes*, Vol. 15, No. 2, pp. 247-258.
20. Mazumder, J., Choi, J., Nagarathnam, K., Koch, J. and Hetzner, D. (1997). The Direct Metal Deposition of H13 Tool Steel for 3-D Components. *Journal of Metals*, May, pp. 55-60.
21. Link, G. R., Fessler, J., Nickel, A. and Prinz, F. (1998). Rapid Tooling Die Casting Inserts Using Shaped Deposition Manufacturing. *Materials and Manufacturing Process*, Vol. 13, No. 2, pp. 263-274.
22. Irving, R. (1999). Taking a Powder. *Mechanical Engineering*, September, pp. 55-59.
23. Grigoryants, A. G. (1994). *Basics of Laser Material Processing*, Mir Publishers, Moscow.

24. Mazumder, J., Conde, O., Villar, R. and Steen, W. (ed.) (1996). *Laser Processing: Surface Treatment and Film Deposition*. Kluwer Academic Publishers, Dordrecht.
25. Altan, T., Fallbohmer, P. and Rodrigues, C. *HSM Research-On the Edges of Technology*, online article, <http://www.modernmachine-shop.com/articles/hsm-9801.html>, Accessed: November 23, 2003.
26. Stoekhert, K. (ed.) (1983). *Mold-Making Handbook: For the Plastics Engineer*, Hanser Publishers, New York.
27. Herman, E. A. (1979). Die Casting Dies: Designing. *Society of Die Casting Engineers Inc.*, Detroit, MI 48253.
28. Kalpakjian, S. and Schmid, S. R. (2001). *Manufacturing Engineering and Technology*, Prentice Hall, Inc., Upper Saddle River, New Jersey 07485, fourth edition.
29. Jacobs, P.F. (1999). New frontiers in mold construction: high conductivity materials & conformal cooling channels. Technical Paper No. n CM99-115, *Society of Manufacturing Engineers*, pp. CM99-115-1 – CM99-115-18.
30. Pullen, P. and Merchant, V. (1996). Lasers in the Die and Mold Industry. *Industrial Laser Review*, April, pp. 13-16.
31. Agarwala, M., Bourell, D., Beaman, J., Marcus, H. and Barlow, J. (1995). Direct Selective Laser Sintering of Metals. *Rapid Prototyping Journal*, Vol. 1, No. 1, pp. 26-36.

32. Miyamoto, Y., Kaysser, W. A., Rabin, B. H., Kawasaki, A. and Ford, R. G. (1999). *Functionally Graded Materials: Design, Processing and Applications*, Kluwer Academic Publishers, Boston/Dordrecht/London.
33. Hilma, G. (1996). Innovative Techniques for Rapid Prototyping Parts of Polymers, Metals, Ceramics, Composites and Functionally Graded Materials, *Materials Technology*, Vol. 11, No. 6, pp. 226-228.
34. World Technology Evaluation Center, (1997). R&D status and trends in nanoparticles, nanostructured materials, and nanodevices in the U.S. *Proceedings of the May 8-9 Workshop*, <http://itri.loyola.edu/nano/US.Review/toc.htm>, Retrieved – March, 1st, 2003.
35. Goldstein, A. N. (1997). *Handbook of Nanophase Materials*. Marcel Dekker, Inc., NY.
36. Chaudhari, R. (2000). *Handbook of Nanostructured Materials and Technology*, Marcel Dekkar, Inc.
37. Manthiram, A., Bourell, D. L. and Marcus H. L. (1993). Nanophase materials in solid freeform fabrication. *Journal of Metals*, November, pp. 66-70.
38. Zhao, Q., Boxman, A. and Chowdhry, U. (2003). Nanotechnology in the Chemical Industry-Opportunities and Challenges. *Journal of Nanoparticle Research*, Vol. 5, pp. 567–572.
39. Report of President's Council of Advisors on Science and Technology. (May 2005). The National Nanotechnology Initiative at Five Years: Assessment and Recommendations of the National nanotechnology Advisory Panel.

40. From the website - http://www1.elsevier.com/WZ/III-Vs/market_news/news/000069/, Nanotechnology related material, Accessed – December 1st, 2006.
41. GB-290 Nanotechnology: A Realistic Market Evaluation, McWilliams, A. March 2004.
42. Koch, C. C. (1993). The Synthesis and Structure of Nanocrystalline Materials Produced by Mechanical Attrition: A Review. *Nanostructured Materials*, Vol. 2, pp. 1091-1129.
43. Axelbaum, R. L., Bates, S. E., Buhro, W. E., Frey, C., Kelton, K. F., Lawton, S. A., Rosen, L. J. and Sastry, S. M. (1993). Wet Chemistry and Combustion Synthesis of Nanoparticles of TiB_2 . *Nanostructured Materials*, Vol. 2, pp. 139-147.
44. Tompa, G. S., Skandan, G., Glumac, N. and Kear, B. H. (1999). A New Flame Process for Producing Nanopowders. *The American Ceramic Society Bulletin*, October, pp. 70-75.

CHAPTER 3. Nanoparticle Additive Manufacturing of Ni/H13 Steel Injection Molds

Paper published in ASME *Journal of Manufacturing Science and Engineering*, 126(3), 2004

Rajeev Nair, Wenping Jiang and Pal Molian

Abstract

Nanoparticle Additive Manufacturing (NAM), a novel solid freeform fabrication process, is a computer-integrated, numerical controller-guided, beam-shaped, laser-cladding process that involves dispersion of nanoparticles into the laser-melt pool. Subsequent solidification results in a thin horizontal layer of nanoparticle-reinforced composite and layer-by-layer addition generate freestanding structures with spatial variations in microstructure. In this paper, we report fabrication of Ni-nanoparticle-dispersed H13 steel gear-shaped molds through use of NAM, characterization of the mold's microstructure, measurement of hardness and corrosion resistance, and determination of the mold's functional capability to produce plastic gears by means of injection molding. The properties and performance of nanopowder-dispersed H13 molds were compared against the benchmark H13 steel molds.

3.1 Introduction

Nanoparticles possess unique mechanical and physical properties because of their large surface area-to-volume ratios, small residual pore sizes, large fraction of atoms residing at the interfaces, phonon scattering, and extremely fine grain, phase, and domain sizes. The effects of nanoparticles on the properties include an increase in strength, hardness, toughness, thermal expansion and diffusivity and a decrease in thermal conductivity, stiffness and density [1-3]. Nanoparticle containing bulk materials and coatings promise to offer a

quantum leap in improvement of engineering properties, compared to properties of current engineering materials. The enhancement of mechanical properties by nanoparticles has enormous implications for a wide variety of wear-, erosion-, and abrasion-resistant materials as well as thermal insulation applications. Nanoparticles have the potential to produce dies of higher densities, with great structural integrity, reduced residual stress, and lower dilution. For example, single-layer test coupons with nanoparticles showed improved integrity, with greatly reduced macro-crack formation, in the selective laser sintering process [4].

In this work, we have developed a novel technique, *Nanoparticle Additive Manufacturing* (NAM), for fabricating high-performance, long-life dies and molds. NAM, a solid freeform fabrication (SFF) process, involves dispersion of nanoparticles in the laser-melt. It is capable of producing freeform, complex geometry components directly from a computer-generated model, with significantly greater benefits over traditional SFF processes. Such advantages include improved mechanical properties, greater dimensional accuracy, smoother surfaces, and decreased residual stresses. Consequently, NAM has the potential in a wide range of industrial uses, to improve quality, reduce cost, and shorten lead-time in die and mold tooling applications for major manufacturing sectors, including the automotive, electronics, and appliance industries.

Our approach to engineering a gear-profile injection mold involved laser melting of a powder bed composed of micropowders of H13 steel and nanopowders of Ni, resulting a near-uniform dispersion of nanoparticles (Figure 3.1). When H13 steel is in the molten state, nanoparticles can be readily dispersed by virtue of characteristics such as high melting

temperature, high ratio of surface area-to-volume, short diffusion length for solid-solid reaction, and the presence of atomic forces comparable to the mass of an individual particle. The envisioned process is a form of liquid-solid sintering in which the laser energy is used only to raise the powder temperature of the binder metal (in this case H13 steel) and cause it to melt and flow through the solid nanoparticles by driving forces such as the liquid pressure, viscosity and capillary forces. If the liquid has low viscosity and high surface tension, it will wet the nanoparticles, resulting in excellent bonding. Subsequent solidification of the melt results in a thin horizontal layer of nanoparticle-reinforced-composite. Continued layer-by-layer addition generates a gear mold with spatial variations of microstructure. The fabricated molds were tested, evaluated, and compared against traditional H13 steel molds, which are an industry standard.

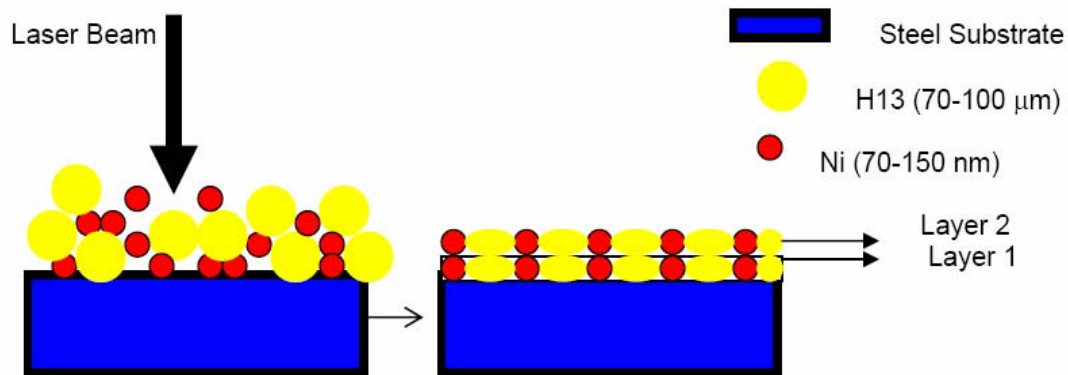


Figure 3.1 Schematic of nanoparticle additive manufacturing of two layers.

3.2 Background

The market for dies and molds is fiercely competitive, with a global size of US \$65 billion [5]. Dies and molds constitute a major portion of costs associated with manufacturing

operations such as injection molding, die-casting, stamping, extrusion and forging [6, 7]. For example, a stamping die for an automobile body costs \$2 million. Consequently, premature failures, including erosion, heat checking (thermal fatigue), oxidation and soldering must be prevented. The traditional die/mold manufacturing process involves detailed design features, part functionality and interfaces, tool path generation, selection of a steel like H13, CNC milling of concave/flat/convex surfaces, heat treating, electrical discharge machining (EDM) of cavities, coating and polishing (mechanical/chemical), quality control (geometry, tolerance, surface roughness and integrity) and parts tryout [5, 6]. Additionally, the machined mold often must be subsequently heat-treated and surface-treated/coated to impart the desired microstructure and properties. If improperly done, the heat treatment causes dimensional instability and generates residual stresses. Post-treatment operations such as grinding and EDM may also damage the surface integrity if improperly used. Alternatives to machining are powder-consolidation processes such as hot isostatic pressing (HIP), which uses rapidly solidified powders to produce dies and molds that outperform cast and machined tools. However, these processes are costly and require long lead times [8].

Solid freeform fabrication (SFF) processes, which have been actively pursued in recent years for direct manufacturing of dies and molds, offer benefits such as geometric flexibility, simplicity, rapid turnaround, and the environmentally benign nature of the process [9, 10]. Of all the techniques reported to date, only laser-cladding-based SFF (LC) processes are paving the way to generating direct metal tooling. However, such techniques are still in their infancy and are not commercially viable. LC technologies include: 1) directed light fabrication (DLF), from Los Alamos National Laboratory [11, 12]; 2) direct metal deposition (DMD),

from the University of Michigan [13]; 3) laser-engineered net shaping (LENS), from Sandia National Laboratory [14-16]; 4) shape deposition manufacturing (SDM), from Stanford University [17, 18]; 5) laser direct casting (LDC), from the University of Liverpool [19], and 6) laser-based flexible freeform fabrication (LBFF) from Iowa State University [20-22]. Among these, only LENS has reached sufficient maturity to enter the commercial market (Optomec LENSTM Model 750). The most common application of LENS is direct fabrication of injection molds. Although the LENSTM process has gained some commercial success, it is generally limited to a small number of metals. It also uses an Nd: YAG laser that has lower power and reliability ratings than the industrial workhorse, the CO₂ laser.

3.3 Experimental Procedure

3.3.1 Materials

AISI H13 is chromium hot-work die steel characterized by high degree of hot-strength, hardenability, toughness and thermal fatigue resistance. The nominal composition of H13 steel in weight percentage is Cr 5.23, V 0.96, Mo 1.43, Si 1.01, Mn 0.39 and C 0.39, with the balance Fe. It is preferred over other alloys for dies and molds [23] and is usually the standard material for laser-clad dies and molds because of its consistent flow during laser processing although residual stresses due to martensite transformation create harmful effects [13, 24].

In this work, H13 powders (70-100 μm) were obtained from Crucible Research, a division of Crucible Materials Corporation. Nickel powders (70-150 nm, Figure 3.2 (A)) were obtained from Argonide Nanometal Technologies. Nickel was selected as the dispersing element

because of its beneficial effects on strength, toughness, and corrosion resistance [25]. Nickel nanopowders were blended with H13 micropowders in the volumetric ratio of 1:4 to produce efficient nanoparticle dispersion. Hot-rolled AISI 1020 steel was used as the substrate on which successive layers of H13 /Ni layers were built.

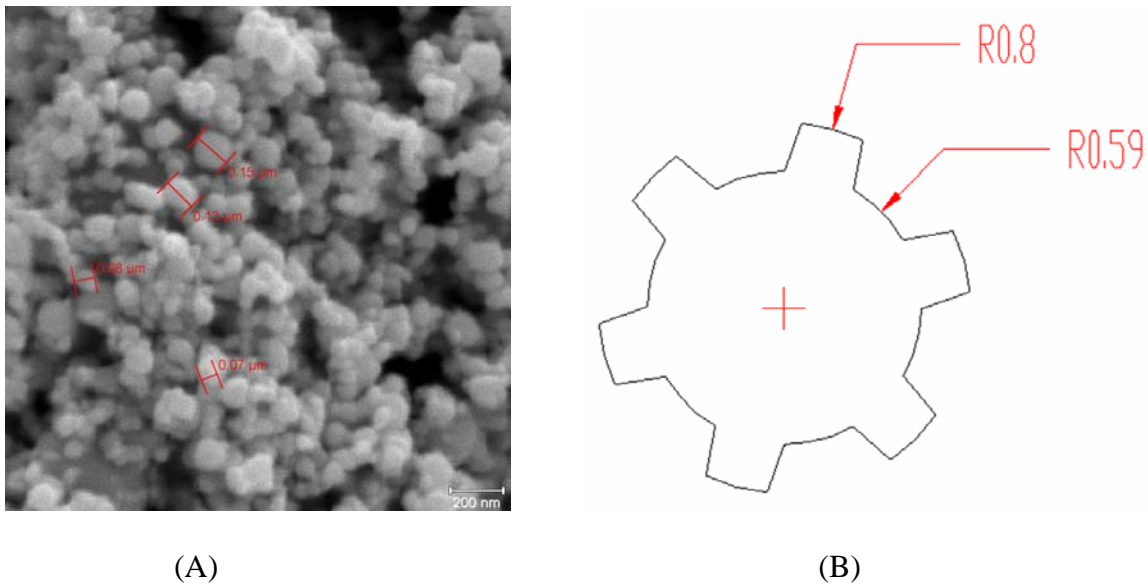


Figure 3.2 (A) Nickel nanopowders, (B) A schematic of mold geometry.

3.3.2 Mold Design

Spur gear geometry was selected for the mold design because, 1) it is widely used for injection molding of plastic gears in industry; 2) the complex (involute) geometry allows improved understanding of the uniformity of powder dispersion; and 3) its curved surfaces and taper impose stringent requirements regarding the molds ability to withstand stresses during injection molding. Figure 3.2 (B) is a sketch of the gear with its dimensions. The outside diameter of the gear was 40.64 mm (1.6 in.), the pitch circle diameter was 36.06 mm

(1.42 in.) and the inner diameter was 29.96 mm (1.18 in.). Thus the addendum and dedendum were 4.57 mm (0.18 in.) and 6.1 mm (0.24 in.) respectively. The gear's wall thickness was 2.25 mm (0.088 in) and its height 2.5 mm (0.098 in.).

The mold was designed in AutoCAD software. A 3D solid model, which is a geometric representation of the designed spur gear mold, was sliced into 2D “blocks” in the Z-direction for a layer thickness 0.2 mm using a CAD/CAM software. CNC codes were then created and used to direct the laser beam scanning in a raster pattern within the boundaries defined by the slices. The laser machine bed moved in the X- and Y-directions. This, in combination with the motion of the laser optics in the Z-direction, paved the way for the generation of the 3D spur gear mold structure.

3.3.3 Powder Feeding

In laser cladding, two methods are generally used to feed the powder [26]. One is to pre-place a powder bed on the substrate and then allow the laser beam to melt the low thermal conductivity powder before melting the high thermal conductivity substrate. Here, the bed depth is a critical parameter for good metallurgical bonding. In the second method, powder is delivered through a pneumatic feeder into the laser-generated molten pool. Table 3.1 summarizes the benefits and drawbacks of these two methods and illustrates the advantages of the powder delivery method. However, in this work, attempts to use the powder delivery method were not successful because the nanopowder flow was unstable and disorderly. Hence, we resorted to the powder bed method, in which a layer was placed and then leveled off for a thickness of 1 mm and in which no attempt was made to pack down the powder

layer. The powder was uniformly spread across the substrate for each pass of the laser. This method was adopted for both the Ni-H13 composite and the H13 micropowder gear molds.

Table 3.1 Comparison of two powder feeding methods.

Characteristic	Powder Bed	Powder Delivery
Beam energy absorption	Higher	Lower
Melting	Top to bottom	Bottom to top
Control of dilution	Inferior	Superior
Specific energy required	Higher	Lower
Bonding integrity	Poor	Good
Complex geometry	Difficult	Acceptable
Cover gas effectiveness	Less	More

3.4 NAM Process

Figure 3.3 displays the schematic setup of NAM process, which uses a 1500 W continuous wave CO₂ laser to melt the blended powders on the substrate, with little dilution into the substrate. The laser beam scanned the steel substrate, with its pre-placed powder bed, according to the gear profile and tool paths obtained through use of CAD/CAM software. Table 3.2 lists the process parameters used. Because each laser scan produced a layer of about 0.2 mm, a dozen scans were used to produce a thickness of 2.25 mm. A CNC mill was then used to remove the supporting material (1020 steel) from the fabricated parts so that the molds could be used in injection molding.

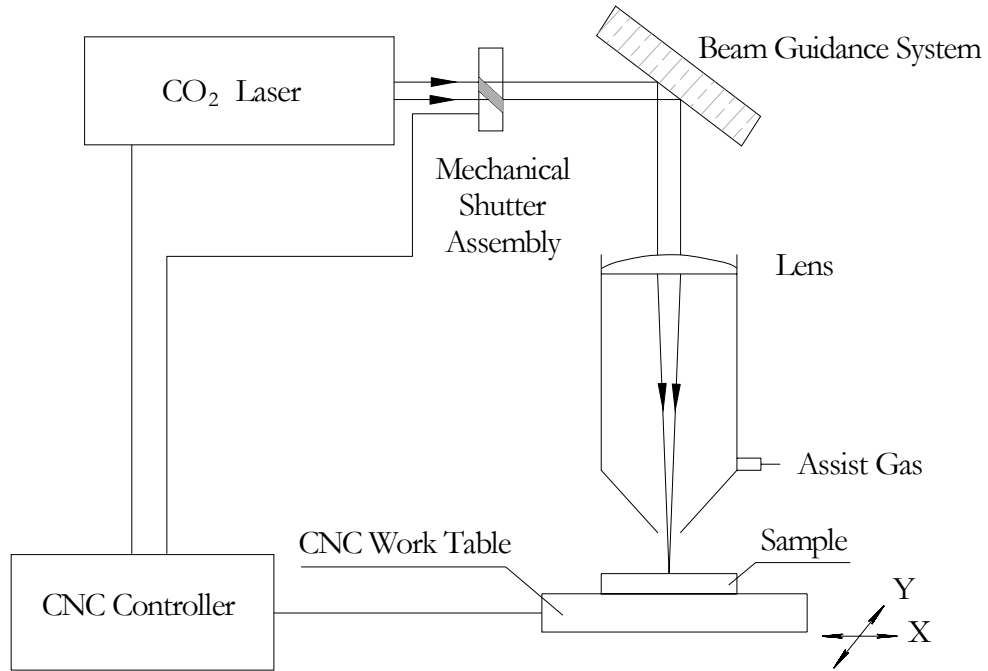


Figure 3.3 A schematic for the NAM process.

Table 3.2 Process parameters for the fabrication.

Parameter	Value
Laser Power, Watt	550
Focal length of lens, mm	191
Spot radius at the powder surface, mm	0.8
Scanning speed, mm/sec	4.2
Standoff distance from the nozzle to the substrate, mm	15
Overlap among passes, %	25

3.5 Characterization and Testing

A surface profilometer with a diamond stylus of 0.025 mm diameter was used to measure the arithmetic average value, R_a , of the roughness of the inside surface. Metallography was performed by sectioning, polishing and etching the molds in a 4% nitric acid solution. Scanning electron microscopy (JEOL JSM35, 10 kV) was then used to examine the flaws (porosity and cracks) and to characterize the dispersion and microstructure of the molds. Hardness (Rockwell C scale) on the top surfaces of the molds was measured by use of a Wilson/Rockwell series 500 hardness tester. Vicker's microhardness measurements were also conducted along the transverse sections. Certified calibration blocks were used to verify the hardness measurements. Corrosion tests of the molds were also performed to evaluate corrosion resistance in 10% HCl solution with intermittent stirring for a period of five hours while measuring the weight loss every hour.

Injection molding was conducted to determine the mold relief ability, the presence of macro-defects and the ability to resist stress deformation. A Boy 30M injection molder was used for the injection process. Polystyrene was the injection material. A Brown and Sharpe coordinate measuring machine (CMM) was then used to measure the extent of mold deformation. Injections were restricted to 10 per mold, owing to the difficulty in removing the plastic gears from the molds. The injection temperature and pressure were set to 210⁰C and 100 bars respectively.

3.6 Results and Discussion

3.6.1 Analysis of Molds

Figures 3.4A and B show the photographs of nanocomposite and straight H13 steel gear molds, respectively, fabricated on hot-rolled AISI 1020 steel substrate, machined on the top surface ready for injection molding. The molds have tapers both inside and outside. The inside taper was intentionally added to aid in removal of the plastic gears later in injection molding. However, the outside taper, which was unintentional, was caused by shrinkage in the solidification process. Introducing a “compensation” offset in CNC programming can eliminate the outside taper.

Visual examination of the molds revealed excessive material deposition at the program starting and end points, and some partially melted powders on the walls. This is normal considering the intrinsic characteristics of the CNC programming and the powder bed method. Excessive material was deposited because the beam was programmed to move inward or outward for an increment after it finished a cycle at a given position. The sudden change in direction of movement made the beam dwell longer at these points than at others, which produced thicker layers. Two processes were used to correct this unevenness: shifting of the point to different peripheral positions during laser processing and post surface grinding.

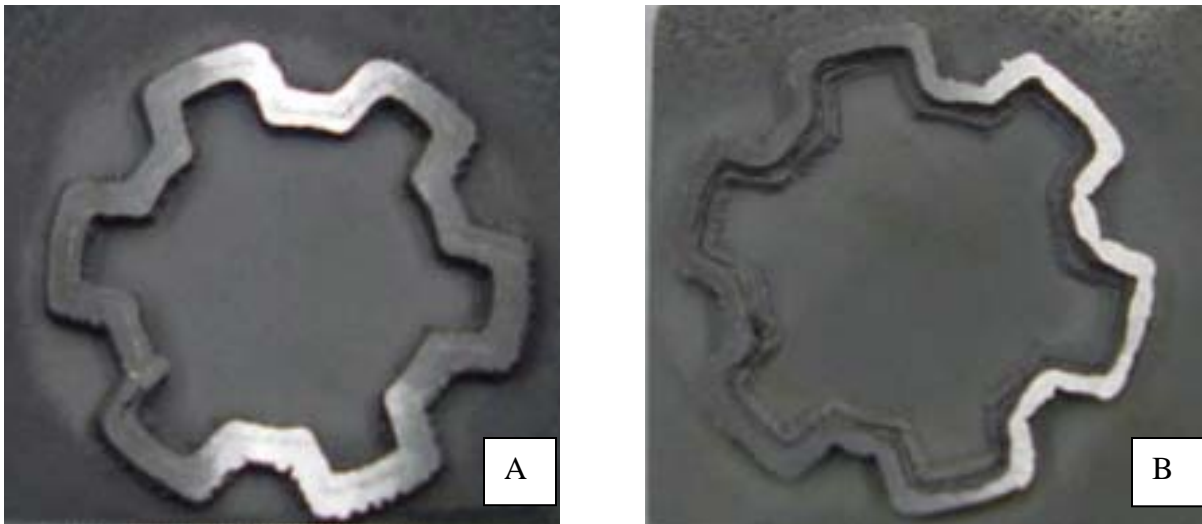
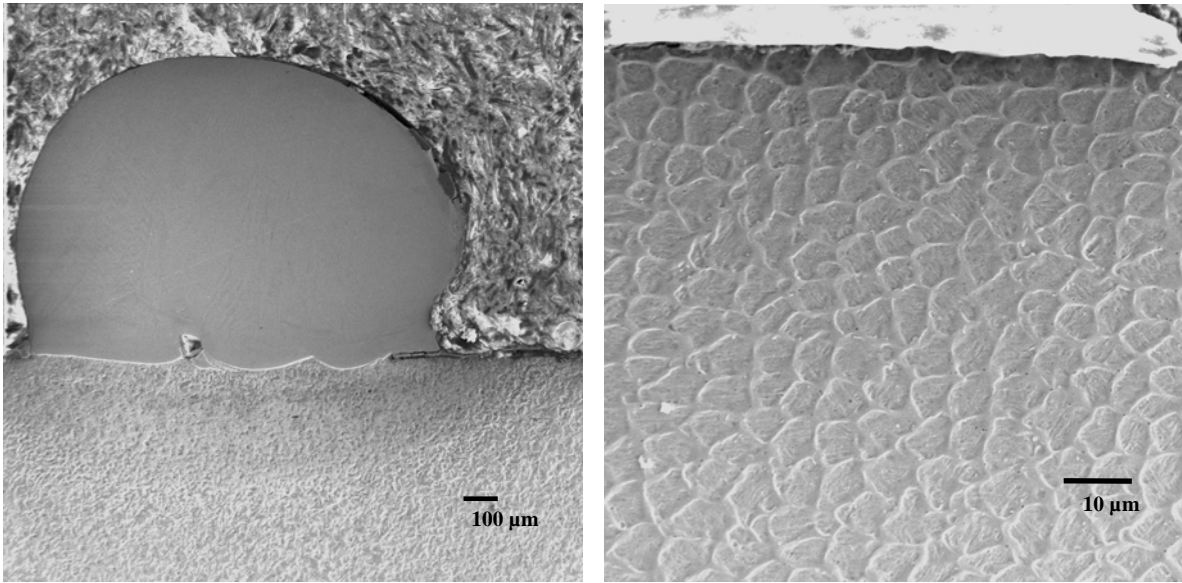


Figure 3.4 Photographs of A) Ni/H13 steel mold, B) H13 steel mold.

Surface roughness of the inside walls of molds showed an average surface roughness (R_a) of 286 μm for the nanocomposite mold and 416 μm for the H13 steel mold, which represented some improvement of surface finish by use of nanopowders. The poor surface roughness is attributed to the formation of partially melted particles, smaller percentage of overlap, powder bed uniformity, thermal conductivity differences of powder and substrate, and beam energy distribution. However, the surface roughness can be improved by switching the powder bed process to the powder delivery system [27]. Optical and scanning electron microscopy examination of the molds did not reveal defects such as porosity, inclusions and cracks, which implies that NAM is capable of producing molds with near-theoretical density. The absence of interfacial porosity (a common problem in laser cladding) is attributed to the material combination of powder and substrate. Since both powder and the substrate are primarily steels with nearly the same melting temperature, the solidification front ends up at the top surface instead of at the interface, thus avoiding interfacial porosity.

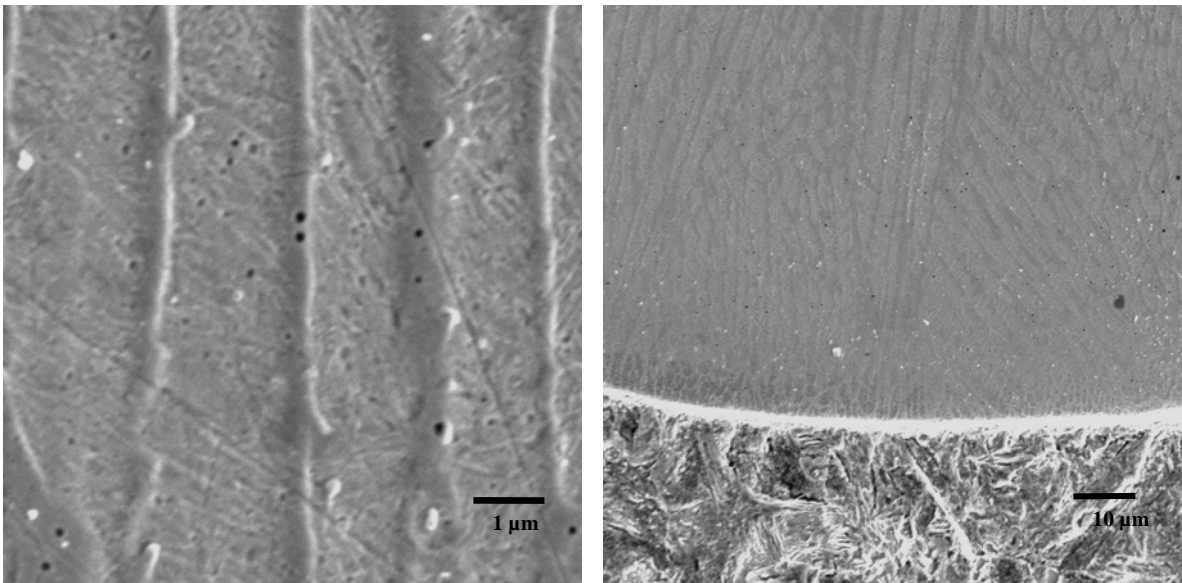
3.6.2 Solidification Structures of Molds

The solidification microstructures of NAM molds are complex and varied, as one might expect with use of a rapid solidification process. Figure 3.5 shows electron micrographs of a single-layer in the z -direction (height of the build). Figure 3.5A shows the single-track clad layer, while Figures 3.5B to D depict the solidification structures of axial cross sections (transverse to the wall thickness) from top to bottom. The morphology of these structures is determined by the thermal gradients and cooling rates in and around the molten pool. The top layer shows cellular structure, reflecting the relatively low temperature gradient and cooling rates. The bottom (interface) layer shows very fine columnar dendrite structures caused by the epitaxial growth and the rapid heat dissipation from the melt pool through the substrate. Columnar grain structure is predominantly present in the middle layer, suggesting that solidification proceeds from the bottom to the top by the conduction mode of heat transfer. Figure 3.6 shows that the dendrites and cells were finer because of the lower laser power levels used in this work. The secondary dendrite arm spacing was widely used to estimate the cooling rate of H13 steel by the equation: $dT/dt = 3.87 \times 10^{-13}/x^3$ where dT/dt = cooling rate in K/sec and x = spacing in meters [13]. This expression yields a cooling rate on the order of 10^4 K/sec for the arm spacing of 4-7 μm obtained in this study.



(A)

(B)



(C)

(D)

Figure 3.5 Scanning Electron Micrographs (SEM) of H13-Nickel nanocomposite gear mold, a) Single clad track, b) Equiaxed cellular structure at the top, c) Columnar dendrite in the middle, and d) Fine epitaxial growth at the bottom (interface). Etchant used was 4% Nital.

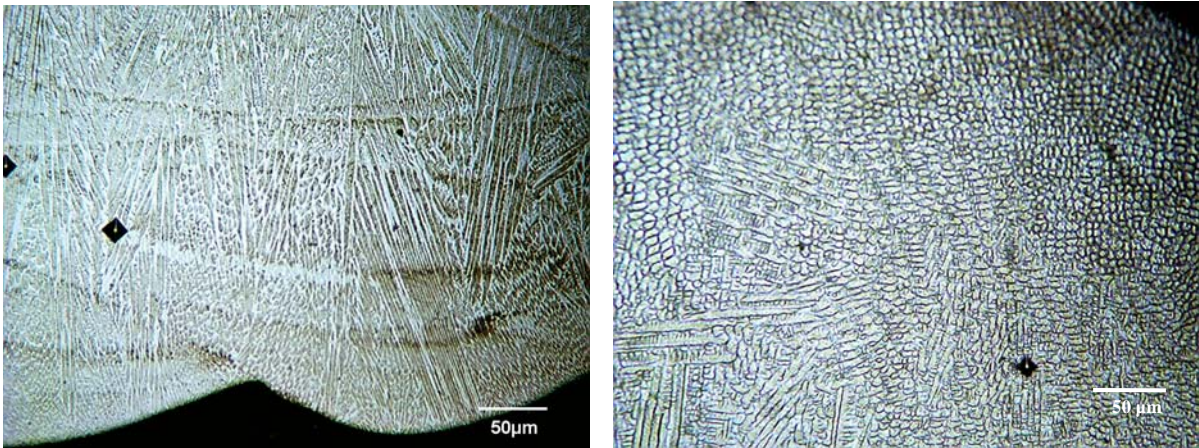


Figure 3.6 Optical micrographs of heavily-etched samples showing the cellular-dendrite structures. Note also the Vicker's hardness indentations.

3.6.3 Composition and Microstructure of Molds

Figure 3.7 shows the dispersion of nanoparticles (black particles) in the steel matrix. Since these particles were clearly observed in the polished condition, any suspicion that they were etch pits was laid to rest. The average chemical composition of the mold, in weight percentages, estimated from the energy dispersive spectra (SEM/EDAX) of the molds, were Ni 5.7, Cr 4.0, Si 0.65, V 0.9, and Mo 0.95, with the balance Fe. Because of the addition of Ni, there was a decrease in all the alloying elements of the H13 steel.

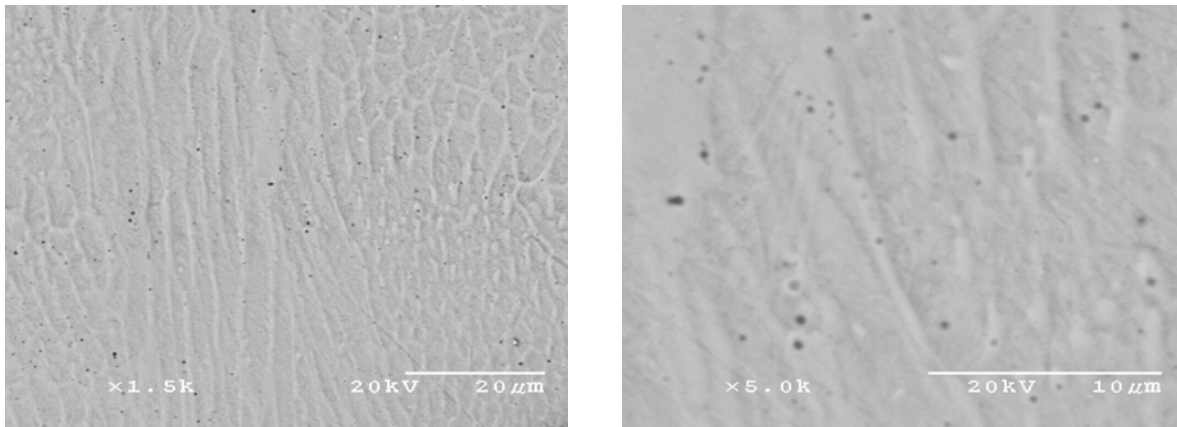


Figure 3.7 Low and high magnification SEM micrographs showing the dispersion of nanoparticles in the steel matrix.

SEM/EDAX spot analysis confirmed that these particles are composed of Ni and small amounts of Si. Figure 3.8 shows the particles and the X-ray spectrum of nanoparticle. The dotted line in Figure 3.8B comes from those of the whole region. Such X-ray spectra must be interpreted with some caution. One must understand that the solid line in the spectrum also includes the emission of elements from bulk, because the X-ray penetration depth in the sample exceeds the particle size. Compared to other elements such as Cr, Mo, and V in H13 steel, the preferential diffusion of Si into the Ni-nanoparticles is quite intriguing and might be understood by its atomic size and solubility. Silicon has a very small atomic radius and a higher self-diffusion coefficient, both of which aid in rapid diffusion into nickel [28]. In addition, the solubility of Si in Ni is quite high as evident from the Ni-Si phase diagram, which shows the formation of several phases: NiSi, NiSi₂, Ni₃Si₂, and Ni₅Si₂. Figure 3.9 shows a typical grain structure of the gear mold. The small grain size (2-4 μm) illustrates the rapid solidification associated with laser processing as well as the ability of nanoparticles to prevent grain growth.

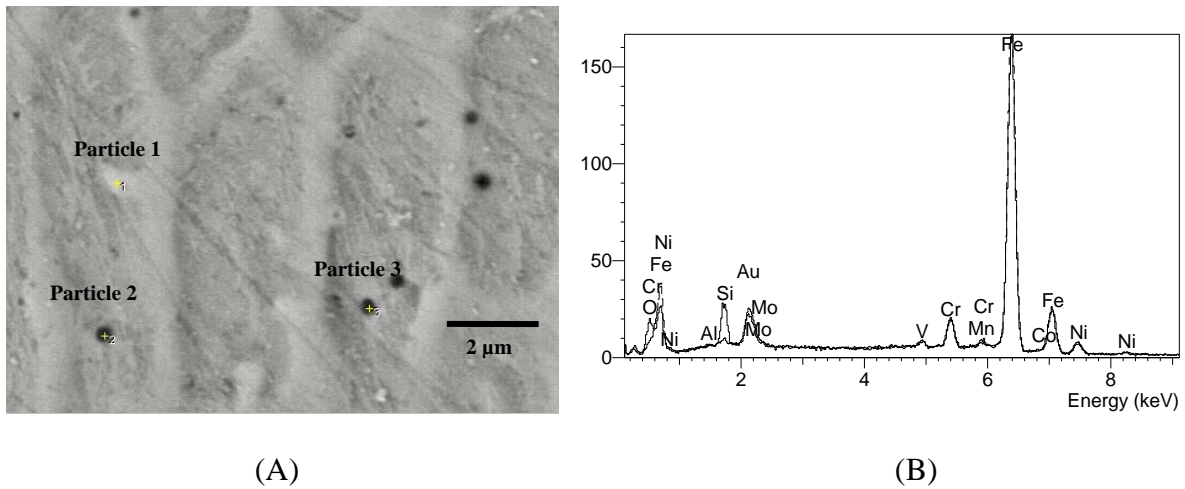


Figure 3.8 (A) SEM micrograph showing the nanoparticles, (B) EDAX spectrum of the black nanoparticle (solid line). Dotted line is the spectrum of overall alloy.

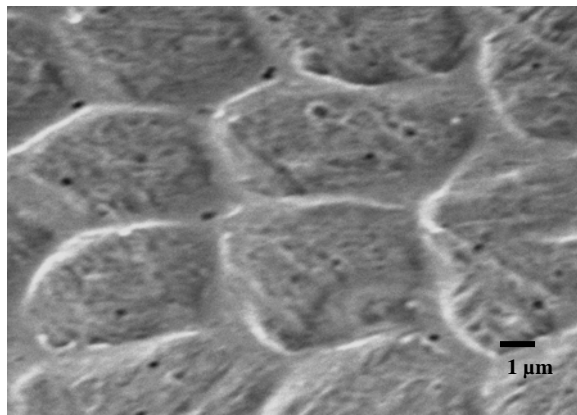
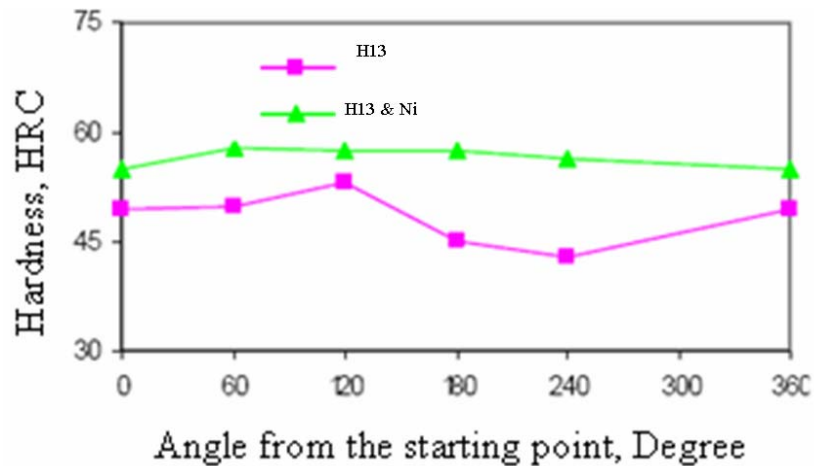


Figure 3.9 Grain structure of nanocomposite mold.

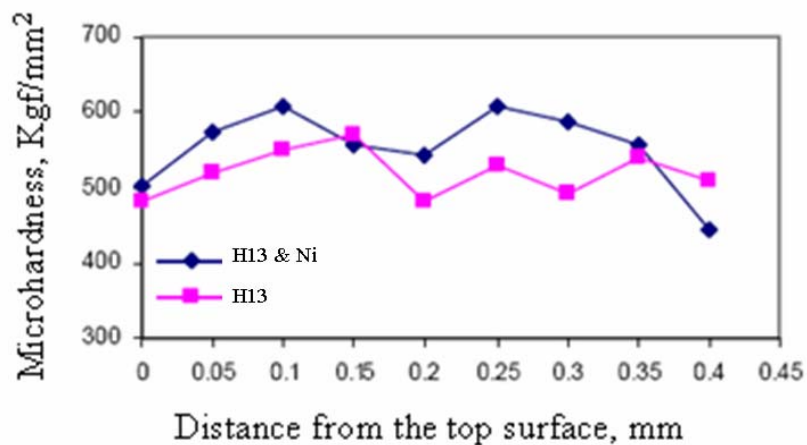
3.6.4 Hardness and Corrosion Resistance

Figures 3.10 (A) and (B) display the hardness data. The hardness in the peripheral region for H13/Ni molds is higher than H13 molds by about 5 to 10 points in Rockwell C scale. Hardness measurements along the top and bottom surface revealed no discernible differences, consistent with the uniformity of microstructure through the axial direction. Figure 3.10 (B) shows the Vickers microhardness along the depth for a sample with single-

layer of about 0.4 mm. The hardness of nanoparticle-dispersed molds exceeded that of H13 mold by 50 points, indicating a similar pattern. Corrosion test data of both molds in 10% HCl acid medium, shown in Figure 3.11, revealed that the weight loss per surface area for H13-Ni mold was more than two times higher than that of the H13 mold.



(A)



(B)

Figure 3.10 (A) Rockwell hardness C scale for H13 and H13/Ni nano molds (Scatter \pm 3%), (B) Variation of microhardness with distance from the top surface of single-layer mold of about 0.4 mm (Scatter \pm 4%).

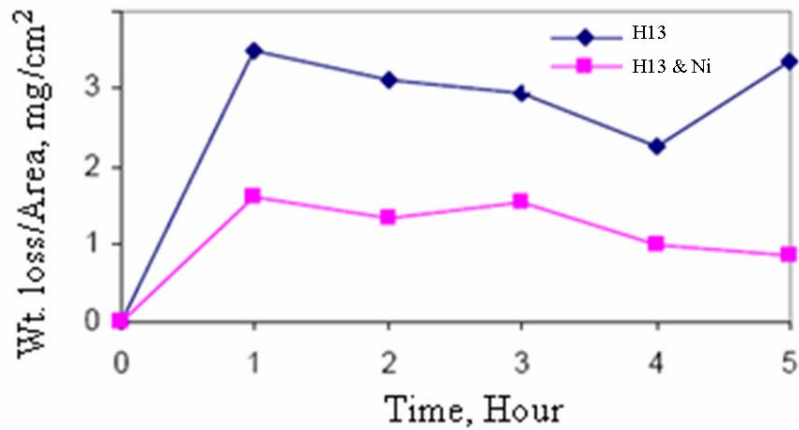


Figure 3.11 Weight loss of molds with immersion time in 10% HCl.

3.6.5 Injection Molding Data

Injection molding tests showed that the injected polystyrene blocks could not be easily ejected from the cavities although a relief angle was present in both molds. This may be due to the poor surface finish at the inner surfaces. In total, 10 shots were made per mold. CMM measurements on the deformation at the bottom of the molds showed that, up to 10 shots, the plastic deformation was insignificant. Also there was no evidence of wear. A higher abrasive resistant material than polystyrene and a large number of shots are necessary to identify the effect of nanoparticles on the abrasive wear resistance molds. Plastic gears produced had acceptable tolerance and surface roughness among both H13 and H13-Ni molds although the latter provided improved finish and tolerance.

3.7 Conclusions

The following conclusions are based on the experimental results obtained when nanoparticle additive manufacturing was applied to the freeform fabrication of the molds:

- (1) NAM is a successful process of dispersing Ni-nanoparticles in H13 steel melt and producing injection molds with excellent structural integrity, higher hardness and increased corrosion resistance.
- (2) Nanoparticles have improved the surface finish of fabricated molds.
- (3) Limited functionality tests of the NAM molds revealed their potential for long-life and high performance.

Acknowledgements

The authors would like to thank Dr. Warren Straszheim for help on obtaining SEM pictures and Larry Couture and Larry Hanft for their assistance.

References

1. World Technology Evaluation Center, (1997). R&D status and trends in nanoparticles, nanostructured materials, and nanodevices in the U.S. *Proceedings of the May 8-9 Workshop*, <http://itri.loyola.edu/nano/US.Review/toc.htm>, Retrieved – March, 1st, 2003.
2. Goldstein, A. N. (1997). *Handbook of Nanophase Materials*. Marcel Dekker, Inc., NY.
3. Chaudhari, R. (2000). *Handbook of Nanostructured Materials and Technology*, Marcel Dekkar, Inc.

4. Manthiram, A., Bourell, D. L. and Marcus H. L. (1993). Nanophase materials in solid freeform fabrication. *Journal of Metals*, November, pp. 66-70.
5. Altan, T., Fallbohmer, P. and Rodriguez, C. (2000). HSM Research - On the edge of technology. *Engineering Research Center for Net Shape Manufacturing*, The Ohio State University, USA, <http://www.mmsonline.com/articles/hsm9801.html>, Retrieved – March, 1st, 2003.
6. Altan, T., Fallbohmer, P., and Rodriguez, C. (1998). *Modern Machine Shop*, January Issue.
7. Fallbohmer, P., Altan, T., Tonshoff, H. K., and Nakagawa, T. (1996). Survey of the die and mold manufacturing industry. *Journal of Materials Processing Technology*, Vol. 59, pp. 158-168.
8. Agarwala, M., Klosterman, D., Osborne, N., Lightman, A., Dzugan, R., Rhodes, G. and Nelson, C. (1999). Hard metal tooling via SFF of ceramics and powder metallurgy. *Solid freeform Fabrication Proceedings*, Austin, TX, pp. 759-766.
9. Hull, C., Feygin, M., Baron, Y., Sanders, R., Sachs, E., Lightman, A. and Wohlers, T. (1995). Rapid prototyping: Current technology and future potential. *Rapid Prototyping Journal*, Vol. 1, No. 1, pp. 11-19.
10. Kochan, A. (1997). Rapid prototyping trends. *Rapid Prototyping Journal*, Vol. 3, No. 4, pp. 150-152.

11. Milewski, J., Lewis, G. K., Fonseca, J., and Nemeč, R.B. (2000). Laser powder deposition of a near net shape injection mold core-a case study. *Materials and Manufacturing Processes*, Vol. 15, No. 2, pp. 247-258.
12. Milewski, J., Lewis, G. K., Thoma, D. J., Keel, G. I., Nemeč, R. B., and Reinert, R. A. (1998). Direct light fabrication of a solid metal hemisphere using 5-axis powder deposition. *Journal of Materials Processing Technology*, Vol. 75, pp. 165-172.
13. Mazumder J., Choi J., Nagarathnam K., Koch J. and Hetzner D., (1997). The Direct Metal deposition of H-13 Tool Steel for 3-D Components. *Journal of Metals*, Vol. 49, No. 5, pp. 55-60.
14. Anon, C. H. (1998). Direct metal fabrication. *Rapid Prototyping Report*, Vol. 8, No. 3, pp. 3-5.
15. Anon, C. H. (1998). Metals Update. *Rapid Prototyping Report*, Vol. 8, No. 10, pp. 3-5.
16. Griffith, M. L., Keicher, D. M., Atwood, C. L., Romero, J. A., Smugeresky, J. E., Harwell, L. D., and Greene, D. L. (1996). Freeform fabrication of metallic components using laser engineered net shaping (LENS). *Solid Freeform Fabrication Proceedings (D. L. Bourell, J. J. Beaman, H. L. Marcus, R. H. Crawford, and J. W. Barlow, eds.)*, The University of Texas at Austin, August, pp. 125–132.
17. Fessler, J. R., Merz, R., Nickel, A. H., and Prinz, F. B. (1996). Laser deposition of metals for shape deposition manufacturing. *Solid Freeform Fabrication Proceedings (D. L. Bourell, J. J. Beaman, H. L. Marcus, R. H. Crawford, and J. W. Barlow, eds.)*, Proc. 1996 Solid Freeform Fabrication Symposium, Austin, August, pp. 117–124.

18. Link, G. R., Fessler, J. R., Nickel, A. H. and Prinz, F. B. (1998). Rapid tooling die cast inserts using shape deposition manufacturing. *Materials and Manufacturing Processes*, Vol. 13, No. 2, pp. 263-274.
19. Irving, R., (1999). Taking a Powder: Metallurgy and lasers are cooking up new methods for manufacturing. *Mechanical Engineering*, September, pp. 55-59.
20. Jiang, W. and Molian, P. A. (2001). Laser-based flexible fabrication of functionally graded mould inserts. *International Journal of Advanced Manufacturing Technology*, Vol. 19, pp. 646-654.
21. Jiang, W. and Molian, P. A. (2002). Production of H13 steel extrusion dies by laser freeform fabrication. *North American Manufacturing Research Conference, NAMRC*.
22. Jiang, W. and Molian, P. A., (2001). Nanocrystalline TiC alloying and glazing of die-casting dies using a CO₂ laser for improved life and performance. *Surface Coatings and Technology*, Vol. 135, No. 2-3, pp. 139-149.
23. Li, G., Li, X. and Wu, J. (1998). Study of the Thermal Fatigue Crack Initial Life of H13 and H21 Steels. *Journal of Materials Processing Technology*, Vol. 74, pp. 23-26.
24. Mazumder J., Schifferer A. and Choi J. (1999). Direct Materials Deposition: Designed Macro and Microstructure. *Material Research Society Symposium Proceedings*, Vol. 542, pp. 51-63.
25. Budinski, K. G. (1996). *Engineering Materials: Properties and Selection*, Prentice Hall Inc., NJ 07632.

26. Eboo G. M. and Lindemanis A. E. (1985). Advances in laser cladding process technology. *Applications of High Power Lasers, The International Society for Optical Engineering*, Vol. 527, pp. 86-94.
27. Jiang, W. (2002). Experimental and analytical studies of a CO₂ laser-based flexible fabrication method for dies and molds. *PhD dissertation*, Mechanical Engineering Department, Iowa State University, Ames, Iowa.
28. Smithells C. J. and Brandes E. A. (1992). *Metals reference book*, Butterworth & Co. (Publishers) Ltd.

**CHAPTER 4. Functionally Graded Mold Inserts by Laser-based Flexible Fabrication:
Processing Modeling, Structural Analysis, and Performance Evaluation**

Paper published in *Journal of Materials Processing Technology*, 166(2), 2005

Rajeev Nair, Wenping Jiang and Pal Molian

Abstract

Laser-based flexible fabrication (LBFF), a novel solid freeform fabrication method based on the principles of laser cladding, was developed to produce functionally graded mold inserts using shaped laser beams, quasi-coaxial nozzle for powder delivery, and functionally graded materials. As a case study of this innovative method, a hollow square mold insert was fabricated with additive layers of H13 steel, Ni/Cr alloy, and TiC using circular and rectangular beam profiles. Finite element analysis using ANSYS[®] was applied to determine temperature fields and thermal gradients associated with circular and rectangular beams. The microstructures and interfaces were examined using a scanning electron microscope, and related to the temperature gradients. Characterization results show a nearly full-density mold with excellent integrity, beneficial microstructures, strong interfaces, and high hardness. In addition, the mold insert was tested and compared to H13 steel molds in a thermal fatigue environment for ability to resist crack initiation, thermal strain, and oxidation.

4.1 Introduction

Solid Freeform Fabrication (SFF) is an advanced manufacturing technology designed to make solid physical models directly from 3D-CAD data representation without special tooling. It uses material addition technology to produce concept models, prototypes, and

tooling for manufacturing dies and molds [1]. SFF offers benefits such as reduction in lead-time, ability to make complex components, and cost savings [2]. However, fabrication of functionally metallic and ceramic components by use of SFF still remains elusive. Initially, selective laser sintering (SLS) of powder materials seemed to have the potential to produce functional prototypes, even for direct tooling fabrication [3, 4]. However, SLS required polymer binders and low-melting compounds. Shrinkage, porosity, and low density of parts are the drawbacks of SLS that prevent it from competing against machining and EDM for mold fabrication. Laser cladding (LC) based freeform fabrication technology has emerged as a promising approach to remedy the deficiencies in SLS. LC consists of pneumatically injecting powders through a quasi-coaxial nozzle into a laser-created molten pool of substrate or by laser melting pre-placed powders. Subsequent solidification forms strongly bonded layers of fully dense and possibly homogeneous microstructures. LC offers several advantages including flexibility in processing structural materials, fine grain structure, low dilution, minimal thermal degradation, formation of non-equilibrium crystalline and amorphous structures, and extension of solid solubility of alloying elements [5].

LC was applied in multiple, overlapping layers to create functional 3D objects [6-8]. Several LC-based SFF processes with minor variations were developed [9-14]. These include: 1) directed light fabrication (DLF) from Los Alamos National Laboratory [9, 10]; 2) direct metal deposition (DMD) from the University of Michigan [11]; 3) laser engineered net shaping (LENS) from Sandia National Laboratory [12]; and 4) shape deposition manufacturing (SDM) from Stanford University [13]. Despite such significant development, the LC-based SFF processes suffer from drawbacks including unsatisfactory surface finish,

residual stresses, low dimensional accuracy, porosity, and crack formation [15]. As a result, this technology could not be implemented in industry. A number of experimental and numerical studies were conducted to understand the LC-based SFF processes. Kobryn *et al.* [16] investigated the effect of laser power and traverse speed on the formation of built height and porosity in laser deposition of Ti-6Al-4V using a factorial experiment. Vasinonta *et al.* [17] developed process maps for fabricating thin-walled sections using AISI 304 stainless steel with emphasis on stress-induced warping. Kaplan and Groboth [18] analyzed laser beam cladding of Stellite-6 powder process using simplified energy and mass balance equations.

To produce high-performance functional components such as molds and dies that are free of the defects mentioned above, a novel LC based SFF technique, namely, laser-based flexible fabrication (LBFF), has been developed. This technique is different from others such as LENS in the following aspects: 1) use of materials to make parts with functionally graded composition and microstructure; 2) application of shaped laser beams to produce desired surface finish and dimensional tolerance, and to reduce residual stresses and dilution in the functional layers; and 3) use of a quasi-coaxial nozzle for powder delivery [16]. Since LBFF involves direct interactions between moving heat source and powder materials, the phenomena of mass transport (powder), heat transfer, and fluid flow make it rather complex. For the processing conditions be optimally chosen to produce parts with high integrity (in terms of surface roughness, crack, and porosity) and mechanical properties, such as hardness and toughness, which are primarily dependent upon microstructures, it is important to understand the underlying physical mechanism associated with the process. Hence,

ANSYS® was used to solve the heat transfer problem related to the fabrication process and to map out the temperature distribution and temperature gradients that are essential to predict the molten pool dimensions, layer depth, type of microstructure, and thermal distortion. In this paper, the production, process modeling, characterization, and evaluation of the FGM mold inserts associated with the novel LBFF process are presented.

4.2 Experimental Materials and Methods

Figure 4.1 shows a schematic of LBFF, where shaped beams are used to make functional objects from CAD files and CNC programming by controlled laser melting of the localized powders of different materials in a functionally graded manner. Micro-sized powders of TiC (2 μm), Ni/Cr alloy (100 μm), and H13 (70~100 μm) were used as construction materials in this work because they exhibit the desired mechanical and physical properties of die and mold materials. TiC, a ceramic coating material with low thermal conductivity, is capable of increasing die- and mold-operative temperature, while maintaining a low temperature at the die surface. Ni/Cr alloy serves as the intermediate metallic layer (mainly due to diffusion) between TiC and H13 layers. Its major functions are to further reduce oxidation and high-temperature corrosion of the H13 layer as well as to improve the adhesion between these layers [20, 21]. H13 is a benchmark material for dies and molds. In addition, these materials also have closely matching thermal expansion coefficients [21], minimizing crack formation and improving adhesion during processing. The addition of materials in creating the inserts was configured in such a way that each side was composed of TiC, Ni/Cr alloy, and H13 powder, respectively, from outside to inside. Through these combinations, high surface hardness and core toughness were anticipated.

A 30 mm square-shaped geometry was chosen as die insert design, with a wall thickness of 8 mm. The maximum building height of parts was varied depending on the width of overlapped track, thickness of single layer, and number of layers deposited. A high-power, continuous wave (CW) CO₂ laser with beam configurations of circle and rectangle was used to melt the powders, introduced through a powder delivery system on H13 steel substrate. First, H13 powders were laser melted and solidified to a thickness of 6.2 mm. Second, Ni/Cr alloy was deposited for a thickness of 1.5 mm. Defocused circular beams (15 mm below focal plane) with a diameter of 0.8 mm were used in both cases. Third, TiC was formed to a thickness of 0.3 mm using a focused rectangular beam of size of 0.1 mm × 1 mm. The rectangular beam offered a high degree of surface integrity compared to the circular beam.

The fabricated inserts were cleaned up, sectioned, polished and etched for characterization of microstructure and composition by SEM. Vickers microhardness (1.0 *kgf*) test was used to determine the hardness distribution across the mold and compared with the benchmark H13 mold. Additionally, a low cycle thermal fatigue experiment was performed on both a H13 mold and the functionally graded mold of same geometries and dimensions, to compare their performance in accordance to crack initiation, thermal strain, and oxidization resistance. The molds were put in a high-temperature (850 °C) Lindberg heat treatment furnace and held for 3 minutes, then quenched in water at room temperature (20 °C) for one cycle. The molds were checked under a microscope of 30× for any cracks at designed intervals. The cycles were repeated till cracks initiated at any of the molds.

4.3 Process Modeling

4.3.1 Problem description

The first law of thermodynamics states that thermal energy is conserved. For a differential control volume associated with laser beam melting of pre-placed H13 powder, if the effect of heat losses from convection and radiation are nullified, and latent heat is neglected, then heat transfer problem can be mathematically described as:

$$\rho C \frac{\partial T}{\partial t} + \{L\}^T \{q\} = 0 \quad (1)$$

in which ρ is temperature dependent density; C is specific heat; T is temperature; and t is time; L represents the divergence operator; q is the heat flux related to the thermal gradients by Fourier's law:

$$\{q\} = -[D]\{L\}T \quad (2)$$

where, $[D] = \begin{bmatrix} k_x & 0 & 0 \\ 0 & k_y & 0 \\ 0 & 0 & k_z \end{bmatrix}$ is conductivity matrix. If material is homogeneous, then there

is $k_x = k_y = k_z = k$. Combining equations (1) and (2), we have:

$$\rho(T)C(T) \frac{\partial T}{\partial t} = \frac{\partial}{\partial x} \left(k(T) \frac{\partial T}{\partial x} \right) + \frac{\partial}{\partial y} \left(k(T) \frac{\partial T}{\partial y} \right) + \frac{\partial}{\partial z} \left(k(T) \frac{\partial T}{\partial z} \right) \quad (3)$$

This equation, based on the global Cartesian system, is used for solving the surface thermal gradients of circular and rectangular beams. Since we are only interested in surface thermal gradients, equation (3) can be reduced to:

$$\rho(T)C(T) \frac{\partial T}{\partial t} = \frac{\partial}{\partial x} \left(k(T) \frac{\partial T}{\partial x} \right) + \frac{\partial}{\partial y} \left(k(T) \frac{\partial T}{\partial y} \right) \quad (4)$$

with initial condition: $T(\pm\infty, y, t) = T(x, \pm\infty, t) = T(x, y, 0) = 293 \text{ K}$; and boundary condition:

$$x^2 + y^2 \leq R_b^2, \frac{\alpha P}{\pi R_b^2} = \text{constant}; \text{ in other areas, heat flux} = 0.0.$$

The solution of non-linear equation (4) is dependent upon temperature-dependent density, specific heat, and thermal conductivity. The powder material, H13, used in this computation is assumed to have the physical properties of bulk material. Since the temperature-dependent properties of H13 are only available up to a temperature of 600°C (873 K), for its properties at any temperature, higher than 600°C and lower than its melting point, are taken as the values at 600°C . Table 4.1 lists the variation of thermal properties with temperature for H13 steel.

4.3.2 Solution

In this study, ANSYS[®], the widely used finite element analysis software package, was applied to solve the aforesaid non-linear heat conduction problem of laser melting the pre-placed H13 powder. Plane elements (2D solid) of 6 nodes and 4 nodes were chosen for meshing the computation domains of circular and rectangular beams, respectively. The domain was a rectangle of 60 mm in length and 30 mm in width. Only a quarter of the rectangle was considered due to the symmetrical characteristics of the domain geometry and load. Element edge length was set to $6.25 \times 10^{-5} \text{ m}$ within the beam, $1.5 \times 10^{-3} \text{ m}$ for all other regions. In the regions adjacent to the beam, elements were refined. The meshes for surface thermal gradient computation corresponding to circular beam and rectangular beam are illustrated in Figure 4.2. Laser energy is assumed to be uniform over the beam profiles. The related basic load settings for the computations related to ANSYS are listed in Table 4.2.

4.4 Results and Discussion

4.4.1 The square mold insert fabricated by LBFF

Figure 4.3 shows a photograph of the functionally graded mold insert in which visual and scanning electron microscope (SEM) examination revealed few defects such as porosity, indicating nearly full density. The time for fabricating this die insert was 56 min.

In this fabrication process, the laser power was set between 500~600 W as powers greater than the above values tend to produce layers with poor surface integrity. Scanning speeds were set as 5, 8.5, to 42 mm/s for Ni/Cr alloy, H13, and TiC powder, respectively. Under these processing conditions, energy density ($\frac{P}{VD}$) for metal powders (73.5 for H13 and 150 J/mm² for Ni/Cr powder) was much higher than that for TiC powder (33 J/mm²) due to large surface area from the reduced size of TiC particles, leading to enhanced absorption of laser beam. The deposition layer thickness for H13 and Ni/Cr alloy powder per laser scan was 0.13 mm, while it was only 0.008 mm for TiC. All these deposition thickness yielded good surface roughness.

4.4.2 Surface thermal gradient profiles of shaped beams

As heating sources, laser beams of the same intensity but of shaped geometry can produce thermal gradients of different magnitude and distribution (Figure 4.4). At a typical power density of 9.4×10^7 W/m² (corresponding to laser power of 500 W on rectangular beam) and an interaction time of 0.0235 s, finite element analysis shows that rectangular beam (RB) produces a more uniform thermal gradient profile than circular beam (CB). RB has a

maximum thermal gradient of 4.94×10^6 K/m, 10% lower than CB. In addition, the highest thermal gradient position of RB is farther away from the beam center than CB. The differences in thermal gradients affect surface tension gradient, a controlling factor for the formation of cross flow in a molten pool [23]. Cross flow plays a decisive role in the uniformity of alloy distribution and surface roughness. Steep thermal gradient variations result in severe cross flow, and possibly rough surfaces. Depositions of TiC powder using rectangular beam produced layers with surface roughness (Ra) value less than $20 \mu\text{m}$, while using circular beam did not produce acceptable surface roughness.

4.4.3 Cooling rate

Normally, cooling rate is related to thermal gradient and beam velocity given by $R = |V \times G|$. Variations of cooling rate along the beam-moving direction follow the same trend as shown by surface thermal gradients. The cooling rate is computed in the order of 10^4 K/s (corresponding to a laser power 500 W and a scanning speed, 8.5 mm/s), which is similar to the results from a point source analytical model [24]. This cooling rate is very high in comparison to those obtainable in conventional material processing, however, it is somewhat lower than laser glazing and alloying.

4.4.4 Solidification microstructures

For a given composition, the formation of specific microstructure depends mainly on solidification parameters such as thermal gradient ($G = \frac{dT}{dx}$), cooling rate ($R_c = \frac{dT}{dt}$), solidification-front moving velocity, and the degree of undercooling [25]. SEM micrographs

(Figure 4.5) show a variety of dendrite structures, typical of the high cooling rate and larger undercoolings. In the H13 layer, the average secondary dendrite arm spacing, λ_2 , is 2.5 μm , and the cooling rate can be estimated as $2.5 \times 10^4 \text{ K/s}$ ($\dot{T} = \frac{1}{\lambda_2^3} (3.87 \times 10^{-13})$) [26], which is very close to the cooling rate obtained from simulation. Columnar dendrites, segmented by the interfaces of individual deposition layer and aligned in the direction of maximum thermal gradients, are observed in H13 and Ni/Cr alloy layers. This could be explained by the epitaxial growth of the layer on the substrate where the grains are favorably situated as well as steeper temperature gradients are provided by the laser parameters. In contrast, equiaxed dendritic structures were observed in TiC layers. Here, new dendrites form and grow in the mushy zone with random orientation. The equiaxed dendrites arise from a heterogeneous nucleation mechanism in which Ni/Cr layer diffuses to provide sites for nucleation. Additionally, the reduced thermal gradients and high growth rates made possible by the laser parameters reduced the G/R ratio, resulting in equiaxed dendrites.

Formation of these microstructures is favorable to the expected mechanical properties. The segmented columnar microstructures observed in both H13 and Ni/Cr layers could increase strain tolerance [27], yielding improved ability to resist thermal shock and spallation caused by cyclic thermal loadings in service. The equiaxed layer of TiC produced by LBFF would likely exhibit reduced thermal conductivity [28], which is beneficial to reduce oxidation of the underlying H13.

Final grain sizes depend, to a large extent, on the rate of cooling and have a direct effect on the mechanical properties [29]. The maximum grain dimension of all regions was measured

less than 25 μm . However, those grains in the regions closer to surface were much smaller. Re-heating of the preceding layers during layer processing caused the growth of grains in zones away from the surface.

Figure 4.6 displays sharp interfaces among distinct layers. Defects were not identified at the interfacial zones. H13 layer was “interlocked” with Ni/Cr layer possibly due to the disturbance of the moving substrate to the slowly solidifying molten pool, which was because of the high density (150 J/mm^2) and the thick deposition layer (0.13 mm) used, while no “interlock” occurrence was observed at the interface between Ni/Cr layer and TiC layer, because of the quick solidification resulting from low energy density (33 J/mm^2) and a thin deposition layer (0.008 mm). Elemental analysis of energy by the energy dispersive spectrum (EDS) shows that more than two-third of TiC layer was diluted by Ni/Cr powder. Furthermore, it did not show any abrupt change in the constituents across those interfaces (Figure 4.7). The observation was in agreement with the definition of functionally graded materials.

Figure 4.8 shows the Vickers microhardness variation with the distance from outside to inside surface. The data scatter was $\pm 4\%$. Compared to the hardness of heat-treated H13 steel, the hardness in the H13 layer of this functionally graded die insert was 15% higher, a direct benefit of rapid solidification resulting in fine structures.

4.4.5 Performance evaluation

High resistance to thermal fatigue, strain deformation, and oxidization at elevated temperature are desired properties for tooling as dies and molds. To examine the performance of dies and molds in a thermal fatigue environment, low cycle thermal fatigue tests were carried out on both machined molds of H13 steel and functionally graded mold (FGM) from LBFF. Results showed that, at the same conditions, machined H13 mold inserts did not have any cracks till onset of deformation due to alternating thermal loads, while the FGM had initiated cracks in the TiC layer around the 15th cycle. The occurrence of crack in TiC layer indicated the existence of residual stresses. In terms of resistance to deformation and oxidization at elevated temperatures, FGM displayed reduced scale formation (weight loss) and improved dimensional stability than the machined H13 molds, which is in consistence with our previous experiment results [21]. The enhanced ability to withhold oxidization and thermal stain deformation is attributed to the additional benefits of the fabrication process, and the peculiar arrangement of the material matrix.

4.5 Conclusions

- (1) A square die insert of functionally graded compositions of H13, Ni/Cr alloy and TiC was designed and fabricated using shaped beam profiles with LBFF. Characterizations showed full density of the insert, and gradual change of the composition in the transitional regions between distinct layers.
- (2) Surface thermal gradients of circular beam and rectangular beam were modeled using ANSYS and compared. The cooling rates were estimated and correlated with secondary dendrite arm spacing.

- (3) Maximal grain size was found to be approximately 25 μm . The coarse grains were resulted from repeated heating by the layer addition process.
- (4) Microhardness of FGM, on average, was higher than that of conventional H13 steel. Performance evaluation in a low-cycle thermal fatigue environment demonstrated improved strain tolerance, and resistance to oxidization at elevated temperature for FGM, but a better resistance to crack initiation for H13 mold due to alternating thermal loading.

Acknowledgements

Thanks are due to Mr. Larry Couture, Mechanical Engineering department, for his assistance in grinding the die insert; Dr. W. Wang and Mr. Y. Tian, Materials Science and Engineering department, for their help in sample preparation.

References

1. Hull, C., Feygin, M., Baron, Y., Sanders, R., Sachs, E., Lightman, A. and Wohlers, T. (1995). Rapid Prototyping: Current Technology and Future Potential. *Rapid Prototyping Journal*, Vol. 1, No. 1, pp. 11-19.
2. Hopkinson, N. and Dickens, P. (2001). Rapid Prototyping for Direct Manufacture. *Rapid Prototyping Journal*, Vol. 7, No. 4, pp. 197-202.
3. King, D. and Tansey, T. (2003). Rapid Tooling: Selective Laser Sintering Injection Tooling. *Journal of Materials Processing Technology*, Vol. 132, pp. 42-48.

4. Simchi, A., Petzoldt, F. and Pohl, H. (2003). On the Development of Direct Metal Laser Sintering for Rapid Tooling. *Journal of Materials Processing Technology*, Vol. 141, pp. 319-328.
5. Vilar, R. (2001). Laser Cladding. *The International Journal of Powder Metallurgy*, Vol. 37, No. 2, pp. 31-47.
6. Kruth, G. B. (1991). Material Ingress Manufacturing by Rapid Prototype Techniques. *Manufacturing Technology, Annals of the CIRP*, Vol. 40, No. 2, pp. 603-614.
7. Gerken, J., Haferkamp, H. and Schmidt, H. (1994). Rapid Prototyping/Manufacturing of Metal Components by Laser Cladding. *Proceedings of the 27th ISATA on Rapid Prototyping and Laser Applications for Automotive Industries*, Aachen, Germany, October 31-November 4, pp. 85-90.
8. Peng, S. C., Chou, C. J. and Jeng, J. Y. (1994). Application of Selective Laser Cladding in Rapid Prototype. *Proceedings of the 27th ISATA on Rapid Prototyping and Laser Applications for Automotive Industries*, Aachen, Germany, October 31-November 4, pp. 273-279.
9. Milewski, J. O., Lewis, G. K., Fonseca, J. C. and Nemeč, R. B. (2000). Laser Powder Deposition of a Near Net Shape Injection Mold Core-A Case Study. *Materials and Manufacturing Processes*, Vol. 15, No. 2, pp. 247-258.
10. Milewski, J. O., Dickerson, P. G., Nemeč, R. B., Lewis, G. K. and Fonseca, J. C. (1999). Application of a Manufacturing Model for the Optimization of Additive Processing of Inconel Alloy 90. *Journal of Materials Processing Technology*, Vol. 91, No. 1, pp. 18-28.

11. Mazumder, J., Choi, J., Nagarathnam, K., Koch, J. and Hetzner, D. (1997). The Direct Metal Deposition of H13 Tool Steel for 3-D Components. *Journal of Metals*, May, pp. 55-60.
12. Keicher, D. M. and Miller, W. D. (1998). LENSTM moves beyond RP to Direct Fabrication. *Metal Powder Report*, Vol. 53, No. 12, pp. 26-28.
13. Link, G. R., Fessler, J., Nickel, A. and Prinz, F. (1998). Rapid Tooling Die Cast Inserts Using Shape Deposition Manufacturing. *Materials and Manufacturing Processes*, Vol. 13, No. 2, pp. 263-274.
14. Irving, R. (1999). Taking a Powder. *Mechanical Engineering*, September, pp.55-59.
15. Kathuria, Y. P. (2000). Some Aspects of Laser Surface Cladding in the Turbine Industry. *Surface and Coatings Technology*, Vol. 132, pp. 262-269.
16. Kobryn, P. A, Moore, E. H. and Semiatin, S. L. (2000). The Effect of Laser Power and Traverse Speed on Microstructure, Porosity, and Build Height in Laser-Deposited Ti-6Al-4V. *Scripta Materialia*, Vol. 43, pp. 299-305.
17. Vasinonta, A., Beuth, J. L. and Griffith, M. L. (2001). A Process Map for Consistent Build Conditions in the Solid Freeform Fabrication of Thin-Walled Structures. *Journal of Manufacturing Science and Engineering*, Vol. 123, pp. 615-622.
18. Kaplan, A. F. H., and Groboth, G. (2001). Process Analysis of Laser Beam Cladding. *Journal of Manufacturing Science and Engineering*, Vol. 123, pp. 609-614.

19. Jiang, W., Stock, M. and Molian, P. A. (2002). Production of Aluminum Extrusion Dies Using a Laser-Based Flexible Fabrication Technique. *Transactions of SME/NAMRC XXX*, pp. 17-24.
20. Mattox, M. (1994). Growth and Growth-Related Properties of Thin Films Formed by Physical Vapor Deposition. *ASM Metal Handbook, Vol. 5*, ASM International, Metals Park, OH, 1994, pp. 538-555.
21. Jiang, W. and Molian, P. A. (2002). Laser-Based Flexible Fabrication of Functionally Graded Mold Inserts. *The International Journal of Advanced Manufacturing Technology*, Vol. 19, pp. 646-654.
22. <http://www.sz-metal.si/products/steels/UTOPMO2.htm>, Date accessed: April 2, 2002.
23. Mazumder, J. and Chande, T. (1985). Two Dimensional, Transient Model for Mass Transport in Laser Surface Alloying. *Journal of Applied Physics*, Vol. 57, No. 6, pp. 2226-2232.
24. Jiang, W. (2002). Experimental and Analytical Studies of a CO₂ Laser-Based Flexible Fabrication Method for Dies and Molds. *PhD dissertation*, Iowa State University, Ames, Iowa.
25. Simchi, A., Petzoldt, F. and Pohl, H. (2001). Direct Metal Laser Sintering: Material Considerations and Mechanisms of Particle Bonding. *The International Journal of Powder Metallurgy*, Vol. 37, No. 2, pp. 49-60.

26. Mazumder, J., Schifferer, A. and Choi, J. (1999). Direct Materials Deposition: Designed Macro and Microstructure. *Symposium Proceedings of Material Research Society*, Vol. 542, pp. 51-63.
27. Steffens, H. D., Bablak, Z. and Brandl, W. (1991). Thermal Barrier Coatings: Some Aspect of Properties Design. *Proceedings of Fourth National Spray Conference*, ASM International, Material Park, OH, pp. 289-294.
28. An, K., Ravichandran, K. S., Dutton, R. E. and Semiatin, S. L. (1999). Microstructure, Texture, and Thermal Conductivity of Single-Layer and Multilayer Thermal Barrier Coatings of Y_2O_3 -Stablized ZrO_2 and Al_2O_3 Made by Physical Vapor Deposition. *Journal of the American Ceramic Society*, Vol. 82, No. 2, pp. 399-406.
29. Hurst, S. (1996). *Metal Casting*. Intermediate Technology Publications, London.

List of Figures

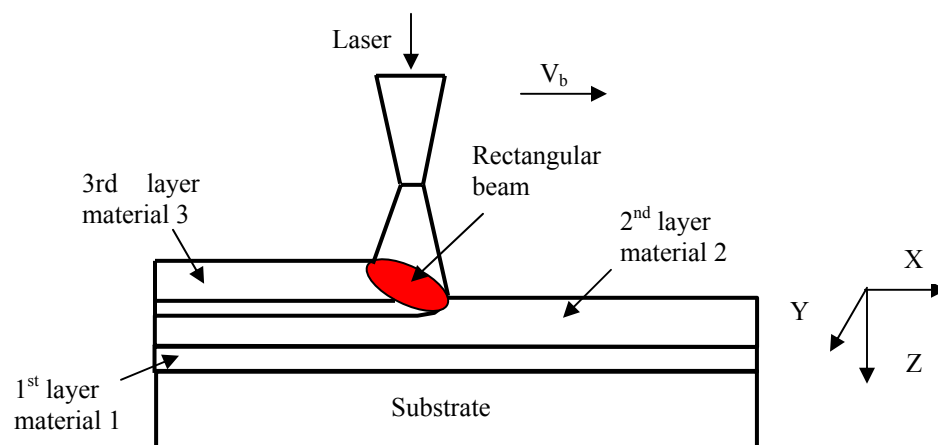
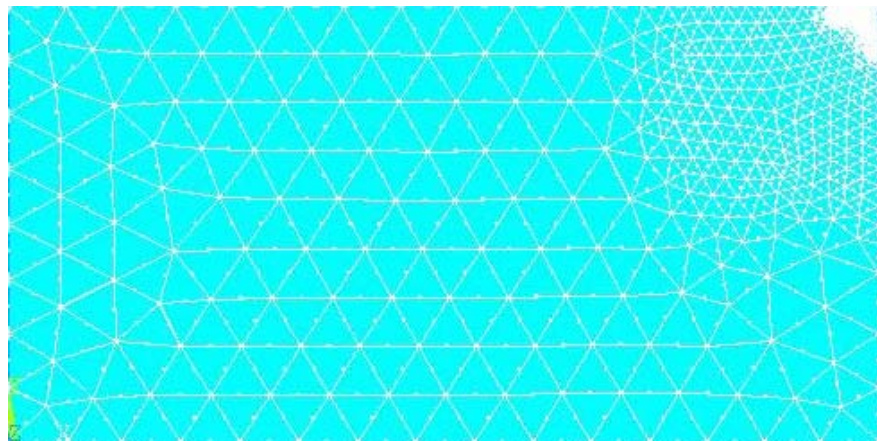
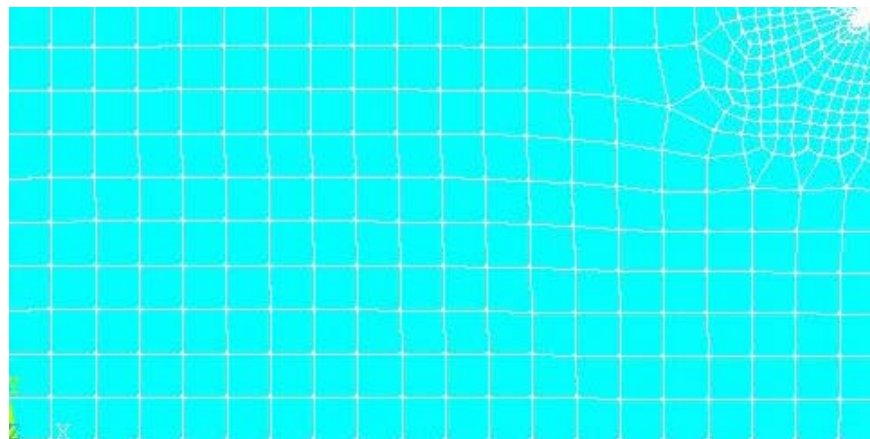


Figure 4.1 Schematic showing the LBFF process.



(A)



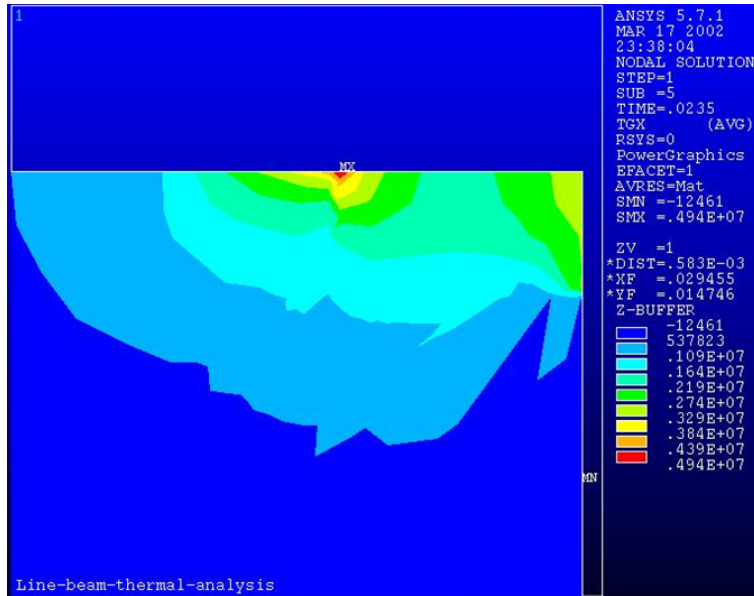
(B)

Figure 4.2 The meshes used for surface thermal gradient computations for: (A) circular beam (CB), and (B) rectangular beam (RB).

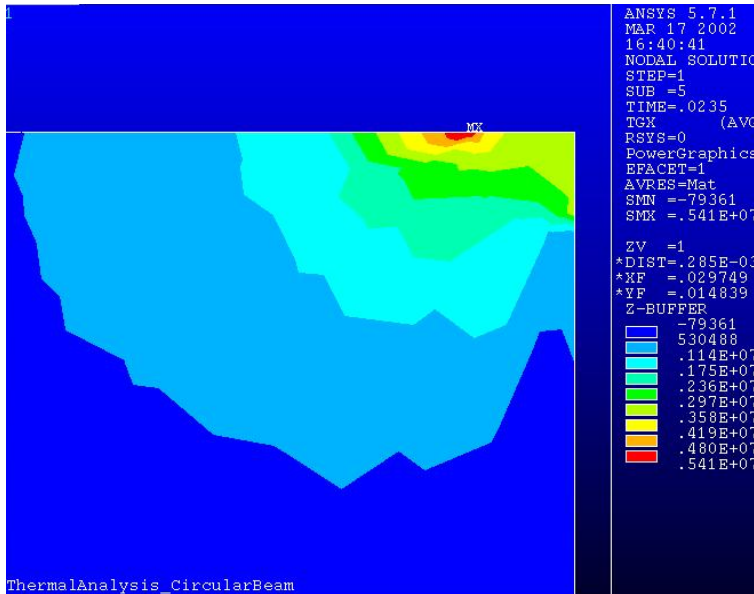


10 mm

Figure 4.3 Photo illustrating a square functionally graded mold insert fabricated using LBFF.

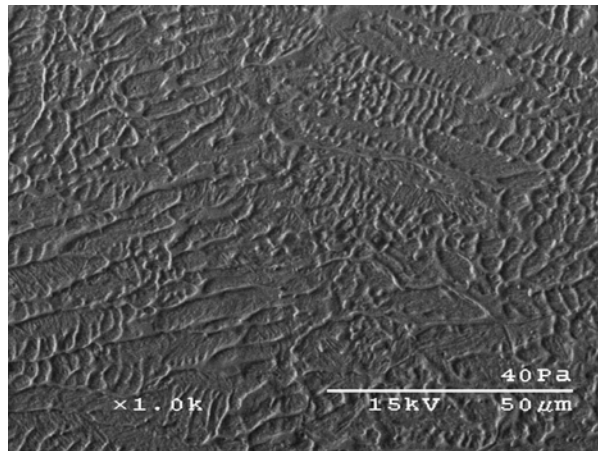


(A)

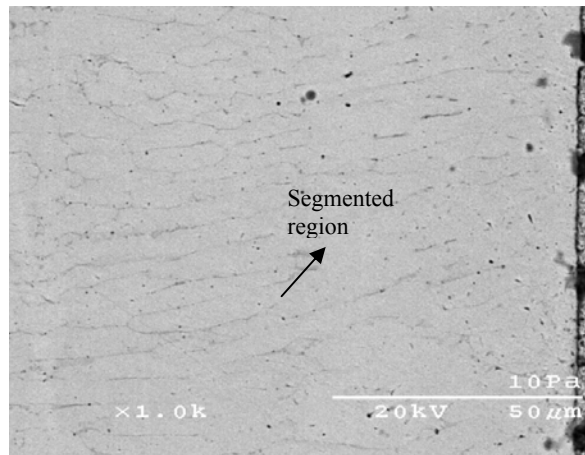


(B)

Figure 4.4 Surface thermal gradient profile of: (A) rectangular beam (RB), and (B) circular beam (CB) (laser power: 500 W; and interaction time: 0.0235 s).



(A)

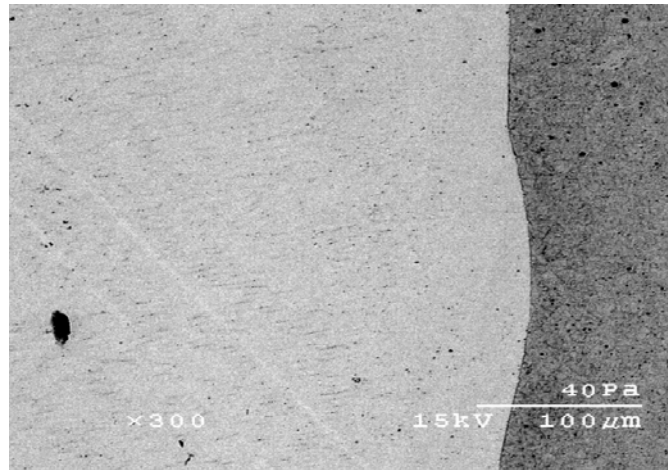


(B)

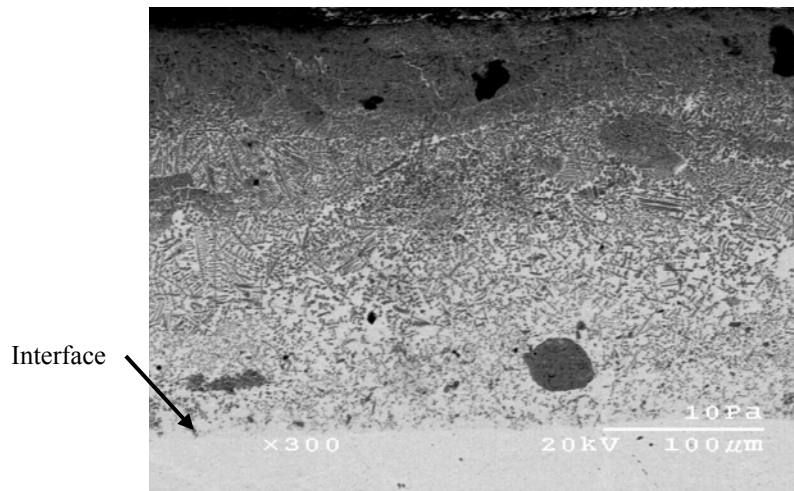


(C)

Figure 4.5 Typical microstructures in: (A) H13 layer, (B) Ni/Cr alloy layer, and (C) TiC layer.



(A)



(B)

Figure 4.6 SEM showing the interfaces of: (A) H13 and Ni/Cr alloy, and (B) TiC and Ni/Cr alloy.

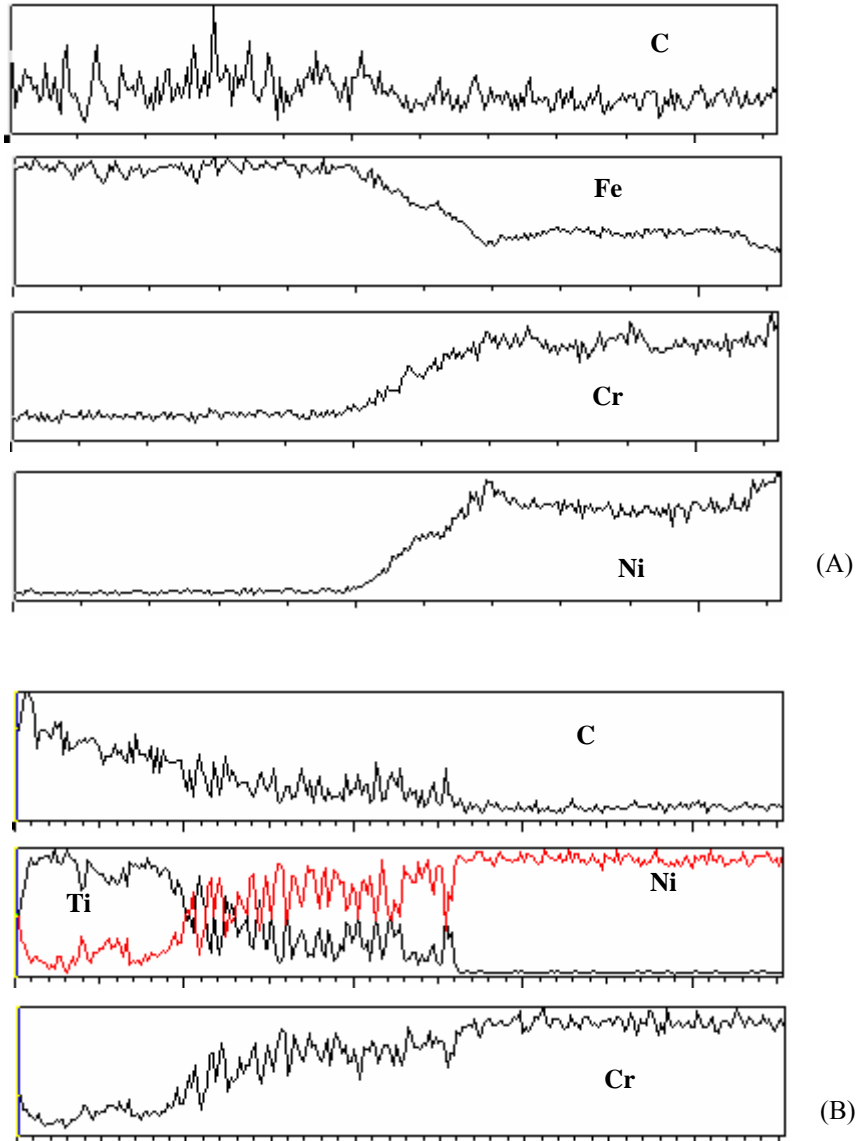


Figure 4.7 SEM of compositional distribution of the FGM interface of: (A) H13 and Ni/Cr alloy, and (B) TiC and Ni/Cr alloy.

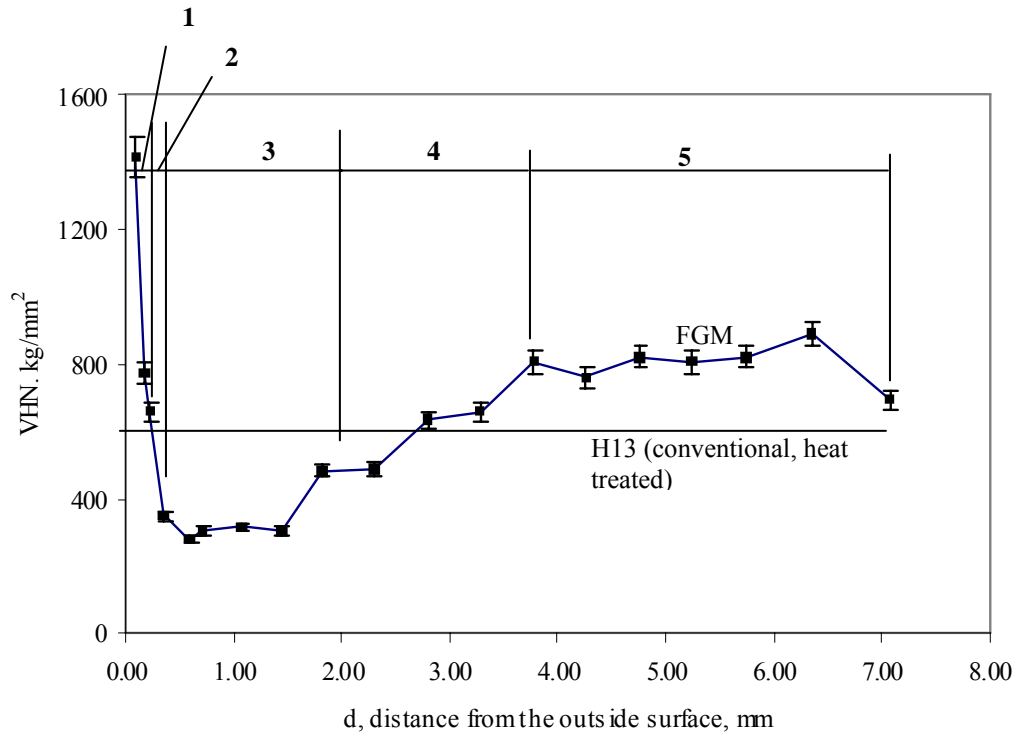


Figure 4.8 Vickers microhardness (1.0 kgf) profile along the mold insert wall thickness starting from outside (1: TiC; 2: interface; 3: Ni-Cr alloy; 4: interface; 5: H-13).

List of Tables

Table 4.1 Density, specific heat, and thermal conductivity of H13 steel [22].

Temperature (K)	293	773	873
Density (kg/m ³)	7800	7640	7600
Specific heat (J/kg.K)	460	550	590
Thermal conductivity (W/m.K)	25.0	28.5	29.3

Table 4.2 Load Settings of ANSYS for surface thermal gradient computation.

Heat flux (W/m ²)	3.75×10^8
Interaction time (sec)	0.0235
Time at the end of load step (sec)	0.0235
Time step size (sec)	0.00235
Initial temperatures (K)	293
Automatic time stepping	ON
Use previous size	YES

CHAPTER 5. Preparation and Characterization of Diamond-like Carbon Coating on Aluminum 6061 T-91 Substrate using Laser Sintering

Paper submitted to *Surface Coatings and Technology*, 2007

Rajeev Nair, Wenping Jiang and Pal Molian

Abstract

Diamond-like carbon (DLC) coatings have been prepared on aluminum 6061 T-91 substrates with the aid of electrostatic spray coating of synthetic nanocrystalline diamond powders followed by direct laser sintering technique. A continuous wave CO₂ laser was utilized, producing a dense coating with an average thickness of 10 μm. The optimal laser parameters were, power of 200 W, spot size of 1mm by 0.1 mm, and speed of 254 mm/s. The evidence of DLC formation and its purity was obtained by characterizing the samples with energy dispersive spectroscopy, Raman spectroscopy, X-ray diffraction and scanning electron microscopy. Functional evaluation of DLC coating was performed using scratch, micro-hardness, fracture toughness and surface roughness tests.

Raman measurements showed the presence of a broader peak at around 1332 cm⁻¹ (characteristic of pure diamond) for samples which were electrostatically coated with diamond nanopowders while the samples which were laser-processed at a higher scan rate showed the presence of DLC with a broad asymmetric hump in the region from 1000 to 1600 cm⁻¹. Energy dispersive spectroscopy and X-ray diffraction confirmed the presence of carbon phases in the processed samples. Scanning electron microscopy showed a 60-80 μm heat-affected-zone between the aluminum sample substrate and the coating, leading us to believe

that the diamond may have diffused into aluminum at the interface to form nano-composite diamond-like carbon-aluminum, while the surface revealed a fairly uniform and dense coating. These coatings exhibited micro-hardness in the range of 2150 to 2350 kg/mm² when measured using a Vickers diamond pyramid indenter. In some localized regions, hardness of 9000 kg/mm² were obtained. Scratch tests revealed a fairly homogenous coating with strong adhesive nature having almost four times the average critical force (L_c) when compared to the electrostatic spray coated sample. Fracture toughness and surface roughness are within acceptable ranges of DLC coatings. Sample characterization showed a strong bond between the substrate and the DLC layer. Coating of aluminum with the outstanding chemical and tribological resistant DLC layer offers the possibility to tailor an extreme lightweight, strong and wear-resistant material.

5.1 Introduction

Nanoparticles are essential building blocks for manufacturing of nano-structured porous and dense coatings, which have unique properties such as ultrahigh hardness, thermal conductivity, strength, and wear resistance. Nanostructured coatings have significant potential applications in wear resistance with enhanced hardness and toughness [1]. However, these coatings are prone to the formation of agglomerates and tend to stick to the surfaces in physical contact during the deposition process. Electrostatic spray coating can avoid particle agglomeration for coating sub-micron and nano-sized particles especially on flat geometries. Laser sintering of electrostatic sprayed nanoparticles is a better technique because the traditional laser sintering using powder delivery method does not allow smooth flow of nanoscale powders through the pipes due to high drag forces [2].

Introduction of a protective layer(s) on a metal substrate is an efficient means of minimizing wear and premature failure because it imparts the desired mechanical (increased wear, erosion, and heat checking resistance) and thermal properties (heat insulation) with much reduced cost [3]. Diamond-like carbon (DLC) is an amorphous (hydrogenated or non-hydrogenated), meta-stable carbon. The extraordinary properties of the DLC explain the ardent interest shown in the development of these coatings in recent years. DLC has established as wear resistant coating on cutting tools, heat dissipation in hybrid integrated circuits, wear-resistant and anti-sticking overcoat for computer disks and wear and corrosion-resistant biocompatible coating for surgical prostheses. Formation of hard, lubricious coatings of DLC on structural substrates results in the substantial improvement of the overall performance of an automobile especially in power train components and piston-bore assembly. Diamond-like carbon coatings fall into the category of high quality surface coatings and have excellent tribological properties [4, 5]. DLC coatings on aluminum alloys are particularly attractive in high vacuum environment such as in outer space, due to chemical inertness, high hardness, thermal conductivity and elastic modulus, low friction coefficient and low wear rate [6-8].

The tribological property profile of a coated-material depends on both the coating and the substrate. Therefore, when discussing tribological properties, one has to take into account not only the behavior of the coating, but also the property profile and suitability of the substrate as well. Low specific gravity and high strength-to-weight ratio make aluminum and its alloys extensively used in many industries, especially in aviation and space industry. DLC coatings are emerging as successful tribological coatings for aluminum alloys. However

these coatings are prepared by techniques such as chemical vapor deposition (CVD) and physical vapor deposition (PVD) which are quite cumbersome.

Nanocrystalline diamond powders were sprayed by electrostatic forces and then laser-sintered on aluminum 6061 T-91 substrates to form DLC coatings with a strong substrate-coating interface unlike other processes like PVD. Laser sintering is a manufacturing technique which uses a laser beam to sinter material powder in several scans to produce three-dimensional parts directly from a computer aided design model (CAD) [9-12]. It can also be used to form a coating on substrate in a single scan. There are four most widely used forms of laser sintering: a) Direct solid-state sintering, b) Direct liquid-phase sintering, c) Indirect solid-polymer sintering, and d) Indirect solid-solid sintering. In direct solid-state sintering, the laser energy is applied to induce a temperature close to the melting temperature so that binding occurs at the interfacial grain contacts [13]. In direct liquid-phase sintering, owing to higher viscosity and surface tension effects, the molten metal tends to form a spherical, ball-type structure, which is basically a coalescence of several nanoparticles [14]. In the case of indirect solid-polymer sintering, the polymer by virtue of its low viscosity acts as a binder and prevents the balling effects as in liquid-phase sintering [15, 16]. Finally, the indirect solid-solid sintering method consists of a mixture of two metal powders comprising a high-melting-point metal and a low-melting-point metal, the latter serving as a binder. In this case, the laser energy should be high enough to raise the powder temperature between the melting points of the two metals to make the binder metal melt and flow by driving forces such as the liquid pressure, viscosity and capillary forces through the pores between the solid particles [17].

5.2 Experimental Procedure

5.2.1 Aluminum substrate

In this work, aluminum 6061-T91 metal substrates are used which have good acceptance of coatings [18, 19]. This grade of aluminum is used for a wide variety of products and applications especially where strength, weldability and corrosion resistance are needed. The heat treatment processes from the wrought aluminum 6061 to transforming it into aluminum 6061 T-91 involves three major steps: The first step is solution heat treatment where the alloy is soaked at 530 °C for a time, long enough to achieve a nearly homogenous solid solution; The second step is to quench the solid solution formed, rapidly enough (and without interruption) to produce a supersaturated solution at room temperature. The final part of heat treatment is precipitation heat treatment where precipitation of solute atoms is done at elevated temperature (160 °C) for 18 hours. Cold working subsequent to precipitation heat treatment is necessary to attain the specified properties for this temper [20]. The following table shows the percentage composition of various elements in aluminum 6061 T-91 used in this work.

Table 5.1 Composition of various elements in Aluminum 6061-T91 [18].

Component	Wt. %	Component	Wt. %	Component	Wt. %
Al	98	Fe	Max 0.7	Si	0.4-0.8
Cr	0.04-0.35	Mg	0.8-1.2	Ti	Max 0.15
Cu	0.15-0.4	Mn	Max 0.15	Zn	Max 0.25

5.2.2 Preparation of Nano-diamond Powders

Diamond powder production and purification is an expensive process. The diamond nanopowders used for this experiment was acquired from Ames Laboratory (Dr. Anatoli

Frishman, Dept. of Physics, Iowa State University) and its production is based on explosion, also called as shock detonation synthesis [21]. This process is based on the effect of ultra-fine diamond nanopowder formation through the detonation wave of some special explosives like Trinitrotoluene (TNT) and Cyclotrimethylene Trinitramine also known as RDX. The nanopowders contained 2% impurities consisting of Ca, Fe, Cu, Al, Cr and Si. Transmission electron microscopy (TEM) micrographs of the acquired diamond nanopowders demonstrate the uniformity of the particles and a particle size range between 4 to 8 nanometers. The electron diffraction rings in the upper right hand corner in part A of Figure 5.1 is a characteristic of nanophase structure. Part B of the figure shows the rounded nature of the grains obtained through the detonation synthesis. Table 5.2 provides the characteristics of nano-diamond powders acquired. It has been found that nanocrystalline diamond is more stable with respect to graphitization than usual diamonds at high temperature and ambient pressure [22]. Direct laser sintering is non-equilibrium high temperature process at ambient pressure and the acquired diamond nanopowders is believed to be excellent towards the creation of a uniform layer of DLC. The wetted and bonded DLC coating is expected to provide properties superior to the often used micro-sized granulate coatings.

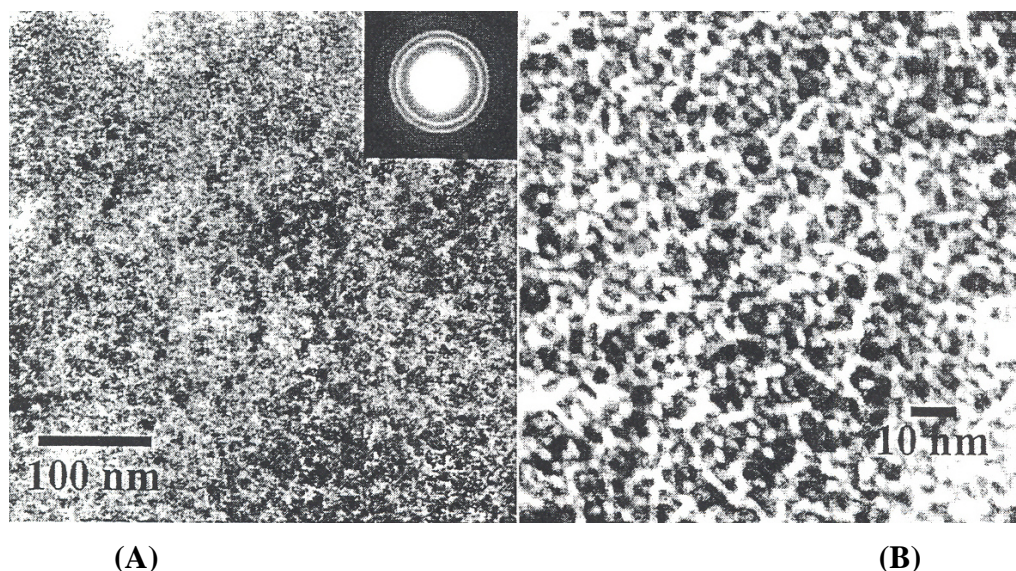


Figure 5.1 TEM micrographs of the as-received diamond powder, A) Lower magnification with a selected area diffraction pattern in the upper right hand corner, B) High magnification micrograph showing the rounded nature of the grains.

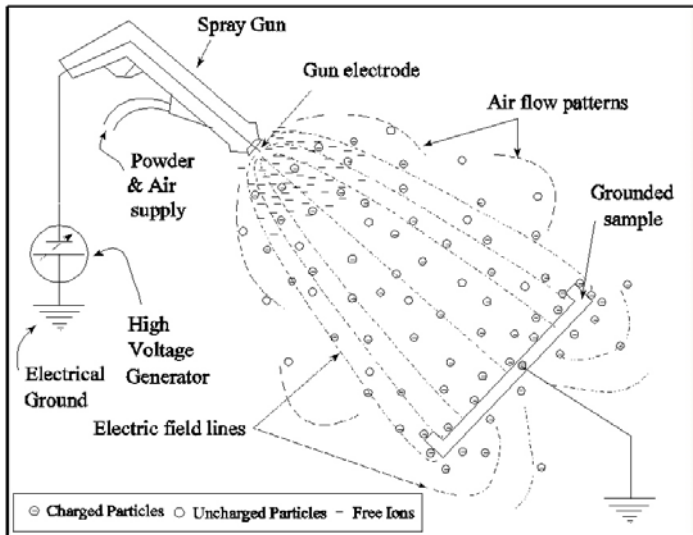
Table 5.2 Basic technical characteristics of the diamond nanopowder.

External kind	Powder of gray color
Moisture quantity, % not more	0.5
Average size of prime particles (coherent scattering region), nm	2-8
Specific surface, m ² /g	250
Pouring density, g/cm ³	3.0
Quantity of metallic impurities, % not more	2.0
Quantity of carbon cubic phase, % not less	90
Quantity of impurity additives, % not more	2.0

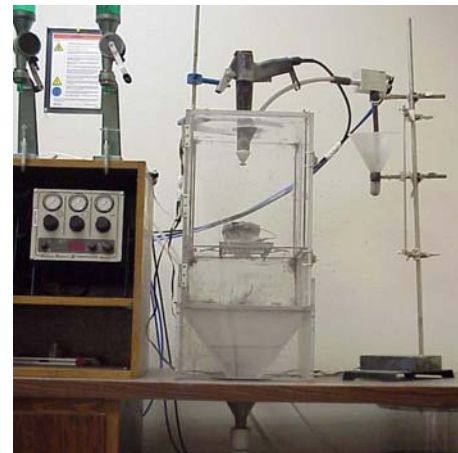
5.2.3 Electrostatic Spray Coating (ESC) Process

Electrostatic spray coating is a widely used method in paint technology; however, it was relatively unexplored in ceramic and metal coating industry. In ESC process, the powder particles are generally electrically insulating in nature and can carry the static charge over a distance of a few tens of centimeters. The powder particles are charged when they come out of the powder spray gun and exposed to an electrostatic field generated by a pointed

electrode, which is subjected to, typically a few tens of kilovolts. The charged powder particles follow the electric field lines toward the grounded objects (substrates) and form a uniform coating preform (Figure 5.2).



(A)



(B)

Figure 5.2 (A) Schematic of the ESC Process [2], (B) Electrostatic spray coater.

In general, powder particles with particle size in the range of a few tenths of a micron have extremely high surface energy and thus, in the dispersion process they tend to clump with each other to minimize the surface energy. The cluster of the particles with reduced sizes significantly increases the difficulty for conventional powder delivery and deposition process. However, in the electrostatic process, particles are charged with similar polarity and will have little chances to form cluster, thus a uniform coating could be obtained covering the entire grounded sample surface. Since the charged powder particles follow the field lines emanating from the entire surface of the grounded objects, the spray coating is formed all

over the object surface, which is a significant advantage for coating complex geometry surfaces. An electrostatic powder deposition system helps in reducing space requirement, achieving a more packed bed and enabling powder storage in a different location other than the workspace [23].

Al-6061 T-91 metal coupons (of sizes 25.4 mm by 25.4 mm by 9.5 mm) were sand blasted and electro-statically deposited with synthetic diamond nanopowders of size range 4 to 8 nm (2% impure). The deposition process was carefully controlled so as to get a uniform and homogenous coating. The thickness of the deposited nano-diamond powder coating was in the range of 20 to 30 μm .

5.2.4 Laser Sintering Process

Laser sintering is a rapid process developed for making thick single-layer coatings on metal samples pre-coated with powders using electrostatic deposition process (Figure 5.3). Laser sintering of nanoparticles is probably a better approach than furnace sintering to retain the grain sizes in the nanometer range. Furnace sintering leads to a coarsening tendency, particle agglomeration, inherent contamination, and ultimate loss of nano-features. Molecular dynamics simulations showed that sintering of nanoparticles proceeds extremely fast, which can be explained by sintering mechanisms such as dislocation motion, particle rotation and viscous flow in addition to surface and volume diffusion [1]. Consequently, laser-sintering would be preferred to match the speed at which nano-sintering takes place. The laser power required for sintering nanoparticles is much lower because nanoparticles can readily absorb laser light due to their large surface areas, and kinetics of sintering indicate the onset of

sintering temperature as $0.2-0.3 T_m$ (melting point) as compared to $0.5-0.8 T_m$ for microscale powders [1]. Consequently laser-sintering is expected to form a homogeneous and dense layer while furnace sintering will produce layers consisting of agglomerates and inter-agglomerate pores.

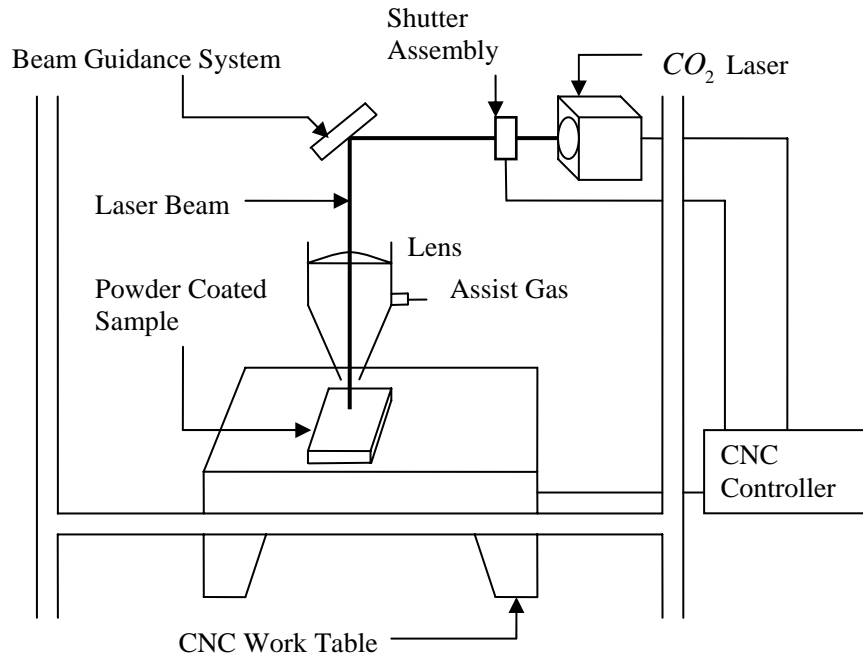


Figure 5.3 Schematic of the direct laser-sintering process.

In this work, we use the direct solid-state laser sintering approach to bond the nanoparticles and the substrate. Direct-solid state sintering offers the benefit of sound bonding, which is important for functional coatings. A factor that can have great impact on the stabilization of nanoparticles is the shape of the laser beam. A defocused Gaussian beam is almost always used for sintering. If the beam is stretched in the direction of sintering, a smooth, flat type of layer can be obtained because of reduced temperature gradient. In addition, the coupling between the beam and material can be made more efficient due to the preheating of the

powder at the leading edge of the beam, making more energy available for heating the powder. Furthermore, switching the circular beam to a high-aspect-ratio rectangular beam (RB) significantly reduces heat conduction losses. Consequently, the shaped beam facilitates even sintering, leading to improved surfaces.

A 1500 W continuous wave CO₂ laser (*820 Spectra – Spectra Physics*[®]) was used for the laser-sintering process. A focused RB (with a focal length: leading edge of 1 mm by a width of 0.1 mm) was chosen for the process which gave a laser spot area on the surface of 0.1 mm². The laser beam motion controlled by a programmed CNC controller, was used to scan the work piece in straight lines across the workpiece with the distance between the scans being 0.254 mm. Argon was used as the assist gas during the sintering process. The range of process parameters used for the laser-sintering process is shown in Table 5.3.

Table 5.3 Process Parameters for the Fabrication.

Parameter	Value
Laser power, Watt	100-300
Focal length of lens, mm	127
Spot area at the powder surface, mm ²	0.1
Scanning speed, mm/s	40-254
Standoff distance from the nozzle to the substrate, mm	15
Overlap among passes, %	15-25
Assist gas flow rate, m ³ /s(*10 ⁻⁴)	3.15

5.2.5 Measurements and Sample Characterization

Micro-hardness tests were conducted to determine the surface hardness of the laser-sintered samples followed fracture toughness evaluations. Surface roughness, R_a , of the scanned surface was measured using a surface profilometer with a diamond stylus of 0.025 mm in diameter. Scratch test (*Micro Photonics*[®] *MST*) was performed to determine the critical and frictional forces on the nano-diamond laser-sintered aluminum sample as well as the non-sintered diamond-coated aluminum sample. Metallographic samples of the molds were prepared, and then examined for flaws (porosity and cracks) and microstructure using scanning electron microscopy (*SEM, JEOL 840A, 10 kV*). X-ray diffraction was carried out on the sintered sample to confirm the presence of carbon phases using a *SIEMENS*[®] *D500* X-ray diffractometer. Raman spectroscopy measurements were conducted: on the pure diamond powder before coating, electro-statically deposited diamond powder on the aluminum samples, and the laser-processed coupons to examine sp^3 and sp^2 bonding (*Ramascope, Reinshaw*[®] *1000*).

5.3 Results

5.3.1 Effects of Laser Parameters

Line energy, that is, the ratio of laser power to scanning velocity, in the range 0.78 and 0.94 J/mm, has the most favorable effect on the laser-processed samples. Line energy below 0.78 J/mm did not show a noticeable change in the powder characteristics. Essentially the energy was not adequate for sintering. Above 0.94 J/mm, the electrostatically-deposited powders melted and vaporized, leaving a highly uneven, non-uniform and discontinuous coating. There were fairly uniform and thick coatings obtained in the range of 0.78 and 0.94 J/mm.

5.3.2 Micro-hardness

Micro-hardness experiments were taken as the benchmark to decide on the effectiveness of laser-sintering of the diamond nanopowders on the aluminum substrate. A Vickers micro-hardness indenter was used for the study with a load of 50 gf along the transverse section. A total of 4 measurements were made for each sample for different power and scan rate. The results show that lower laser scan rates produced coatings with very poor micro-hardness values when compared to those produced using higher rates for all power. The best results (Figure 5.4) were obtained for a laser power of 200 Watts and a laser scan rate of 254 mm per min. yielding an average micro-hardness value of 2250 kg/mm² (22.5 GPa). There were a few spots which produced hardness in the range of 9000 kg/mm² (200 W and 254 mm per second).

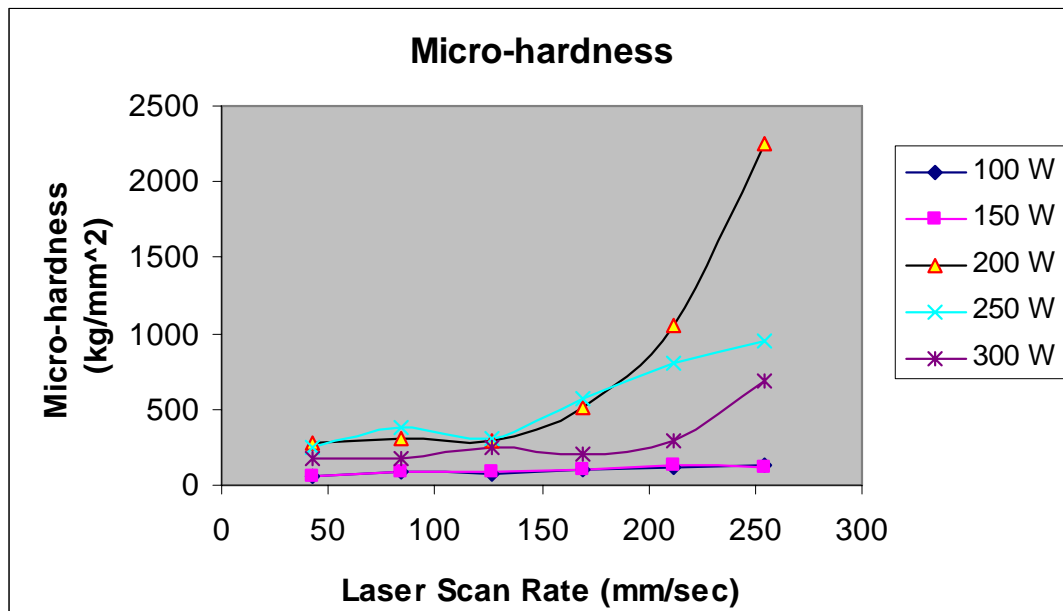


Figure 5.4 Micro-hardness of diamond sintered samples (Scatter $\pm 4\%$).

Vicker's microhardness test using 100 gf load was performed on the cross-section of DLC coated 6061 aluminum substrate. Figure 5.5 shows the optical micrograph with microhardness indentations. Figure 5.6 shows the hardness distributions in the heat affected zone (HAZ) and substrate. Only one hardness reading could be taken in the HAZ at one location because the diagonal of square indentation was about 55-60 μm , which is nearly 80% of the size of HAZ. The hardness depends on the precipitate distribution such as Mg_2Si . The hardness was lower in the HAZ (based on three locations) than the substrate because of re-resolution of precipitates and overaging effects that caused growth of precipitates.

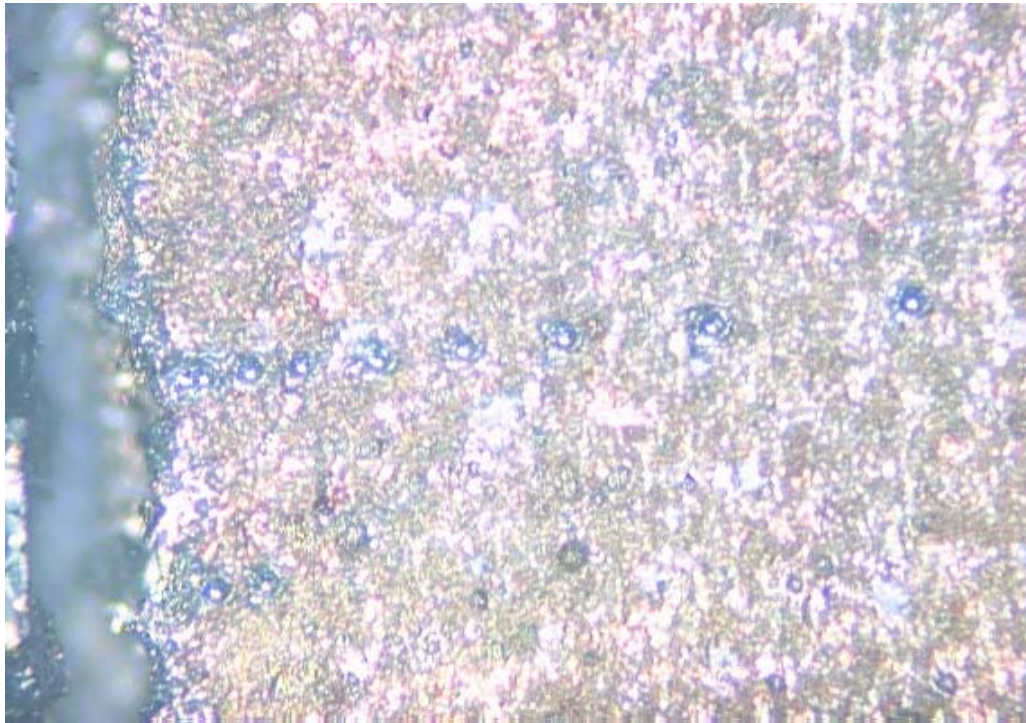


Figure 5.5 Optical micrograph of the substrate cross-section with microhardness indentations (coating at the left, substrate from left to right).

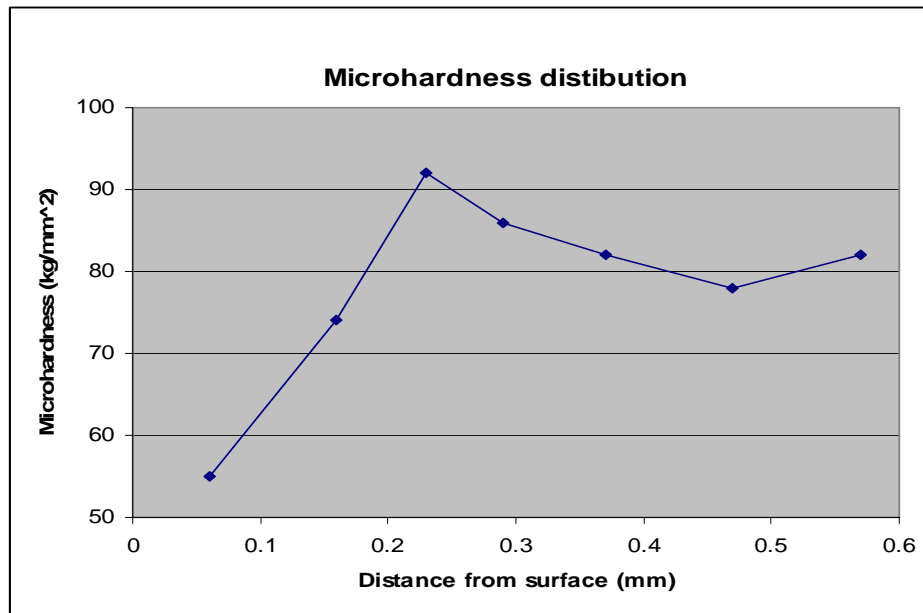


Figure 5.6 Vickers microhardness distribution across the cross-section

5.3.3 Fracture toughness

Since the optimal laser power was found to be 200 W and scan velocity 254 mm/s, it was decided to conduct fracture toughness tests on the sample sintered using those processing conditions. The fracture toughness K_{Ic} is a measure of the resistance of a crack to propagate in a material and may be determined by observing how a crack of known geometry extends as a function of applied stress [24]. The technique used here to find fracture toughness is based on the observation that brittle materials will normally fracture when indented with a certain critical load. Although this method is crude to ascertain fracture toughness, a general estimate can be found. The load depends on the material and type of indenter but typically for a Vickers indenter and brittle coatings (like ceramics and DLC), the critical load at which cracks will nucleate and propagate from the corners of the impression are above 0.25 N, depending on the thickness of the coating [25].

In this experiment a Vickers indenter was used to make indentations on the sintered sample (Figure 5.7), laser-treated at 200 W and 254 mm per second, which was found to have the maximum micro-hardness among all the samples. It has been shown in multiple derivations that length of the corner cracks can be related to the fracture toughness of a material by the formula [26],

$$K_C = \zeta \left(\frac{E}{H} \right)^{\frac{1}{2}} (P)(c)^{-\frac{3}{2}} \quad (1)$$

E = Young's Modulus of DLC = $3.4 * 10^5$ MPa, H = Hardness = 2250 Vickers hardness number = $2250 * 9.81 = 22072$ MPa, P = Load = 2 kgf = 19.62 N, c = Distance from the center of the indentation to the end of the crack = 105 μm , ζ = Constant taken as 0.016,

$$K_C = 1.15 \text{ MPa} \sqrt{m}$$

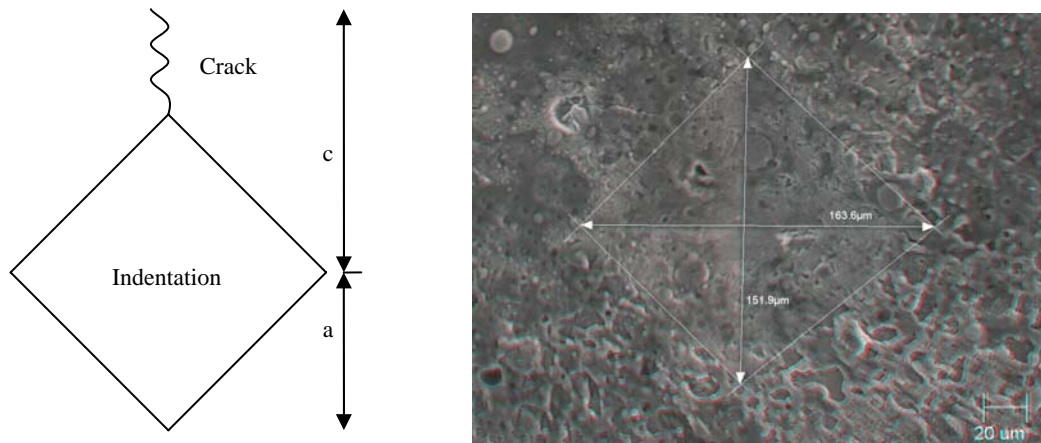


Figure 5.7 Indentation profile with a Vickers probe.

The fracture toughness obtained in this case, is in the range of 1 to 2.3 $\text{MPa} \sqrt{m}$, generally obtained for diamond-like carbon film coatings. Repetitive experiments (four tests) all

revealed the fracture toughness value to be in this range and showed the brittle nature of the coating.

5.3.4 Surface Roughness

The average surface roughness (R_a) of the 200 W laser-sintered sample was measured using a *Sheffield Measurement*[®] surface profilometer. The measurements were done perpendicular to the direction of the movement of the laser beam.

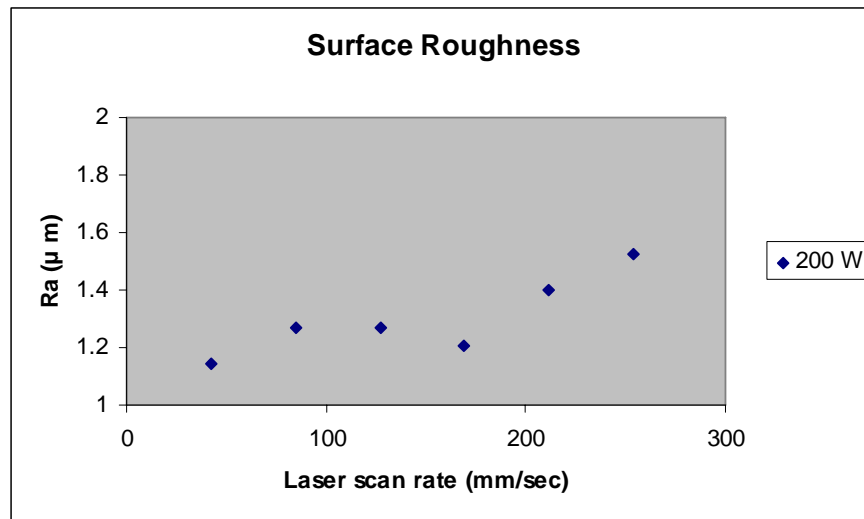


Figure 5.8 Average surface roughness of laser-processed samples (Scatter $\pm 3\%$).

The average surface roughness tends to increase with increased laser scan rate as seen in Figure 5.8. This has to do with the laser energy on the diamond-coated sample surface and the conversion into various carbon forms. It is believed that higher energy density may create different carbon phases like graphite that can give rise to low surface roughness which essentially is the case when the laser scan rate is lower. At lower laser scan rates, the energy

density is higher and the nano-diamond powders convert into full polycrystalline graphitic phases rendering it very smooth, giving a better surface finish.

5.3.5 Scratch test

The scratch-test method consists of the generation of scratches with a spherical stylus, generally Rockwell C diamond, tip radius 200 μm , which is drawn at a constant speed across the coating-substrate system to be tested, under either constant or progressive loading at a fixed rate. For progressive loading, the critical load (L_c) is defined as the smallest load at which a recognizable failure occurs; for the constant loading mode, the critical load corresponds to the load at which a regular occurrence of such failure along the track is observed. The driving forces for coating damage in the scratch test are a combination of elastic-plastic indentation stresses, frictional stresses and residual internal stresses. In the lower load regime, these stresses generally result in conformal or tensile cracking of the coating which still remains fully adherent. The onset of these phenomena defines a first critical load. In the higher load regime, one defines another critical load which corresponds to the onset of coating detachment from the substrate by spalling, buckling or chipping [27]. The scratch test is basically a comparison test. The critical loads depend, of course, on the mechanical strength (adhesion, cohesion) of a coating-substrate composite but also on several other parameters: some of them are directly related to the test itself, while others are related to the coating-substrate system.

There are different means for critical load determination. Microscopic observation is the most reliable method to detect coating damage. This technique is able to differentiate

between cohesive failure within the coating and adhesive failure at the interface of the coating-substrate system. Acoustic emission (AE) detection is the detection of elastic waves generated as a result of the formation and propagation of micro-cracks. The AE sensor is insensitive to mechanical vibration frequencies of the instrument. Tangential force (F_t) recording enables the force fluctuations along the scratch to be followed.

Table 5.4 Scratch test conditions and procedure.

Loading range	0 to 9 N
Loading rate, dL/dt	6 N/min
Scratch length	7.5 mm
Scratching speed, dx/dt	5 mm/min
Acoustic emission sensitivity, S_{AE}	9
Diamond indenter tip radius	200 μm

A laser-sintered sample (200 W, 254 mm per second) was chosen for the scratch test and was compared to an ‘as-coated’ sample under progressive loading of 6 N/min. An ‘as-coated’ sample refers to an aluminum sample which has been electrostatic spray coated (ESC) with synthetic nano-diamond powders. Average critical force (L_c) based on the sudden change of the acoustic emission signal for a laser-sintered sample (200 W, 254 mm per second) was found to be 4.51 N and that for an ‘as-coated’ sample 1.61 N. The critical load can be clearly seen to be almost 350 % more compared to an ‘as-coated’ sample for a long delamination. As the aluminum alloy substrate is soft that the deformation of the substrate occurs during the scratch test, the measured average critical force value of 4.51 N may not be the actual adhesion strength of the DLC coating, but, this is a good comparison test versus the ‘as-coated’ sample. A few optical micrographs of sintered and ‘as-coated’ samples during the start of the scratch test till the long delamination are shown below. In a recent study, PVD

(physical vapor deposition) coatings of Ti and TiN of different thicknesses deposited on aluminum were evaluated using the same scratch test [28]. The critical loads were substantially lower than those reported here.

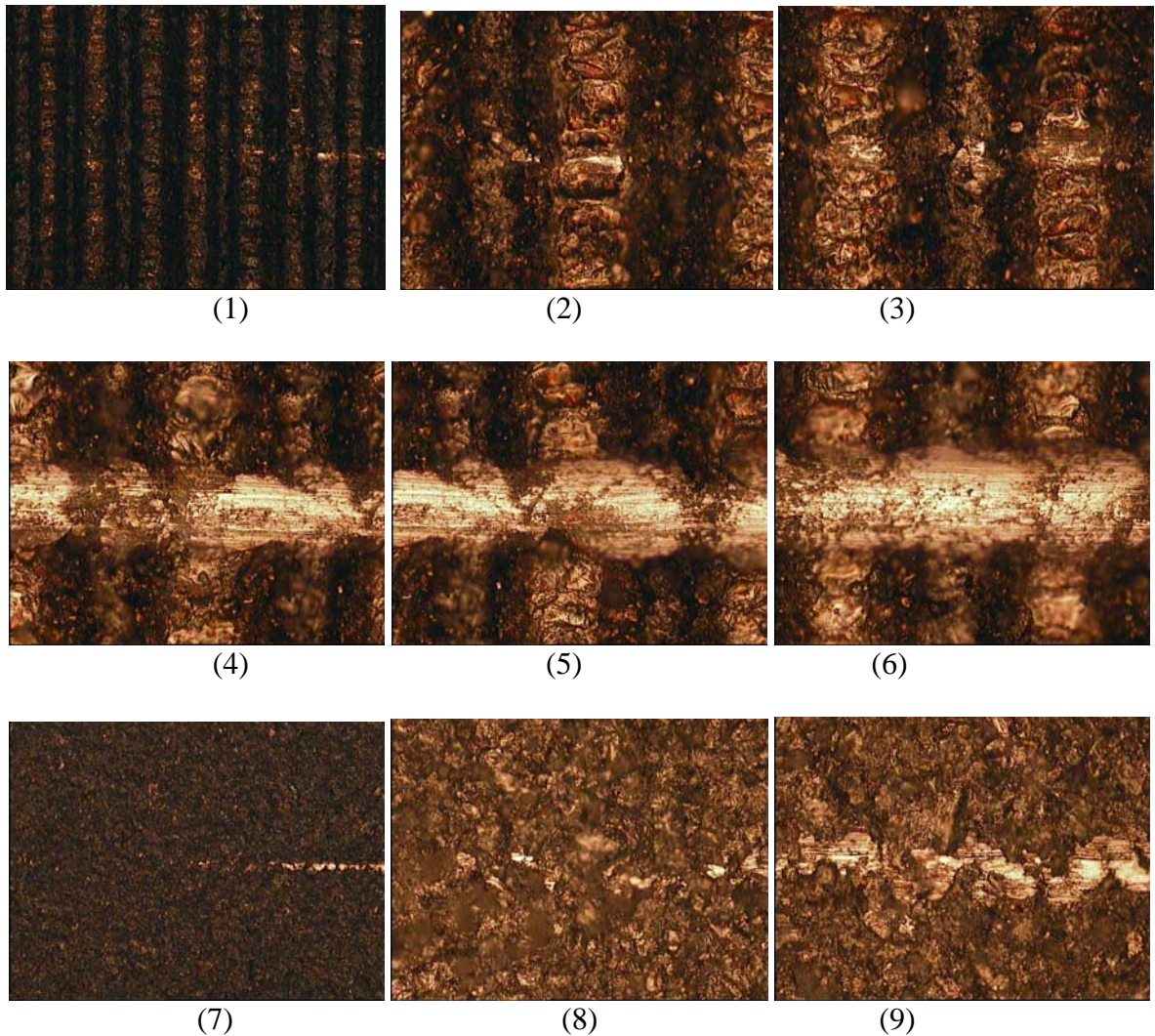


Figure 5.9 Pictures of delamination for sintered and ‘as coated’ sample (1. Sintered - Beginning of Scratch (50x), 2. Sintered – 1st Delamination (200x), 3. Sintered – 1st Delamination Valley (200x), 4. Sintered – Long Delamination (LD) (200x), 5. Sintered – LD (cont...), 6. Sintered – Large/LD (200x), 7. As coated - Beginning of Scratch (50x), 8. As coated – 1st Delamination (200x), 9. As coated – LD (200x)).

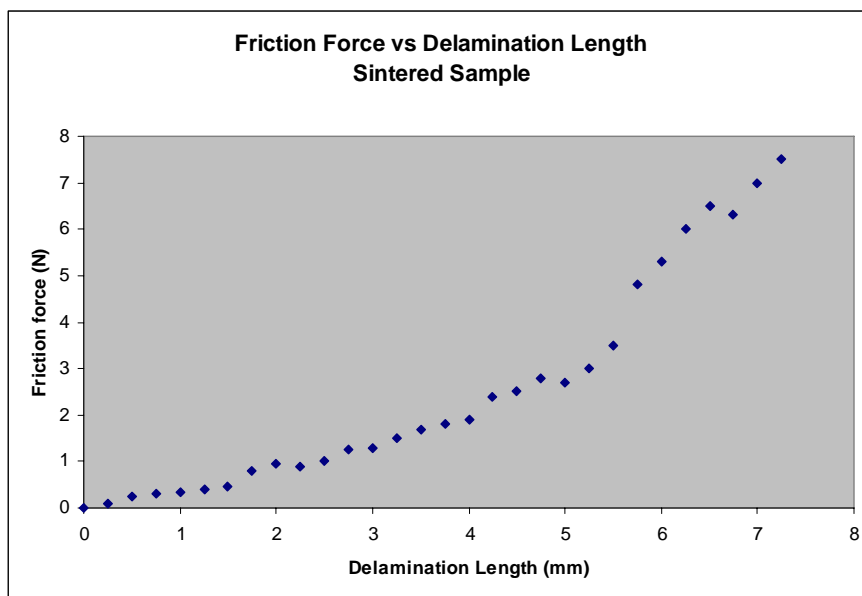


Figure 5.10 Friction force of the sintered sample.

The comparison graph (Figure 5.10) above shows the relationship between the friction force and delamination length for the laser-sintered sample. It can be seen in the figure that the frictional force gradually rises from 0 N to 7.65 N over the test scratch length of 7.5 mm as the depth reaches 9.4 μm which is the approximate thickness of the sintered coating. The friction coefficient fluctuates between 0.2 and 0.5 as the full depth of the coating is reached. As we compare this to the ‘as-coated’ sample (Figure 5.11) where the synthetic diamond powders are deposited and coated uniformly by the electrostatic spray coating process (ESC), it is seen that the friction force rises to 3.6 N over the test length. The friction coefficient fluctuates between 0.1 and 0.4. The higher value of friction force and friction coefficient for the sintered sample can be attributed to the rough surfaces developed due to laser-sintering and the more cohesiveness in the laser-sintered microstructure. The friction force is a function of counter face material and hydrogen content of DLC. For example, the friction

coefficient with steel is 0.2 and with alumina is 0.08 [29]. Most DLC's contain >30 at% hydrogen, making the friction coefficient highly variable.

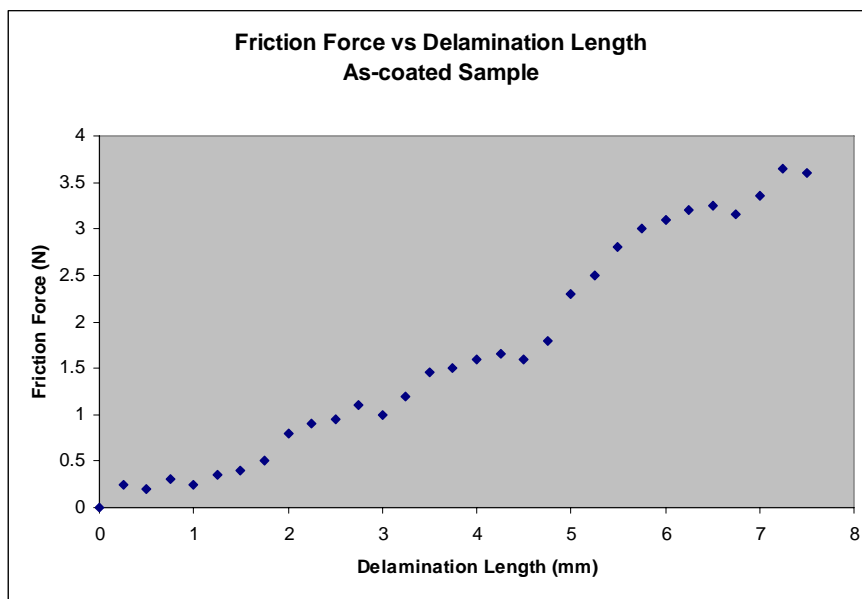


Figure 5.11 Friction force of the 'as-coated' sample.

5.3.6 Raman Spectroscopy

Raman Spectroscopy is a non-destructive technique for the identification of a wide range of substances and has been widely used to study the structure of DLC materials [30]. It involves illuminating a sample with monochromatic light and using a spectrometer to examine light scattered by the sample. The frequency shift corresponding to the energy difference between the incident and scattered photon is termed as the Raman Shift. A plot of detected number of photons versus Raman Shift from the incident laser energy gives a Raman spectrum. Raman spectra of crystals behave differently from that of gases and liquids, as they do not behave as if composed of molecules with specific vibration energy levels, instead the crystal lattice

undergoes vibration and these macroscopic vibration modes are called Phonons. A micro-Raman spectroscopy (*Ramascope, Reinshaw 1000*) using monochromatic light of wavelength 488 nm was used to characterize the coatings. Diamond powder and the powder-coated, laser-treated samples were separately analyzed. The results are as given below.

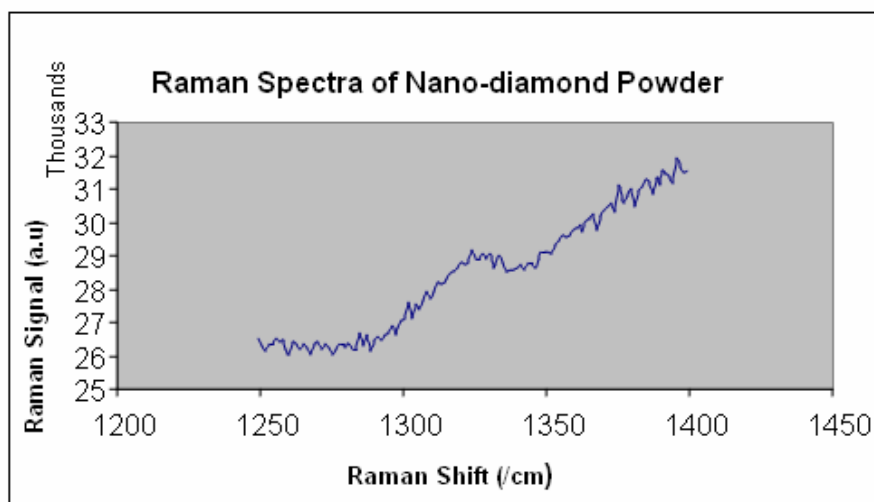


Figure 5.12 Raman Spectra of Nano-diamond Powder.

Natural diamond exhibits one main Raman active vibration which manifests itself as a sharp first order peak in the Raman spectrum at 1332 cm^{-1} . In the nano-powder sample that was tested for Raman Spectra a broader peak can be seen at 1332 cm^{-1} as shown in Figure 5.12. Broadening of the diamond band is a result of decreased grain size (nanometer scale) and impurities. A strong, narrow first order diamond peak, located close to 1332 cm^{-1} , and a lack of features attributable to non-diamond forms usually indicates that the material is of good quality. Since our nano-diamond powder had 2% impurity, a strong, narrow first order peak was not visible. In addition, graphitic inclusions can 'screen out' the diamond signal from

diamond regions deeper in the sample making the Raman spectrum to indicate a worse quality material than is actually the case.

Natural single crystal graphite exhibits a single Raman peak at around 1580 cm^{-1} , namely the G peak. If graphite becomes disordered in the carbon layers, the G peak broadens. For polycrystalline graphite, a second peak at 1350 cm^{-1} appears namely the disordered or the D peak. If the long range order of the crystalline material is lost and the carbon phase becomes glassy, both the G and D peaks broaden. For a laser-processed diamond sample (200 W, 254 mm per second), the Raman Shift shows a broad band over the range of 1200 to 1600 cm^{-1} (Figure 5.13). However, unlike resonant Raman scattering, visible laser light such as 488 nm light is not sensitive to sp^3 carbon bonding in DLC materials. Therefore, fitting D and G peaks has commonly been used to interpret the Raman spectra acquired from DLC materials. The emergence of the D peak can be used to predict the appearance of sp^2 clusters in the coatings containing high sp^3 content [31, 32].

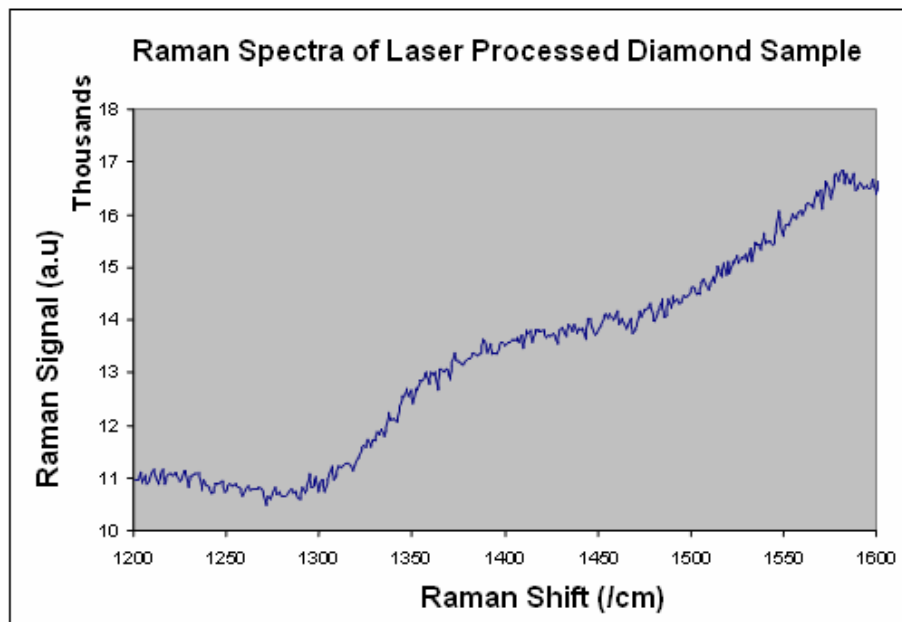


Figure 5.13 Raman Spectra of Laser-processed Diamond Sample (200 W, 254 mm/s).

The Raman spectra for the sintered coating gave a broad band overlaid by G and D peaks. It is well known that the G band of bulk graphite is located at 1580 cm^{-1} of the E_{2g} mode which represents the C-C stretching vibration in the graphite layer. In DLC materials, the decrease in the C-C stretching vibration corresponds to the lengthening of the C-C bond and some carbon atoms leave the layer. Under these conditions interlayer bonds may appear. DLC materials therefore usually show a lower G peak position as is seen in Figure 5.13. Researchers have also shown that for DLC films containing aluminum, both G and D peak positions shifted to lower frequencies as the content of aluminum was increased [31]. Amorphous carbon produces a broad asymmetric hump in the region $1000\text{-}1600\text{ cm}^{-1}$.

5.3.7 Microstructure & Surface Morphology

SEM micrographs of the surface (Figure 5.14) of the laser-sintered samples showed it to be fairly uniform and smooth. EDS (Energy dispersive spectroscopy) spectrum at a magnification of 500X, showed trace amounts of iron, magnesium and silicon, which were reported to be impurities in the synthetic diamond nanopowder. SEM micrograph at a magnification of 4000X shows a near dense coating with very few cracks.

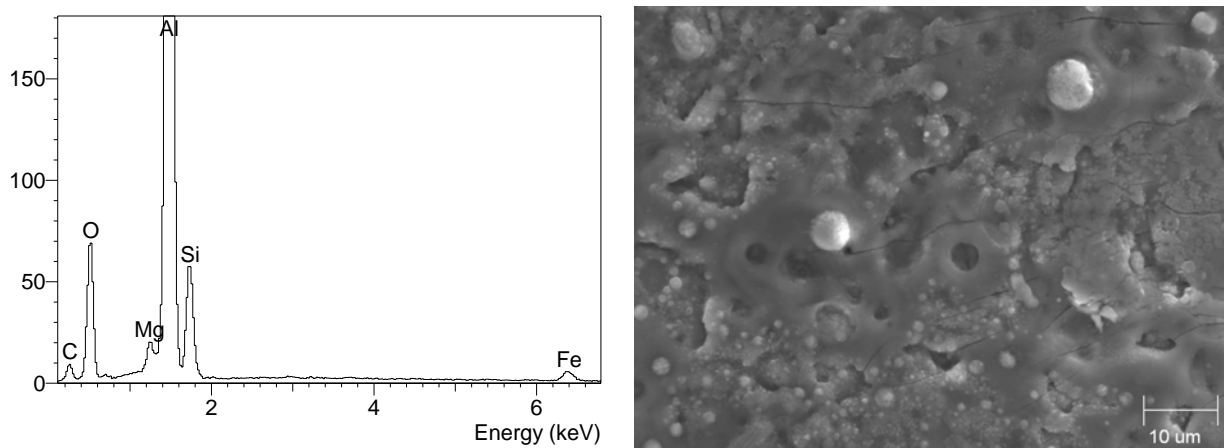


Figure 5.14 EDS and SEM micrograph of the laser-sintered sample (200 W, 254 mm/s).

Polishing and etching (Aqua Regia) of the cross-section of the sintered sample was performed. A very thin layer of gold was coated (*DENTON[®] sputter coater*) on the sample for better resolution and signal quality. This sample was studied under an SEM (Figure 5.15). Etch pits were seen in the interface between the coating and the aluminum substrate possibly due to the use of aqua regia as the etchant. The coating is seen to be fairly uniform and smooth. It is also free from crack, porosity and inclusions.

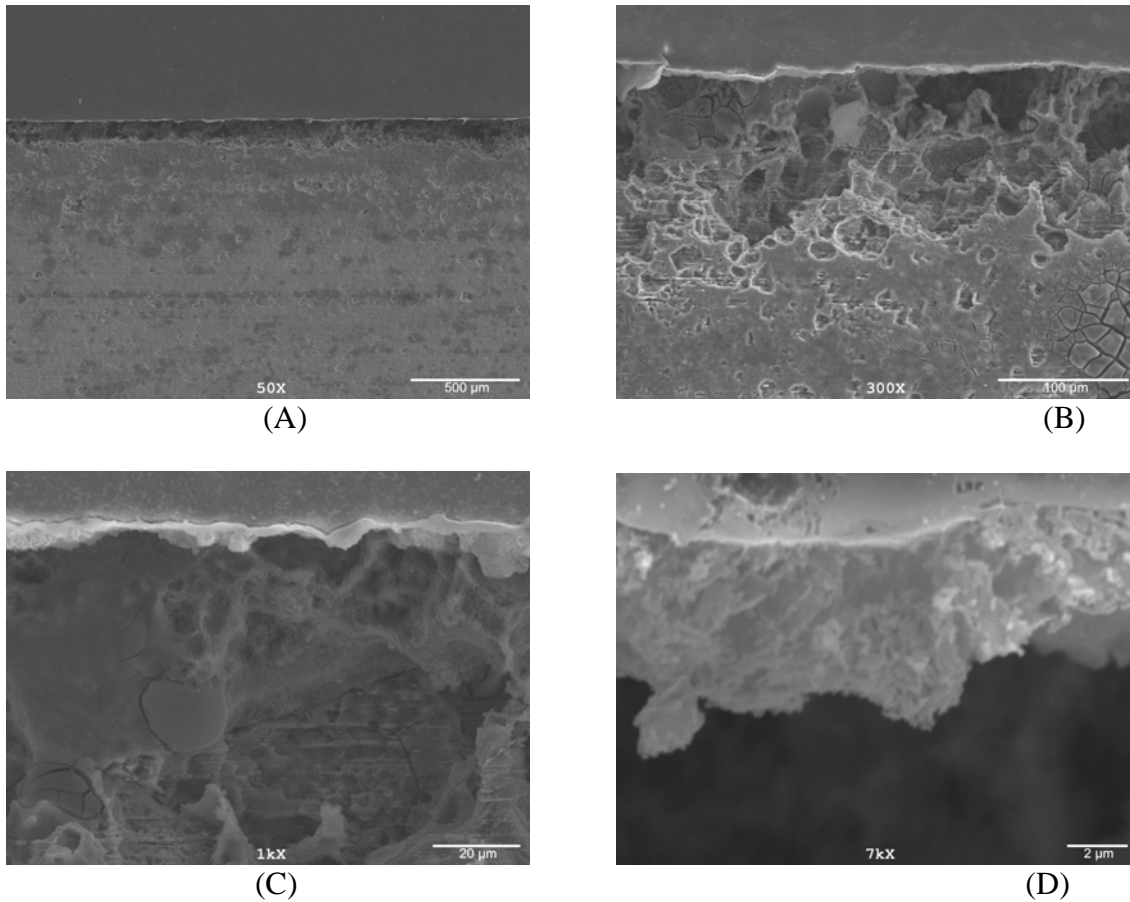


Figure 5.15 SEM micrographs of the laser-sintered sample (200 W, 254 mm/s), A) Coating at 50X magnification, B) At 300X, etch pits can be seen between the coating and the substrate, C) Thin layer of coating with an average thickness of 10 μm , and D) Coating at 7,000X.

5.3.8 X-ray Diffraction (XRD)

XRD patterns from a known or approximated crystal data for the laser-sintered sample proved the existence of DLC coating on the aluminum substrate. However, since a thin film XRD was not done, the data obtained showed only trace amounts of the DLC phase as expected, because the X-rays penetrate deep into the substrate material as well.

As seen in the diffractogram in Figure 5.16, the y-axis is a logarithmic value of the counts and so most of the peaks generated are extremely small in real scale. The aluminum peaks at two-thetas of 38.49, 44.74 and 65.11 are reflective of the face centered cubic (FCC) structure of the aluminum alloy. Two-theta peaks of 28.45, 47.31 and 56.18 represent the presence of silicon, possibly from the silicon content (Si is in the form of inter-metallic compounds) in aluminum 6061. XRD diffractogram clearly shows a DLC peak at Two-Theta (deg.) of 26.61. Rest of the peaks represent the reflection of X-rays from aluminum which exist in orientations other than FCC and can be interpreted as crystalline structures developed as a consequence of the processes involved in the preparation of the coupons of aluminum 6061 T-91, including cold working and heat treatment. There are trace phases of other elements and compounds which are part of the aluminum alloy.

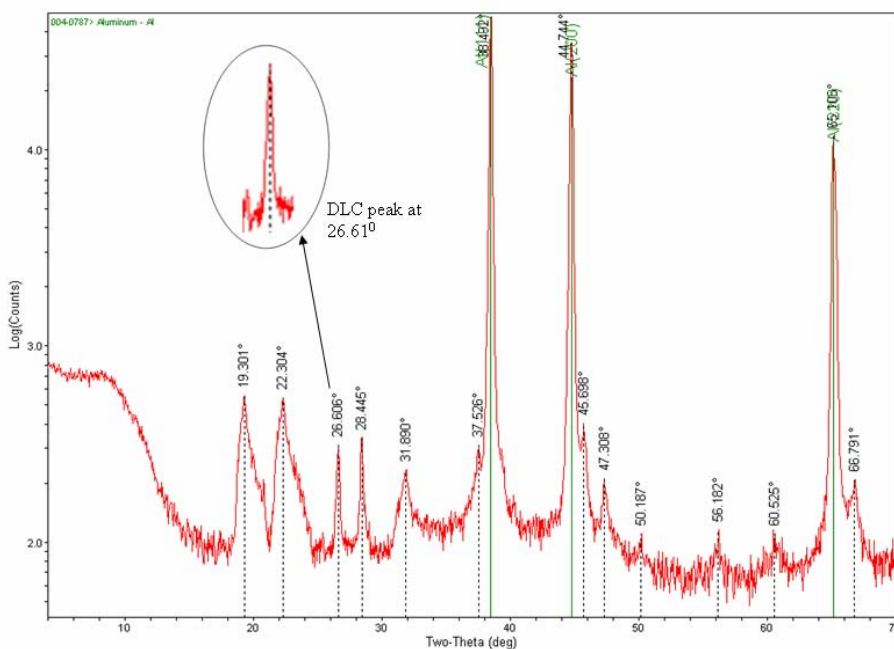


Figure 5.16 XRD diffractogram of the sintered sample.

5.4 Discussion

Among all the nonferrous alloys, aluminum alloys are the most widely used. AA 6061 is the most general purpose aluminum alloy with numerous applications which demand high specific strength, low friction and high wear resistance. While the desired strengths can be achieved through alloying, cold work and heat treatment, the tribological properties of aluminum alloys are usually attained by a variety of surface coating technologies that include anodizing, Cr-electroplating, Ni-P electroless plating, sputtering, CVD and laser alloying/cladding methods.

In this work, we have employed laser-sintering in preference to other coating techniques for the following reasons: anodizing, Cr-plating and PVD coatings are usually too thin and contain a high density of defects. PVD is also limited by the large size and complexity of part as well as by vacuum requirements. In addition, the poor bonding strengths at the coating-substrate interfaces restrict the PVD processes from applying it to high load-bearing components. CVD is a high-temperature process that causes dimensional change, geometric distortion, and grain growth. Laser sintering has the advantage of overcoming many of these obstacles. The general benefits of laser-sintering can be summarized as:

- Better functionality (excellent bonding, less residual stresses, higher hardness)
- Simplicity (absence of vacuum chambers)
- Flexibility (selective area deposition)
- Low substrate temperatures
- Minimal changes in dimensional accuracy
- Fairly smooth surfaces

- Minimal contamination
- Environmental friendly
- Nanostructured coatings due to suppression of grain growth.

Aluminum alloys are traditionally subjected to anodizing treatment, a classical route, to enhance the tribological properties. Anodizing produces an oxide layer at ambient temperature with hardness close to that of high strength steels but well below that of α -alumina, the principal constituent of the oxide coating. Anodized coatings are quite porous, sometimes as much as 50%. In addition, the coating brittleness and the cracks induced during the process strongly affect the fatigue performance. Furthermore, low PH acidic electrolytes used in the process do not meet the environmental regulations. Cr and Ni-P plating processes suffer from similar problems. Recent innovation in anodizing is a controlled oxidation process, designated as microplasmic anodizing by the Microplasmic corporation, which offers the benefits of less environmental damage due to increased pH, less porosity, increased density and much improved hardness of around 1300 kg/mm² [33]. However, studies of micro-arc oxidized aluminum alloys have shown that as-deposited and polished alumina coatings have a relatively high friction coefficient >0.7 [34]. A variety of PVD and CVD coatings such as TiN have been applied to aluminum to improve its tribological properties [28, 35 and 36]. Although PVD-coated TiN or CrN on aluminum alloys exhibited high surface microhardness, the low thickness of coating and thermal/mechanical mismatch of the coating with the substrate did not allow adequate load support in service [36].

One specific coating that had a marked tribological effect on aluminum was DLC which consists mainly of a mixture of “diamond” sp^3 and “graphite” sp^2 hybrid carbon atoms with no long range order. The level of hardness obtained in DLC depends on the volume fractions of two phases. General Motors R&D Center initiated a study of DLC coating (CVD process) for aluminum A390 alloy to determine its potential for improving the tribological properties of the piston bore in automotive engine applications [14]. Results showed the beneficial effects of low friction coefficient and absence of scuffing wear. However the thin coatings ($<2 \mu\text{m}$) performed well only for short time. The life expectancy of a modern combustion engine requires much thicker coatings. However, increasing the DLC coating thickness by CVD processes has detrimental effects such as increased deposition time and increased internal stresses causing delamination. A unique method of combining micro-arc plasma oxidation and plasma implantation was used to deposit thick, dual coatings of alumina and DLC on aluminum alloy parts, which improved the load-carrying capacity [34].

DLC coatings have been deposited using various deposition methods that include ion beam deposition (IBD), magnetron sputter deposition (MSD), and plasma CVD (PECVD). IBD has the advantage of being able to deposit high quality coatings at very low temperatures (near room temperature) but the deposition rate is very low ($1\mu\text{m/hr}$). In addition, complex manipulation of the substrate was required in order to ensure uniform deposition. Plasma-assisted CVD techniques employing RF and DC glow discharges in hydrocarbon gas mixtures produce smooth films but at the expense high substrate temperatures of at least 600°C to give the required combination of properties. This will in turn deleteriously affect the aluminum substrate properties by causing the *overaging*. The CVD technique results in

good deposition rates and very uniform coatings, and is well suited to large-scale production. Another technique is unbalanced magnetron sputter ion plating that has recently been developed to apply thick coatings (4 μm) at 200°C with much improved adhesion to any substrate. This technique combines the benefits of both plasma CVD and ion beam deposition.

Laser sintering of DLC coatings carried out in this work is certainly advantageous over the current techniques as can be seen from Table 5.5. DLC coatings could be produced because high-energy precursive carbon atoms are rapidly cooled on the relatively cold surfaces. Here cubic and hexagonal phases are randomly intermixed because of the lack of time for one crystalline phase to grow at the expense of other phase.

The shrinkage behavior of laser-sintering affects the density and formation of residual stresses. The electrostatic spray coated samples had an average thickness of 25 μm . The nano-diamond particles are loosely attached with the substrate (van Der Waals bonds), resulting in a substantial amount of porosity. Upon laser-sintering, the average thickness was reduced to 10 μm . In addition, there was an intermixed layer (aluminum and DLC) of about 60 μm observed. Laser sintering consolidates the electrostatic spray coating to near theoretical density with little evidence of porosity. This is essentially attributed to localized thermal diffusion that binds the particles and causes shrinkage. There is also some melting and resolidification of aluminum that increases the amount of shrinkage. The residual stresses in the laser-sintered coatings are expected to be much lower than CVD and PVD processes primarily due to its localized nature.

Laser surface cladding and alloying of aluminum alloys using different metals and ceramics have been carried out by a number of researchers [37-43]. Various degrees of improvements on the surface hardness and wear-resistant properties have been reported. However none of these works dealt with DLC coatings as well as laser-sintering of electrostatic sprayed coatings. As has been demonstrated, the formation of a well adhered, very hard, good toughness and low friction DLC coating on aluminum substrate by laser-sintering has potential economic benefits for a wide variety of mechanical parts.

Table 5.5 Comparison of coating characteristics produced by laser-sintering (current work) and other methods (previous works).

Characteristic	Other Methods	Laser-sintering
Hardness, Vickers	1000-1500	2000-2500
Deposition Temperature, °C	20-600	27
Deposition time	Long	Short
Friction coefficient	0.1 – 0.3	0.1 – 0.4
Coating thickness, μm	0.001 to 4	9
Surface roughness	Fine	Coarse
Adhesion	Weak	Strong
Deposition equipment	Complex	Simple
Environmental effect	Malign	Benign

5.5 Conclusions

Electrostatic spray coating technique was utilized to deposit a fairly uniform coating of nominal thickness 25 μm diamond nanopowders on industry standard Aluminum 6061 T-91 substrates. Laser sintering was then followed up to create a uniform 10 μm thick DLC surface with excellent surface properties such as microhardness, fracture toughness and scratch critical force and good structural integrity. Laser power and scanning speed played

vital roles in obtaining the uniform DLC coating. Vickers microhardness number of 22.5 GPa falls in the category of super-hard materials. Fracture toughness values are as expected of a DLC coating in the range of 1 to 2.3 MPa \sqrt{m} . Although scratch critical forces could not be compared to other industry standard DLC coatings, the value of 4.51 N obtained for the laser-sintered sample was almost 4 times, greater than the electrostatic spray coated (non-sintered) specimen. Average surface roughness was in the desired range of 1 to 1.5 μm . Raman spectroscopy measurements showed a broad asymmetric hump in the region of 1000–1600 cm^{-1} confirming the presence of a fairly uniform DLC coating. Finally, X-ray diffractogram proved the existence of the DLC coating with a two-theta peak at 26.61 degree. Results of the present work offer a new method of DLC coating of aluminum with advantages of simplicity, cost effectiveness, environmentally benign, enhanced properties and improved bonding over CVD and PVD coating methods. In addition, it also provides an excellent alternative to the existing anodizing and microplasmic coating processes for improving the tribological performance of aluminum.

Acknowledgements

The authors would like to thank Dr. Anatoli Frishman, Dr. Warren Straszheim, Mr. Hal Sailsbury and Mr. Scott Schlorholz for their help during this research.

References

1. Zhu, H. and Averback, R. S. (1996). Sintering Processes of two nanoparticles: a study by molecular-dynamics simulations. *Philosophical Magazine Letters*, Vol. 73, No. 1, pp. 27-33.

2. Jiang, W., Malshe, A. P. and Brown, W. D. (2004). Physical powder deposition of solid lubricant nanoparticles by electrostatic spray coating (ESC). *Surface and Coatings Technology*, Vol. 177 –178, pp. 671–675.
3. Williams, J. D. (1997). Numerical modeling and experimental analysis of selected parameter effects on the selective laser sintering process response. *M.S Thesis*, Clemson University, Clemson, SC.
4. Wielage, B. and Dorner, A. (1998). Bonding and sliding wear behavior of diamond-like carbon coatings on fiber reinforced aluminum. *Surface and Coatings Technology*, Vol. 108–109, pp. 473–478.
5. Malaczynski, G., Hamdi, A. H., ElmoursI, A. A. and Qiu, X. (1997). Diamond-like carbon coating for aluminum 390 alloy – automotive applications. *Surface & Coatings Technology*, Vol. 93, pp. 280-286.
6. Li., L. H., Tian, X. B., Chu, P. K., Zhang, Y. H, Cui, X. M. and Zhang, H. Q. (2003). Growth and nucleation of Diamond-like carbon (DLC) film on aluminum. *Nuclear Instruments and Methods in Physics Research B*, Vol. 206, pp. 691–695.
7. Liao, J. X., Xia, L. F., Sun, M. R., Liu, W. M., Xu, T., and Xue, Q. J. (2004). The tribological properties of a gradient layer prepared by plasma-based ion implantation on 2024 aluminum alloy. *Surface and Coatings Technology*, Vol. 183, pp. 157–164.
8. Oka, Y., Tao, M., Nishimura, Y., Azuma, K., Fujiwara, E., and Yatsuzuka, M. (2003). Properties of thick DLC films prepared by plasma-based ion implantation and deposition using combined RF and H.V. pulses. *Nuclear Instruments and Methods in Physics Research B*, Vol. 206, pp. 700–703.

9. Jacobs, P. F. (1992). *Rapid Prototyping & Manufacturing: Fundamentals of Sterolithography*, Society of Manufacturing Engineers.
10. Bugada, G., Cervera, M. and Lombera, G. (1999). Numerical prediction of temperature and density distribution in selective laser sintering process. *Rapid Prototyping Journal*, Vol. 5, No. 1, pp. 21-26.
11. Childs, T. H. C. and Tontowi, A. E. (2001). Selective laser sintering of a crystalline and glass-filled crystalline polymer: Experiments and simulations. *Proc. Inst. Mech. Engrs*, Vol. 215, No. B, pp. 1481-1495.
12. Agarwala, M., Bourell, D., Beaman, J., Marcus, H. and Barlow, J. (1995). Direct selective laser sintering of metals. *Rapid Prototyping Journal*, Vol. 1, No. 1, pp. 26-36.
13. Van der Schueren, B., and Kruth, J. P. (1995). Powder deposition in selective metal powder sintering. *Rapid Prototyping Journal*, Vol. 1, No. 3, pp. 23-31.
14. German, R. M. (1990). Supersolidus liquid phase sintering. Part II: Densification theory. *International Journal of Powder Metallurgy*, Vol. 26, No. 1, pp. 35-42.
15. Subramanian, P. K., Vail, N. K., Barlow, J. W., and Marcus, H. L. (1995). Selective laser sintering of alumina with polymer binders. *Rapid Prototyping Journal*, Vol. 1, No. 2, pp. 24-35.
16. Yagi, S. and Kunii, D. (1957). Studies in the effective thermal conductivities in packed beds. *American Institute of Chemical Engineers Journal*, Vol. 3, No. 3, pp. 373-381.
17. Tolochko, N. K., Laoui, T., Khlopkov, Y. V., Mozzharov, S. E., Titov, V. I., and Ignatiev, M.B. (2000). Absorptance of powder materials suitable for laser sintering. *Rapid Prototyping Journal*, Vol. 6, No. 3, pp. 155-160.

18. MatWeb.com, The Online Materials Database. <http://www.matweb.com>, *Properties of Aluminum 6061 T-91*, Retrieved – January, 15th, 2006.
19. Ouyang, J. H., Nowotny, S., Richter, A. and Beyer, E. (2001). Laser cladding of yttria partially stabilized ZrO₂ (YPSZ) ceramic coatings on aluminum alloys. *Ceramics International*, Vol. 27, pp. 15-24.
20. ASM Metals Handbook[®], Heat Treating, Ninth edition, Volume 4, *American Society for Metals*, Metals Park, Ohio 44073
21. Bursill, L. A., Fullerton, A. L. and Bourgeois, L. N (2001). Size and Surface Structure of Diamond Nano-Crystals. *International Journal of Modern Physics B*, Vol. 15, No. 31, pp. 4087-4102.
22. Dubrovinskaia, N., Dubrovinsky, L., Langenhorst, F., Jacobsen, S. and Liebske, C. (2005). Nanocrystalline diamond synthesized from C₆₀. *Diamond and related materials*, Vol. 14, pp. 16-22.
23. Melvin, L. and Beaman, J. (1991). The Electrostatic Application of Powder for Selective Laser Sintering. *Proceedings: Solid Freeform Fabrication Symposium*, University of Texas, Austin Texas, pp. 171- 177.
24. Parker, A. P. (1981). *The mechanics of Fracture and Fatigue*. E and F. N. Spon, London.
25. Li, X. and Bhushan, B. (1998). Measurement of Fracture Toughness of Ultra-thin Amorphous Carbon Films. *Thin Solid Films*, Vol. 315, pp. 214-221.
26. Anstis, G. R., Chantikul, P., Marshall, D. B. and Lawn, B. R. (1981). A Critical Evaluation of Indentation Techniques for Measuring Fracture Toughness: I. Direct Crack Measurements. *Journal of American Ceramic Society*, Vol. 64, pp. 533-539.

27. Oka, Y., Nishimura, Y., and Yatsuzuka, M. (2004). DLC coating of a few microns in thickness on three-dimensional substrates. *Vacuum*, Vol. 73, pp. 541–547.
28. Ashrafizadeh, F. (2000). Adhesion evaluation of PVD coatings to aluminium substrate. *Surface and Coatings Technology*, Vol. 130, pp. 186-194.
29. Luo, S. Y., Kuo, J., Yeh, B., Sung, J. B., Dai, C. and Tsai, T. J. (2001). The tribology of nano-crystalline diamond. *Materials Chemistry and Physics*, Vol. 72, Issue 2, pp. 133-135.
30. Nishimura, Y., Ohkawa, R., Oka, H., Akamatsu, H., Azuma, K. and Yatsuzuka, M. (2003). Uniform coating of thick DLC film on three-dimensional substrates. *Nuclear Instruments and Methods in Physics Research B*, Vol. 206, pp. 696–699.
31. Liu, E., Shi, X., Tay, B. K., Cheah, L. K., Tan, H. S., Shi, J. R., and Sun, Z. (1999). Micro-Raman spectroscopic analysis of tetrahedral amorphous carbon films deposited under varying conditions. *Journal of Applied Physics*, Vol. 86, No.11, pp. 6078-6083.
32. Liu, E., Gao, J. X., Zeng, A. P., Tay, B. K., and Shi, X. (2002). Tribological behavior of nanocomposite diamondlike carbon-aluminum films. *Material Research Society Symposium Proceedings*, Vol. 695, pp. 231-236.
33. Patel, J. and Saka, N. (1999). *Microplasmic coating shows high resistance to wear, heat and corrosion*. <http://www.nasatech.com/Briefs/Oct99/ETB10991.html>, Retrieved – November, 16th, 2006.
34. Nie, X., Wilson, A., Leyland, A. and Matthews, A. (2000). Deposition of duplex Al₂O₃/DLC coatings on Al alloys for tribological applications using a combined micro-arc oxidation and plasma-immersion ion implantation technique. *Surface and Coatings Technology*, Vol. 131, Issues 1-3, pp. 506-513.

35. Monaghan, D. P., Laing, K. C., Logan, P. A., Teer, P. and Teer, D.G. (1993). How to deposit DLC successfully. *Materials World*, Vol. 1, no. 6, pp. 347-49.
36. Fuchs, O., Friedrich, C., Berg, G., Broszeit, E., Leyland, A. and Matthews, A. (1998). Hard coatings on light-metal components under mechanical surface loading. *Materialwissenschaft und Werkstofftechnik*, Vol. 29, Issue 3, pp. 141-152.
37. Almeida, A., Anjos, M., Vilar, R., Li, R., Ferreira, M. G. S., Steen, W. M. and Watkins, K. G. (1995). Laser alloying of aluminium alloys with chromium. *Surface and Coatings Technology*, Vol. 70, pp. 221–229.
38. Tomlinson, W. J. and Bransden, A. S. (1995). Cavitation erosion of laser surface alloyed coatings on Al-12%Si. *Wear*, Vol. 185, pp. 59–65.
39. Hu, C., Xin, H. And Baker, T.N. (1996). Formation of continuous surface Al-SiCp metal matrix composite by overlapping laser tracks on AA6061 alloy. *Materials Science and Technology*, Vol. 12, pp. 227–232.
40. Watkins, K. G., McMahon, M. A. and Steen, W. M. (1997). Microstructure and corrosion properties of laser surface processed aluminium alloys: a review. *Materials Science and Engineering: A*, Vol. 231, Issues 1-2, pp. 55–61.
41. Fu, Y., Batchelor, A. W., Gu, Y., Khor, K. A. and Sing, H. (1998). Laser alloying of aluminum alloy AA 6061 with Ni and Cr. Part 1. Optimization of processing parameters by X-ray imaging. *Surface and Coatings Technology*, Vol. 99, Issue 3, pp. 287 294.
42. Kelly, J., Nagarathnam, K. and Mazumder, J. (1998). Laser cladding of cast aluminum-silicon alloys for improved dry sliding wear resistance. *Journal of Laser Applications*, Vol. 10, Issue 2, pp. 45–54.

43. Man, H. C, Kwok, C. T. and Yue, T. M. (2000). Cavitation erosion and corrosion behaviour of laser surface alloyed MMC of SiC and Si₃N₄ on Al alloy AA6061. *Surface and Coatings Technology*, Vol. 132, Issue 1, pp. 11–20.

CHAPTER 6. Thermal Transport Analysis of Laser Sintering of Nanocrystalline Diamond Powders on Aluminum Substrate

Paper submitted to *Surface Coatings and Technology*, 2007

Rajeev Nair and Pal Molian

Nomenclature

<p>A laser spot size area [m^2] A_H area fraction of the holes C_p specific heat [$\text{J kg}^{-1} \text{K}^{-1}$] E Youngs modulus of elasticity [Pa] E_a activation energy [kJ mol^{-1}] f_g probability of phase transformation $G_{T,P}^g$ Gibbs free energy for graphite g volumetric heat generation [W m^{-3}] h heat transfer coefficient [$\text{W m}^{-2} \text{K}^{-1}$] K_s thermal conductivity of solid [$\text{W m}^{-1} \text{K}^{-1}$] K_g thermal conductivity of gas [$\text{W m}^{-1} \text{K}^{-1}$] K_{eff} effective thermal conductivity [$\text{W m}^{-1} \text{K}^{-1}$] L plate length [m] L_b length of the laser beam [mm] Nu Nusselt number Pr Prandtl number P total laser power [W] P' power absorbed by the powder surface [W] \dot{Q} heat flux [W m^{-2}] R gas constant Re Reynolds number t time [s] T temperature [K] T_S surface temperature [K] T_f film temperature [K] T_A ambient temperature [K] T_{env} environment temperature [K] T_0 uniform temperature [K] u_a flow velocity of argon gas [$\text{m}^3 \text{s}^{-1}$] V_s laser beam velocity [mm s^{-1}]</p>	<p>W_b width of the laser beam [mm] x coordinate [m] X dimensionless coordinate y coordinate [m] Y dimensionless coordinate z coordinate [m] Z dimensionless coordinate Z_B bottom of the substrate [m]</p> <p><i>Greek symbols</i></p> <p>ρ density [kg m^{-3}] ϕ porosity parameter ϕ empirical coefficient χ absorptivity ε emissivity ε_H emissivity of the hole ε_S emissivity of the solid σ Stephan-Boltzmann constant ∇ divergence operator ∂ partial derivative α thermal diffusivity [$\text{m}^2 \text{s}^{-1}$] ν kinematic viscosity [$\text{m}^2 \text{s}^{-1}$] μ dynamic viscosity [$\text{kg m}^{-1} \text{s}^{-1}$] σ_z thermal stress [Pa] β coefficient of expansion [K^{-1}] Δ difference</p>
--	---

Abstract

Laser sintering of electrostatically-sprayed diamond nanopowder (size 4-8 nm, nominal thickness 25 μm) on aluminum 6061 T-91 substrate was carried out using a continuous wave

CO₂ laser. The optimum laser parameters were experimentally determined to be 200 W (laser power) and 254 mm/s (scanning speed) based on the criterion of maximum hardness of coating. The optimal coating consisted of a mixture of mostly diamond-like carbon (DLC, accounting for a hardness of 2250 kg/mm²) and some nanocrystalline diamond (hardness of 9000 kg/mm²). Finite element model (FEM) solutions of one-dimensional thermal energy transport through the powder bed were obtained for these optimal laser parameters. The heat transfer and parametric design capabilities of the FEM code ANSYS were employed for this purpose. Thermal properties of the diamond powder bed and aluminum 6061 T-91 were evaluated and applied in these models. The steady state and transient temperature profiles along the depth of the coating and substrate as well as the time-dependent cooling in the case of transient model were obtained and used to validate the experimentally-obtained coating thickness and phase transition. Inclusion of convection in the models showed negligible effects of shield gas on the temperature distributions during heating and cooling. A hypothesis of the events that occur during laser sintering is postulated based on the evidence obtained from both model and experiment. Finally, thermal expansion coefficients of the coating and the substrate were used to determine thermal stresses at the coating-substrate interface.

6.1 Introduction

Laser sintering (LS) is a manufacturing technique which uses raster scanning of a laser beam to a specific shape, dictated by a computer-aided design solid model, to sinter powder material and thereby produce three-dimensional objects and coatings [1-5]. Sintering normally refers to furnace processes where the powder compacts are heated to elevated

temperatures, usually close to its melting point, where diffusion mass transport is appreciable so that binding occurs at the interfacial grain contacts [6]. However, LS is advantageous over furnace sintering by suppressing the grain growth and particle agglomeration, minimizing the contamination, and reducing the sintering temperature. LS generate homogeneous and dense layers while furnace sintering produces layers consisting of agglomerates and inter-agglomerate pores. For example, Macedo and Hernandez [7] reported that laser sintering of ceramics produced finer grain size (50% smaller) and much denser (95%) parts than those obtained in electric furnace sintering. In addition, LS is a line-of-sight technique providing simplicity, flexibility and environmental safety in processing complex shapes while achieving the functionality, dimensional accuracy, smooth surface, and fine microstructure of the components.

In laser sintering, the use of nano-sized particles is quite attractive over micro-sized particles because sintering can be done at substantially lower temperatures. In addition, nanoparticles can better absorb laser light. Both these effects are attributed to large surface area-to-volume ratio of nanoparticles. Furthermore, the melting temperature decreases markedly with particle size reduction in the nanoscale range [8]. Molecular dynamics simulations [9] showed sintering of nanoparticles proceeds extremely fast due to mechanisms such as dislocation motion, particle rotation and viscous flow in addition to surface and volume diffusion. Consequently, laser sintering would be preferred to match the speed at which nanopowder sintering takes place. Studies of laser sintering of nanopowders indicate the onset of sintering temperature is $0.2-0.3 T_m$ as compared to $0.5-0.8 T_m$ for microscale powders where T_m is the melting temperature [9]. Furnace sintering studies of WC/Co

showed that nanopowder starts to shrink at much lower temperatures than micropowder and concluded that nanopowder densifies mostly in the solid state while the micropowder densifies in the liquid state [10].

In this work, laser sintering of nanocrystalline diamond powders (4-8 nm) on aluminum 6061 substrate was performed to create a fairly thick layer of diamond-like carbon (DLC), alternatively known as tetrahedral-amorphous carbon films. DLC exhibits high hardness due to the significant fraction of sp^3 hybridized carbon atoms [11]. DLC has many potential applications due to their superior thermal, electronic, optical, mechanical and tribological properties [12-15].

The melting point of diamond is 3800 K. For nanocrystalline diamond powders, temperatures around 800-1200 K ($0.2-0.3 T_m$) are expected to cause binding along the particle surfaces. However, at these temperatures, nanocrystalline diamond can potentially undergo phase transition to fully graphitic phase if it is held for a longer time such as in furnace annealing, even under an inert gas environment [16].

In this paper, experimental results of DLC coating formation, coating thickness, size of heat affected zone and adhesion strength are corroborated with finite element solution of thermal energy transport models which take into account laser energy absorption, powder densification, heat conduction and convection. We have utilized one-dimensional steady and transient heat flow models to explain the observed results. Dabby and Paek presented a transient one-dimensional model considering the penetration of radiation into the material

[17]. Noguchi, *et al.* applied the enthalpy method to formulate a one-dimensional volumetric heating model and solved it using a finite element technique [18]. Mazhukin, *et al.* analyzed the volume overheating of solid and liquid phases in pulsed laser evaporation of superconducting ceramics using a one-dimensional model [19]. It may be noted that there are several analytical and numerical models ranging from 1-D to 3-D available for predicting the effects of laser-induced heating.

6.2 Experimental procedure and results

Sample coupons of aluminum alloy 6061-T91 with a size of 25 mm x 25 mm x 9.5 mm were prepared by cutting and grinding from a large plate stock. Nanocrystalline diamond powders with a size range of 4-8 nm were electrostatically sprayed on the aluminum coupons for a nominal thickness of 25 μm . A high-power continuous wave CO₂ laser (*820 Spectra – Spectra Physics*[®]) was then used to densify and sinter the diamond powders. A focused rectangular beam (length of 1 mm by width of 0.1 mm) was chosen for the process. The laser beam in raster scan configuration, controlled by a programmed CNC controller, was used to sinter the nanoparticles. Argon was used as the assist gas during the sintering process. Numerous laser parameter variations such as laser power and scan rate were attempted. The optimum laser parameters were determined based upon the criterion of maximum hardness and listed in Table 6.1.

Following laser sintering, the coatings were evaluated for densification, phase transformation, hardness, coating thickness and coating/substrate interface strength. Detailed examination of the coating using a variety of instruments (presented in Chapter 5) revealed

>99% dense, mixture of DLC (>90%) and diamond phases for a nominal thickness of 10 μm , and average hardness of 2250 kg/mm^2 . A few regions exhibited hardness of nearly 9000 kg/mm^2 . Figure 6.1 shows a scanning electron micrograph showing the regions of coating, heat affected zone (HAZ) and substrate. HAZ is essentially a zone of overaging in precipitation hardened alloys where the precipitates become coarse and the material becomes quite heterogeneous. Consequently, the etchant aqua regia had a severe attack through ensuing chemical reactions and creating etch pits (Figure 6.1).

Table 6.1 Optimal Process Parameters.

Parameter	Value
Laser power, Watt	200
Focal length of lens, mm	127
Spot area at the powder surface, mm^2	0.1
Scanning speed, mm/sec	254
Standoff distance from the nozzle to the substrate, mm	15
Overlap among passes, %	15-25
Assist gas flow rate, $\text{m}^3/\text{s}(*10^{-4})$	3.15

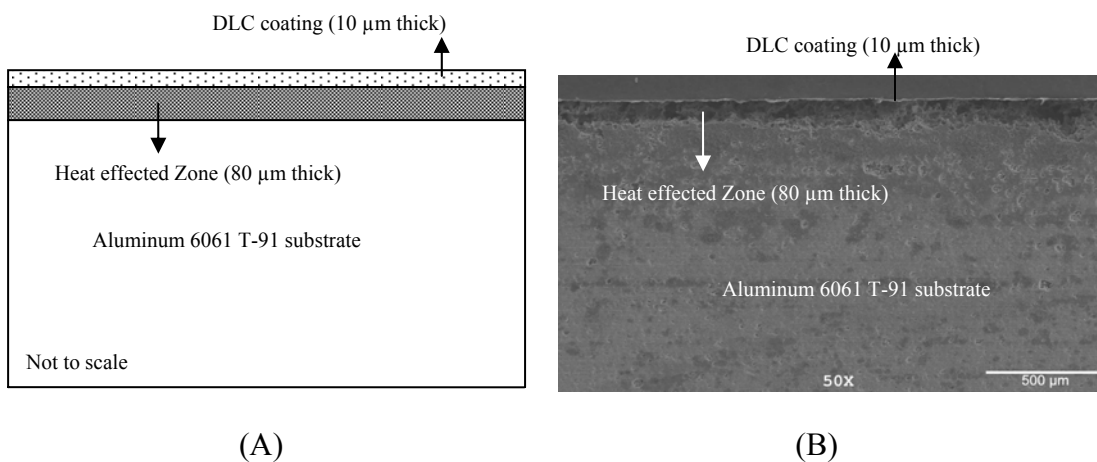


Figure 6.1 (A) Schematic, and (B) SEM micrograph of the transverse section of the coating.

6.3 Thermal energy transport model description

Laser sintering involves several physical phenomena including energy absorption, heating of the powder, binder melting, densification and sintering of particles. Laser power, energy distribution, spot size, beam speed, and extent of overlapping control these phenomena. The incident angle of the beam is kept normal to the powder bed source to minimize the reflective energy losses. Multiple scattering occurs and helps in a nearly homogeneous distribution of the radiation in the powder bed. Energy absorption is also enhanced by the powder porosity. Densification begins in the solid state based on the hypothesis that the nanoparticles rearrange rapidly and diffusion rate is much higher. In contrast, the sintering behavior of micropowders is such that there is no measurable shrinkage until close to the melting point where densification becomes rapid and the specimen is fully sintered by liquid-phase [10]. It is also possible that the laser energy heats and melts the aluminum substrate and enough liquid is produced to achieve liquid-phase sintering with an inter-particle connection to minimize surface energy. In thermal analysis, the individual diamond particle is considered as a dense material while the surrounding air is approximated by a low thermal diffusivity continuum. The process model has several parts as described below.

6.3.1 Properties of Powder Bed, Substrate and Assist Gas

Powder Bed: The nanocrystalline diamond powder received had 2% metallic impurities and moisture. Electrostatic spraying resulted in an average thickness of the powder bed as 25 μm . The degree of packing of a powder bed is characterized by the relative density, ρ_R defined as:

$$\rho_R = \frac{\rho}{\rho_s} \quad (1)$$

where ρ is the density of the powder bed and ρ_s is the theoretical density of the solid. The determination of actual powder bed density is an uncertain process. There are some idealized extremes, one of which involves the assumption that all the solid particles in the powder are spheres of equal size/density arranged in a cubic array. In such a case the bed density is given by $\rho = \frac{\pi\rho_s}{6}$, and hence ρ_R becomes 52.3 % [20]. The porosity content can be estimated from the porosity parameter as:

$$\varphi = 1 - \rho_R = 0.477 \text{ or } 47.7\%. \quad (2)$$

Actual powder beds in laser sintering exhibit porosities between 40 and 60% [20]. It is assumed in our study that the porosity is 55%, which makes the porosity parameter $\varphi = 1 - \rho_R = 0.55$. Since the solid theoretical density of polycrystalline diamond is $\rho_s = 3500 \frac{kg}{m^3}$ and $\rho_R = 0.45$, the density of powder bed becomes $\rho = 1575 \frac{kg}{m^3}$. When the powder particles are composed of the same material, and voids are filled with air, the specific heat capacity C_p of the powder bed is practically same as the solid particles [21-23], which in this case, is composed of nanocrystalline diamond powders.

Heat transfer through powder bed mainly occurs through conduction and radiation since inter-particle distances are too small to permit convection heat transfer. Powder particles are separated by gas in the bed and since gases have smaller thermal conductivities at room temperature, the thermal conductivity of a powder bed is essentially dictated by the gas (air in this case) embedded within the voids [22, 24]. Effective thermal conductivity of a powder

bed including radiation, convection and conduction effects was given by Yagi and Kunii [25] as,

$$K_{eff} = \frac{\rho_R K_s}{\left(1 + \frac{\phi K_s}{K_g}\right)} \quad (3)$$

Where, K_s is the solid thermal conductivity, K_g is the thermal conductivity of air which surrounds the diamond nanoparticles and ϕ is an empirical coefficient given by:

$$\phi = 0.02 * 10^{2(0.7 - \rho_R)} \quad (4)$$

Temperature-dependent numerical values of specific heat and effective thermal conductivity of the powder bed used for the finite element modeling are enumerated in Table 6.2. These properties are assumed to be constant after 1100 K.

Table 6.2 Some thermo-physical properties of the powder bed [26-28].

Temp. (K)	K_s (W/m K)	K_g (W/m K)	K_{eff} (W/m K)	C_p (J/Kg K)
300	2050	0.0262	0.1864	500
400	1500	0.0338	0.2404	875
500	1250	0.0407	0.2894	1125
600	1000	0.0469	0.3335	1375
700	950	0.0524	0.3725	1525
800	900	0.0575	0.4087	1700
900	850	0.0626	0.4449	1750
1000	850	0.0676	0.4804	1800
1100	850	0.0726	0.5159	1850

Substrate: Aluminum 6061 T-91 was selected as the substrate in this study for a number of reasons. It is an excellent structural material with beneficial characteristics such as light weight, good strength and high corrosion resistance. It is also an excellent substrate material for deposition of coatings. It is used in a wide variety of products and applications [29, 30].

Properties of aluminum 6061 T-91 used in thermal analysis are listed in Table 6.3. However, it lacks tribological properties for which DLC coatings would be the most preferred choice [31].

Table 6.3 Thermo-physical properties of aluminum 6061 T-91 [29].

Temp. (K)	K (W/m K)	C _p (J/Kg K)
300	170	892
400	175	947
500	170	993
600	165	1047
700	160	1086
800	155	1148
900	150	1226

Assist Gas: Argon, used as the shield gas during laser sintering, creates convection heat transfer. Hence, it is imperative to calculate heat transfer coefficient (h) of argon. In order to calculate h , the surface temperature must be known. For this purpose we have assumed a surface temperature of 1200 K (based on transient heat conduction model that will be shown later). The film temperature, T_f is the average of the surface temperature and the ambient temperature (300 K).

$$T_f = \frac{T_s + T_A}{2} = 750K \quad (5)$$

Dynamic viscosity and density of argon at 750 K are $44.5 \cdot 10^{-6}$ kg/ms and 1.784 kg/m³ respectively [25]. Hence the kinematic viscosity is,

$$\nu = \frac{\mu}{\rho} = 24.94 \cdot 10^{-6} \frac{m^2}{s} \quad (6)$$

It is necessary to understand whether the flow of argon gas over the diamond powder is a laminar or turbulent one. The Reynolds number is hence calculated as follows.

$$\text{Re}_L = \frac{u_\alpha L}{\nu} \quad (7)$$

where u_α is the flow velocity of argon gas and L is the plate length over which the gas flows. u_α is 27.59 m/s for a gas flow rate of $3.15 \times 10^{-4} \text{ m}^3/\text{s}$ through a pipe of diameter 0.00381 m and L is 0.0254 m. This gives a Reynolds number of 28,100 which is well below 100,000 necessary for developing full turbulent flow over a flat plate [24].

For a flat plate in parallel flow [24],

$$\overline{Nu}_L = 0.664 \text{Re}_L^{0.5} \text{Pr}^{0.33}, \text{Pr} \geq 0.6 \quad (8)$$

$$\text{Pr} = \frac{\nu}{\alpha} = \frac{\mu C_p}{K} \quad (9)$$

C_p and K for argon at 750 K are 520.5 J/kg K and 0.0353 W/m K respectively, giving a Prandtl number of 0.6561. Hence, the Nusselt number becomes,

$$\overline{Nu}_L = 0.664(28,100)^{0.5} (0.6561)^{0.33} = 93.8$$

The heat transfer coefficient, h , is now calculated as:

$$h = \frac{\overline{Nu}_L K}{L} = \frac{(93.8)(0.0353)}{0.0254} = 130.35 \frac{\text{W}}{\text{m}^2 \text{K}} \quad (10)$$

6.3.2 Energy Input Sub-model

Duration of laser irradiation τ for a line beam of $L_b \times W_b$ is,

$$\tau = \frac{L_b}{V_s} \quad (11)$$

where L_b is the length of focused beam, W_b the width and V_s is the beam speed

For $L_b = 1 \text{ mm}$, $V_s = 254 \text{ mm/sec}$, $\tau = \frac{L_b}{V_s} = \frac{1 \text{ mm}}{254 \frac{\text{mm}}{\text{s}}} = 0.0039 \text{ s}$

Next step is to find out the power absorbed by the powder bed surface, P' which is related to the beam power, P , as follows [32].

$$P' = \chi P - \varepsilon \sigma (T_s^4 - T_A^4) \quad (12)$$

Neglecting radiation losses (second term on the right side of equation (12)), and based on gray body approximation wherein emissivity of a body is equal to its absorptivity, we obtain,

$$P' = \varepsilon P \quad (13)$$

Emissivity of the powder bed can be derived from the following equation [32]:

$$\varepsilon = A_H \varepsilon_H + (1 - A_H) \varepsilon_s \quad (14)$$

where A_H is the area fraction of the surface that is occupied by the radiation-emitting holes, ε_H is the emissivity of the hole and ε_s is the emissivity of the solid particle (nanocrystalline diamond).

For the CO_2 laser (infrared) emitting a laser beam at a wavelength of $10.6 \text{ }\mu\text{m}$, the reflectance, R of a diamond particle surface is 0.1668 [33]. Assuming that the rest is absorbed, the solid emissivity ε_s becomes 0.8332. A_H is based on the porosity parameter φ and is given as [32],

$$A_H = \frac{0.908\varphi^2}{1.908\varphi^2 - 2\varphi + 1} \text{ and for a } \varphi \text{ of } 0.55, A_H = 0.5756$$

Emissivity of the hole, ε_H is dependent on ε_s and φ by the following equation [32],

$$\varepsilon_H = \frac{\varepsilon_s \left[2 + 3.082 \left(\frac{1-\varphi}{\varphi} \right)^2 \right]}{\varepsilon_s \left[1 + 3.082 \left(\frac{1-\varphi}{\varphi} \right)^2 \right] + 1} = 0.953$$

$$\varepsilon = A_H \varepsilon_H + (1 - A_H) \varepsilon_s = 0.9022$$

For incident laser power of 200 W and emissivity of 0.9022, the power absorbed by the powder bed surface, P' , is, 180.44 W.

Power density (or the heat flux) is given as power over the spot area. For a rectangular beam of length and width 1mm by 0.1 mm, $A = 1 * 0.1 = 0.1mm^2$, Power = 180.44 W,

$$\text{Power density} = \frac{180.44W}{0.1mm^2} = 1804.4 * 10^6 \frac{W}{m^2}$$

6.3.3 Heat transfer Sub-model

The first law of thermodynamics states that thermal energy is conserved. For a differential control volume associated with laser beam melting of diamond powder, heat transfer problem can be mathematically described as [24]:

$$\rho C_p \frac{\partial T}{\partial t} = \nabla(K \nabla T) + g(x, y, z, t) \quad (15)$$

The term on the left represents energy storage, the first term on the right provides the three-dimensional heat conduction and the second term on the right corresponds to the internal heat generation, which in this case is zero. ρ is the temperature-dependent density; C_p the specific heat; T the temperature; t the time and ∇ represents the divergence operator.

Since the material is assumed to be homogeneous, $K_x = K_y = K_z = K$. Combining equations we have:

$$\rho(T)C_p(T)\frac{\partial T}{\partial t} = \frac{\partial}{\partial x}\left(K(T)\frac{\partial T}{\partial x}\right) + \frac{\partial}{\partial y}\left(K(T)\frac{\partial T}{\partial y}\right) + \frac{\partial}{\partial z}\left(K(T)\frac{\partial T}{\partial z}\right) \quad (16)$$

Figure 6.2 depicts a three-dimensional representation of the model. In this work, we have considered only one-dimensional equation as it is deemed adequate for the purpose intended, namely determining both steady state and transient temperature profiles as a function of depth that result from the moving heat source by the raster scan of laser beam.

One-Dimensional, Steady-State Formulation: In the steady state case the heat conduction equation becomes,

$$\frac{\partial}{\partial z}\left(K(T)\frac{\partial T}{\partial z}\right) = 0 \quad (17)$$

The boundary conditions are,

$$-K\frac{\partial T}{\partial z}\Big|_{z=0} = 0, \text{ neglecting both convection and radiation}$$

$$-K\frac{\partial T}{\partial z}\Big|_{z=z_B} = 0$$

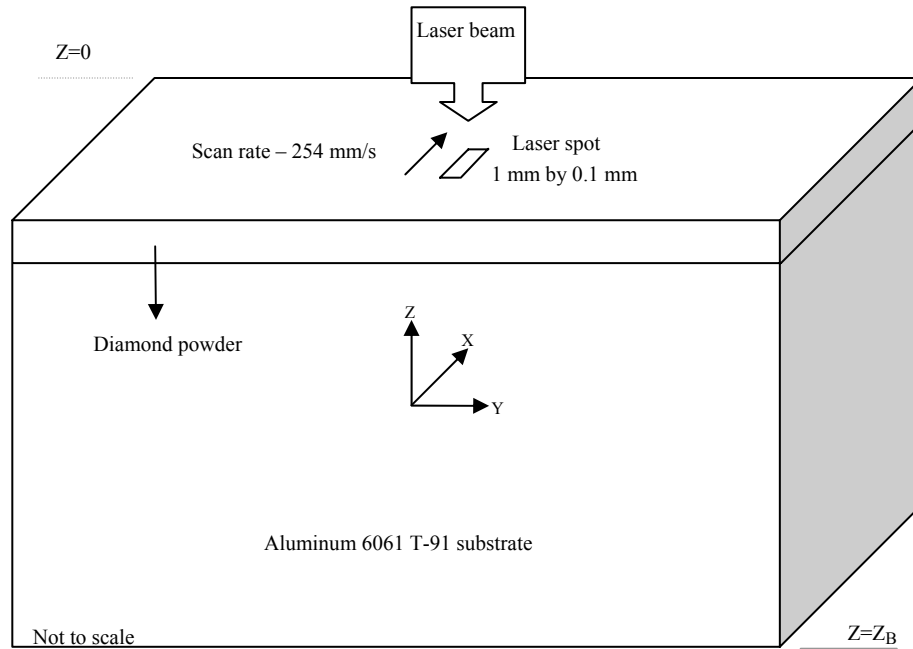


Figure 6.2 Three-dimensional representations of the thermal model.

One-Dimensional, Transient Formulation: In one-dimension transient condition, the heat diffusion equation (16) reduces to,

$$\rho(T)C_p(T)\frac{\partial T}{\partial t} = \frac{\partial}{\partial z}\left(K(T)\frac{\partial T}{\partial z}\right) \quad (18)$$

Following boundary conditions are applied:

Case 1: Convection is considered but radiation is neglected

$$-K\frac{\partial T}{\partial z}\Big|_{z=0} = h(T_{z=0} - T_{env}) \quad (19)$$

where h is the convection coefficient of argon and T_{env} is the ambient temperature.

Case 2: Both convection and radiation are neglected

$$-K\frac{\partial T}{\partial z}\Big|_{z=0} = 0 \quad (20)$$

For both cases, no heat is assumed to be lost at the bottom of the aluminum substrate of thickness z_B and hence,

$$-K \frac{\partial T}{\partial z} \Big|_{z=z_B} = 0 \quad (21)$$

The following initial condition is also applied to recognize the existence of uniform temperature, T_0 , throughout the powder bed prior to the laser sintering process,

$$T(z, 0) = T_0 \quad (22)$$

Thermal conductivity K and specific heat C_p are temperature-dependent properties in the powder bed and hence Tables 6.2 and 6.3 are used to solve the non-linear heat conduction equation.

6.3.4 Finite Element Solution Procedures

Solving the heat transport equations along with material properties in ANSYS code yields the time-dependent temperature distribution throughout the powder bed. One-dimensional conduction elements called “link 32” were used for conduction between nodes, and convection element called “link 34” was used for simulating the convective heat transfer between the top of the coating and the argon shield gas. The material properties of nanocrystalline diamond powder and aluminum 6061 T-91 were used. The aluminum alloy substrate of 0.009525 m long was represented by 10 elements (10 nodes), each element being 0.0009525 m long. The 25 μm thick electrostatic spray sintered diamond nanopowder coating on the aluminum alloy substrate was represented by 5 elements, each 5 μm long. There was a common node at the interface. The spot size area of 0.1 mm^2 was incorporated

as a real constant. The bottom of the substrate was assumed to be at a room temperature of 300 K with no heat loss (fully insulated). Particulars of loading the heat flux were different for steady state and transient analyses and are listed in Tables 6.4 and 6.5 respectively. The following assumptions were made.

- Effects of radiation are negligible and hence ignored
- Material properties are assumed constant wherever its dependence on time is not available
- Laser beam transmission, deflection and scattering losses are ignored
- Laser beam energy is assumed uniform over the spot size and normal to the surface
- Absorbed laser energy is converted to thermal energy instantaneously
- Losses due to ablation of the sample surface, if any, are ignored
- Room temperature is assumed to be 300 K

Table 6.4 Load Settings used in ANSYS for the steady state analysis.

Heat flux (W/m ²)*10 ⁶	1804.4
Interaction time (s)	0.0039
Time at the end of load step (s)	0.0039
Time step size (s)	0.00039
Initial temperature (K)	300
Automatic time stepping	On
Use previous size	Yes

Table 6.5 Load Settings used in ANSYS for the transient state analysis.

H, Heat flux (W/m ²)*10 ⁶	1804.4
Interaction time (s)	0.0039
Cooling time (without convection) (s)	0.0039
Cooling time (with convection) (s)	0.017
Load, Time at the end of load step 1 (s)	0,0
Load, Time at the end of load step 2 (s)	H, 0.00001
Load, Time at the end of load step 3 (s)	H, 0.0013
Load, Time at the end of load step 4 (s)	H, 0.0026
Load, Time at the end of load step 5 (s)	H, 0.0039
Load, Time at the end of load step 6 (s)	0, 0.00391
Load, Time henceforth (s)	0, increments of 0.0013
Step size increments	10
Load type	Step
Initial temperature (K)	300
Automatic time stepping	On
Use previous size	Yes

6.4 Results and Discussion

6.4.1 One-dimensional steady state results

Laser sintering is not a steady state process. In this analysis, there is no dependence of temperature on time or thermal diffusivity. The effects of change in density, thermal conductivity and specific heat of the powder bed along with the phase transition to DLC are not accounted for in this model. Despite all these deficiencies, the steady state analysis is capable of providing a quick estimate of temperature distributions, DLC formation and coating depth. Figures 6.3 and 6.4 shows the temperature-depth profile obtained in this work.

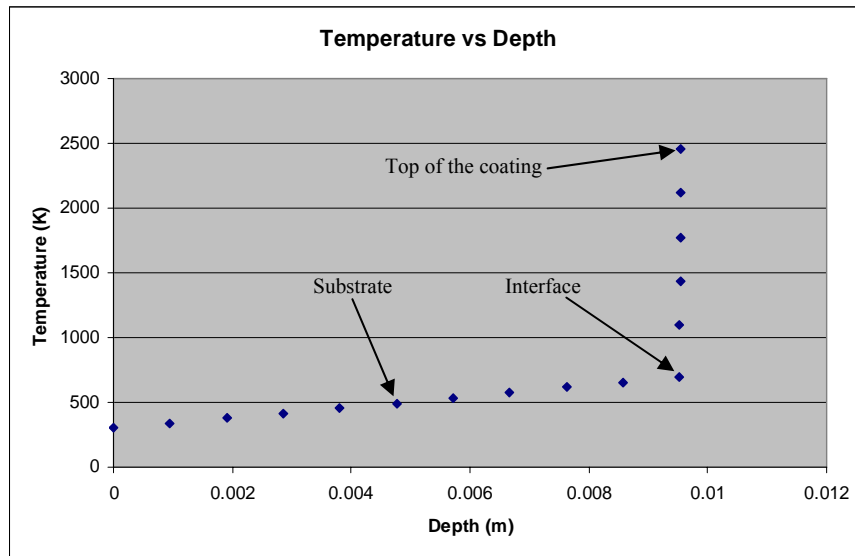


Figure 6.3 Temperature versus depth profile for a one-dimensional steady state analysis (0.0039 s).

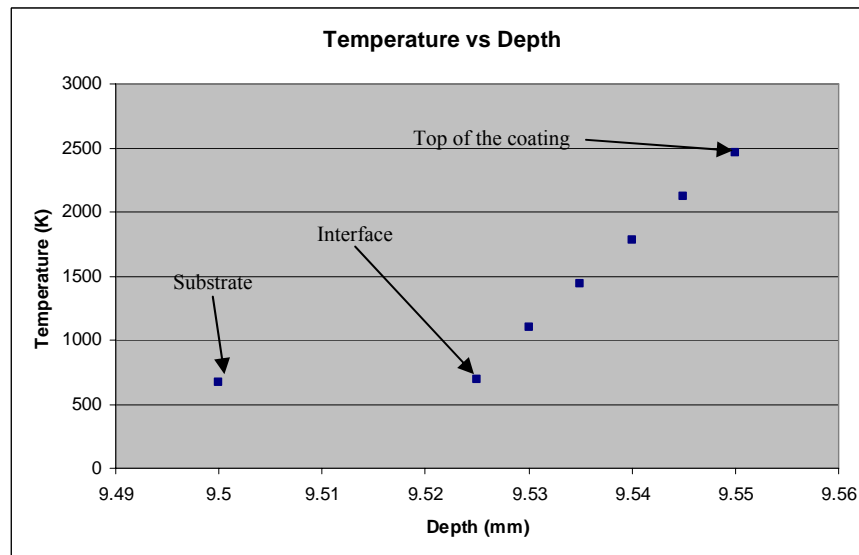


Figure 6.4 Temperature versus depth profile for the steady state analysis, from just below the interface to the top of the coating (0.0039 s).

The temperature at the top surface of the coating is about 2450 K and average temperature of about 1500 K can be seen within the coating depth. The phase transition of diamond to DLC

usually occurs in this temperature range for micropowders (lower for nanopowders). For example, studies of the high-temperature transformation of diamond to graphite performed on micro-sized diamond powders in vacuum revealed that specimens which were heated below 1500 K remained as diamond while those which had been heated to above 1500 K but below 2300 K transformed into a mixture of diamond, DLC and graphite [34, 35].

At normal pressures, diamond is thermodynamically unstable form of carbon and at high temperatures, diamond transforms to other forms of carbon. Based on the traditional phase diagram of carbon, the general expression of the fraction of diamond to transform to graphite, f_g , as a function of temperature and pressure is given by [36]:

$$f_g = \exp\left[-\left(\frac{E_a}{RT}\right)\right] - \exp\left[\frac{-(E_a - \Delta G_{T,P}^g)}{RT}\right] \quad (23)$$

$$\Delta G_{T,P}^g = 1.77 * 10^{-6} (2.73 * 10^6 T + 7.23 * 10^8 - P) \quad (24)$$

Where E_a is the activation energy equal to 120 kJ/mole, R is the gas constant 8.31 J/mole K and P is the pressure in Pa. Application of this equation in the present study (P = 100,000 Pa, T = 1500 K) yields $f_g = 0$. However, the particle size dependence is not shown in these expressions. Figure 6.5 shows the phase diagram of ultra-fine carbon [37] where the particle size is assumed to be 100 nm in the horizontal plane. This diagram illustrates that the diamond is more thermodynamically stable than graphite particularly when the particle sizes are less than 3 nm. Thus, it is inferred that the use of diamond nanopowders can minimize the phase transition to graphite at high-temperatures.

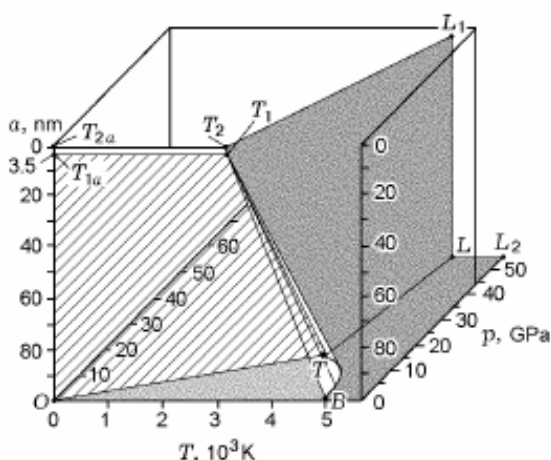


Figure 6.5 Phase diagram of ultrafine carbon [37]: $OBTT_1T_{1a}$ is the existence domain of the graphite phase, OTT_1T_{1a} is the interface between the graphite and diamond phases, BTT_1 is the interface between the liquid carbon and graphite phases, and TT_2L_1L is the interface between the liquid carbon and diamond phases.

The issue of phase transition from nanocrystalline diamond to DLC warrants explanation. There are three means by which crystalline diamond can be transformed into amorphous carbon: 1) Melting and rapid quenching of diamond crystals - Lee *et al.* [38] used molecular dynamics simulations to demonstrate the formation of amorphous structure of carbon by rapid quenching of the melted diamond lattice from 10,000 K at various cooling rates from 1.25×10^{15} K/s to 6.25×10^{15} K/s. This method of phase transition is unlikely in the present work because both temperatures and cooling rates obtained are much lower; 2) Ion beam irradiation - Reinke *et al.* [39] studied the effects of ion irradiation on the surface structure of polycrystalline diamond using photoelectron spectroscopy and found that a gradual change from diamond to amorphous carbon occurred for certain ion doses. The tendency of diamond surface to amorphize rather than graphitize under ion irradiation is essentially to do with the type defect structures generated. This type of mechanism is again ruled out in our present work because the laser beam does not exert momentum as much as ions; 3) Annealing –

Nistor *et al.* [40] subjected polycrystalline diamond to furnace annealing in vacuum at temperatures of 1623–1723 K and then examined the changes by optical absorption, Raman spectroscopy, transmission electron microscopy and electron energy loss spectroscopy. The formation of amorphous carbon and/or of well-crystallized graphite layers was observed along grain boundaries. The diamond-to-graphite transition occurred in such a way that three (111) diamond planes transform into two (0002) graphitic sheets. This type of mechanism is probable in our work where the temperatures are quite similar. However, rapid heating and cooling associated with laser sintering caused diamond transformation to DLC rather than graphite. Furthermore, the fact that phase transition takes place at the grain boundaries during annealing implies that nanoparticles would provide large number of sites for the formation of amorphous carbon.

Another interesting observation in the temperature plot (Figures 6.3 and 6.4) is the interface temperature of 700 K, which is close to the melting point of aluminum 6061 T-91 (855 K). The sintering process is culminated when the aluminum alloy starts melting at 855 K along the interface and diffuses into the lower part of the sintered coating.

6.4.2 One-dimensional transient state results

The laser energy is distributed as near Gaussian according to the laser manufacturer specification. However due to multiple scattering of powder particles in the bed, it is assumed that the laser power is uniform along the spot size and remains constant throughout the laser-material interaction time. The temperature profiles along the depth with and without convection are shown in Figures 6.6 and 6.7. Convective heat transfer by argon gas has an

insignificant effect. The temperature at the top node representing DLC layer is reduced only by 1.23% while it is even less (0.003%) at a node representing the surface just below the substrate-alloy interface.

Both steady state and transient analyses exhibit the same slopes of the 'substrate' and the 'coating' parts of the plots. However, the primary difference is the actual temperature predictions. In the transient analysis, the top surface exhibits a temperature of 1275 K and 1258 K without and with convection respectively as opposed to 2450 K in the steady state. The transient analysis also predicts much lower temperatures at the coating-substrate interface. This substantial reduction in temperatures compared to the steady state is explained below.

Since each section of the powder bed collapses through densification as it reaches its sintering temperature, there is a subsequent reduction in the depth of the coating and an increase in density and thermal conductivity. There is also the formation of DLC phase which could change some of the assumed properties of the diamond nanopowders. In FEM, it is assumed that the powder bed is remaining with the same thickness until the end of laser beam passage. But in reality, the powder bed is compacted from 25 μm to 10 μm during laser processing. This reduction in 16 μm is not accounted for in the FEM solution.

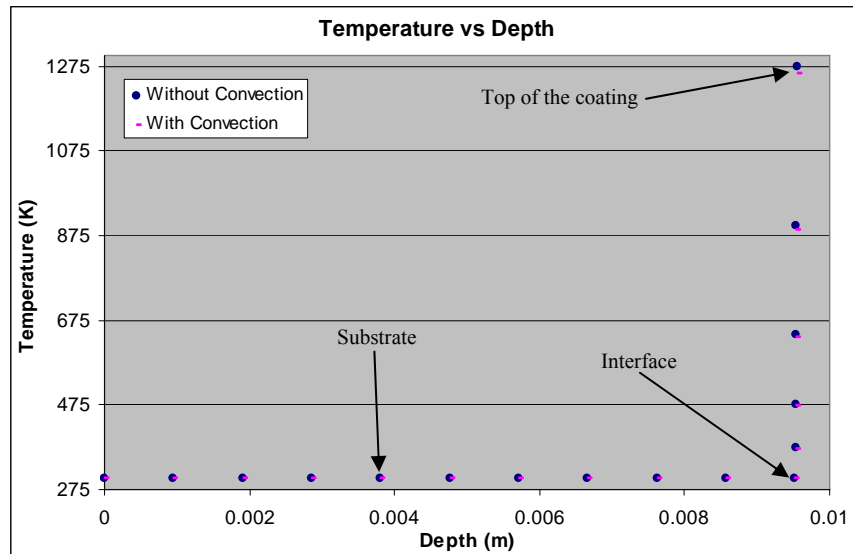


Figure 6.6 Temperature versus depth profile for the transient analysis (0.0039 s).

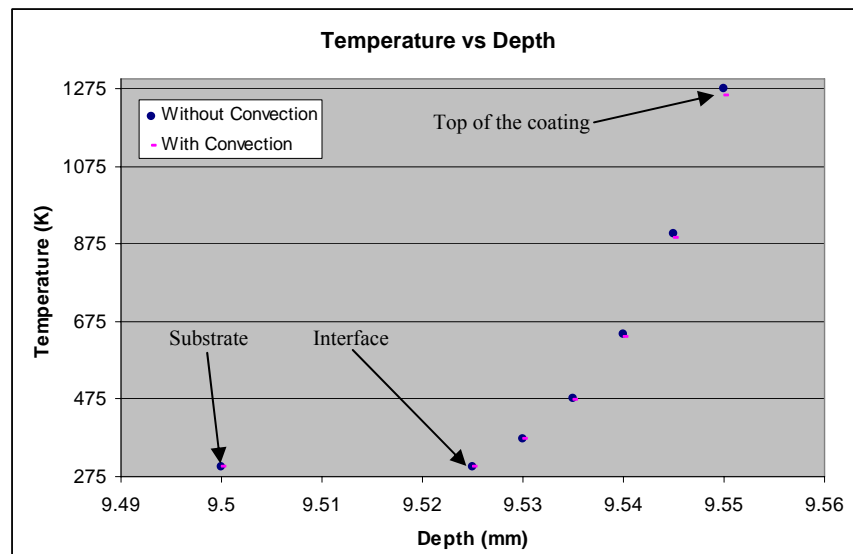


Figure 6.7 Temperature versus depth profile for the transient analysis, from just below the interface to the top of the coating (0.0039 s).

Cooling curves for the ‘convection-free’ and ‘with convection’ analyses are shown in Figures 6.8 and 6.9. As expected, the top surface reaches much higher temperatures compared to the middle, interface and substrate. Even after the heat flux is removed at 0.0039 s, it can be seen that the temperature continues to rise till about 0.006 s for the middle of the coating and then

decreases. This is also true for the interface and for a portion just below the interface although the magnitudes are very small. For the forced convection model, the temperatures are slightly lower compared to the convection ‘free’ model.

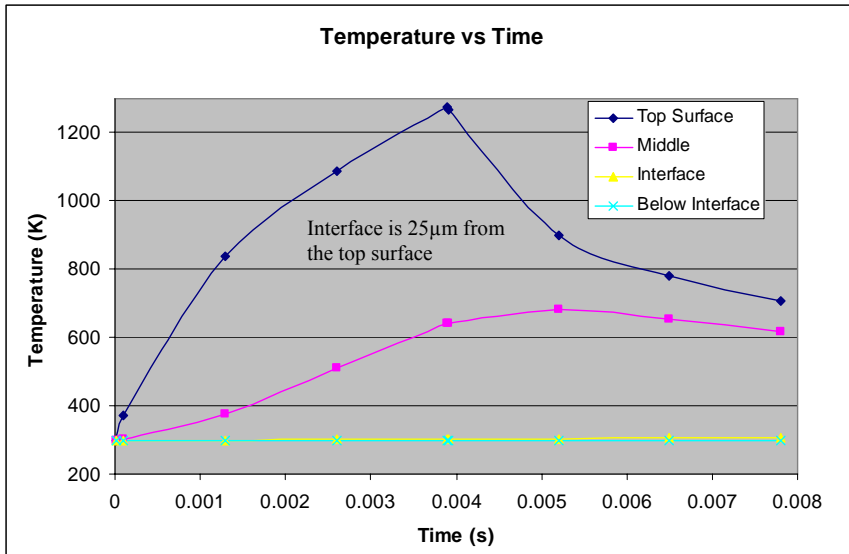


Figure 6.8 Temperature versus time curve for a transient ‘convection free’ model.

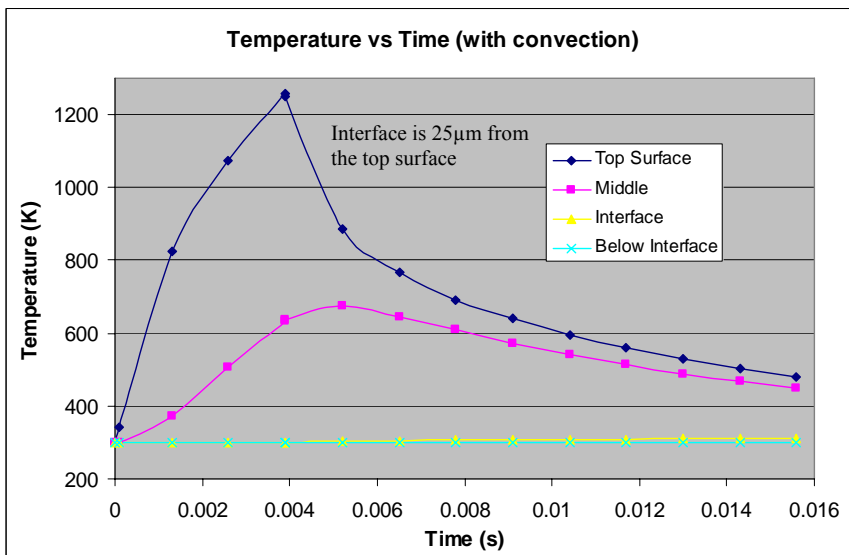


Figure 6.9 Temperature versus time curve for forced convection transient model.

Both experimental data and transient heat transfer analysis offer evidence for postulating the following hypothesis: During the first three-fourth of the interaction time of the beam with powder bed, adequate temperatures have reached for initiation of nanoparticle sintering and densification of powders to take place followed by phase transition from diamond powder to DLC. The depth of coating is reduced to 10 μm from 25 μm . Density of the powder bed increases as material flow into voids, causing a decrease in overall volume. Mass transfer occurs during this phase that reduces the total porosity by repacking, followed by material transport due to diffusion. Atoms move along crystal boundaries to the walls of internal pores, redistributing mass from the internal bulk of the object and smoothing pore walls. Surface tension is the driving force for this movement. In the final one-fourth of time, melting and overaging of aluminum alloy takes place at and below the interface. The conversion of diamond nanopowder into amorphous carbon form occurs around 940 K [41] at ambient pressure in fast pace due to large surface area of nanoparticles and non-equilibrium nature of laser sintering.

To partially support this hypothesis, a revised transient analysis (with convection) is carried out with the following assumptions. Since it is known that the final thickness of the coating is 10 μm and we believe that it occurred after $\frac{3}{4}$ th of the beam interaction time, the model is revised wherein the temperatures at the top three nodes in the transient model after 75% of the laser interaction time are chosen as the initial conditions. The coating thickness of 10 μm is represented by 2 elements each 5 μm long having thermal properties of tetrahedral amorphous carbon (ta-C) which is one of the forms of DLC [42]. The rationale behind making such an assumption is because the powder bed collapses in the laser sintering process

and the temperature in the interface is seen to be high enough to melt the substrate-coating interface. Heat is supplied for the remaining 25% of the laser interaction time and the final temperatures obtained match closely to that observed in the experiment as shown in the figure below. The substrate-coating interface temperature obtained is just below melting temperature of the aluminum alloy. At 80 μm below the substrate-coating interface is the heat affected zone (HAZ)-substrate interface where the temperature is close to 430 K. The average temperature in the HAZ is large enough to support the possibility that overaging process can occur in this zone.

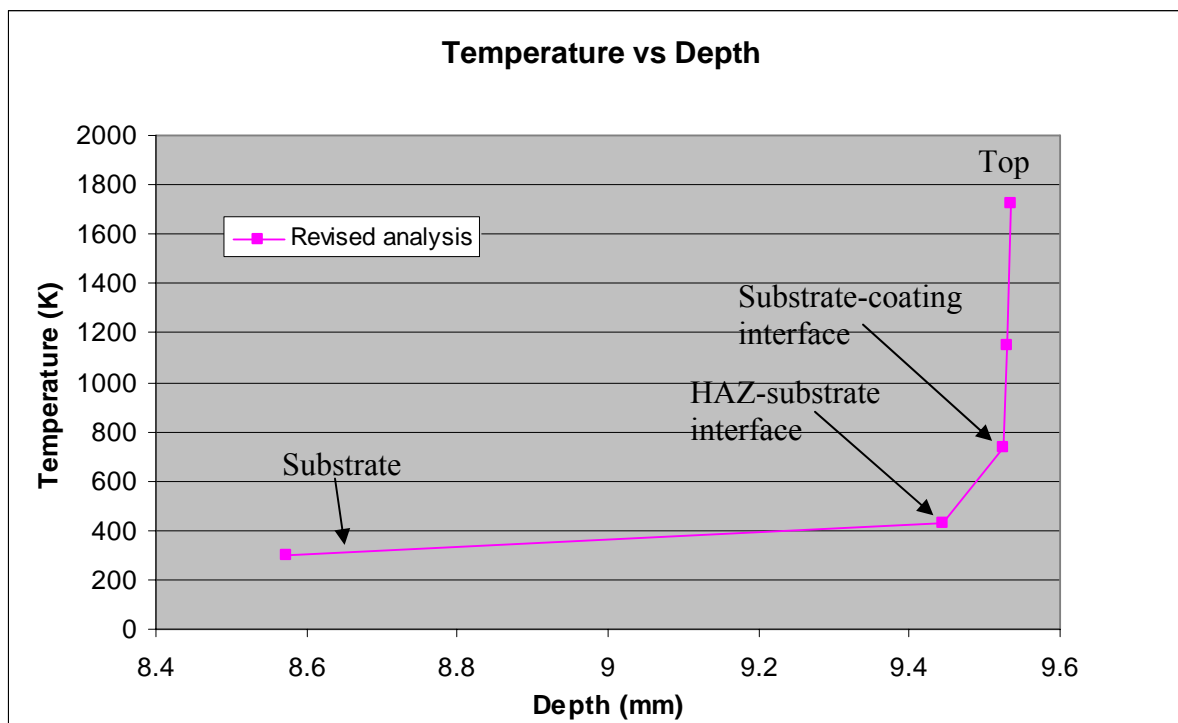


Figure 6.10 Temperature versus depth plot after the revised analysis (0.0039 s).

6.4.3 Stress calculations

Based on these stresses obtained and taking 735 K (interface temperature at the end of the laser beam interaction) as the stress free temperature, a thermal stress versus depth plot can be drawn, where it is seen that the 10 μm coating above the substrate exists in tension, while the substrate exists in compression. Thermal expansion coefficient and Young's modulus of DLC [43, 44] are used for calculating the stresses in the coating and that of aluminum 6061 T-91 [29] for the substrate.

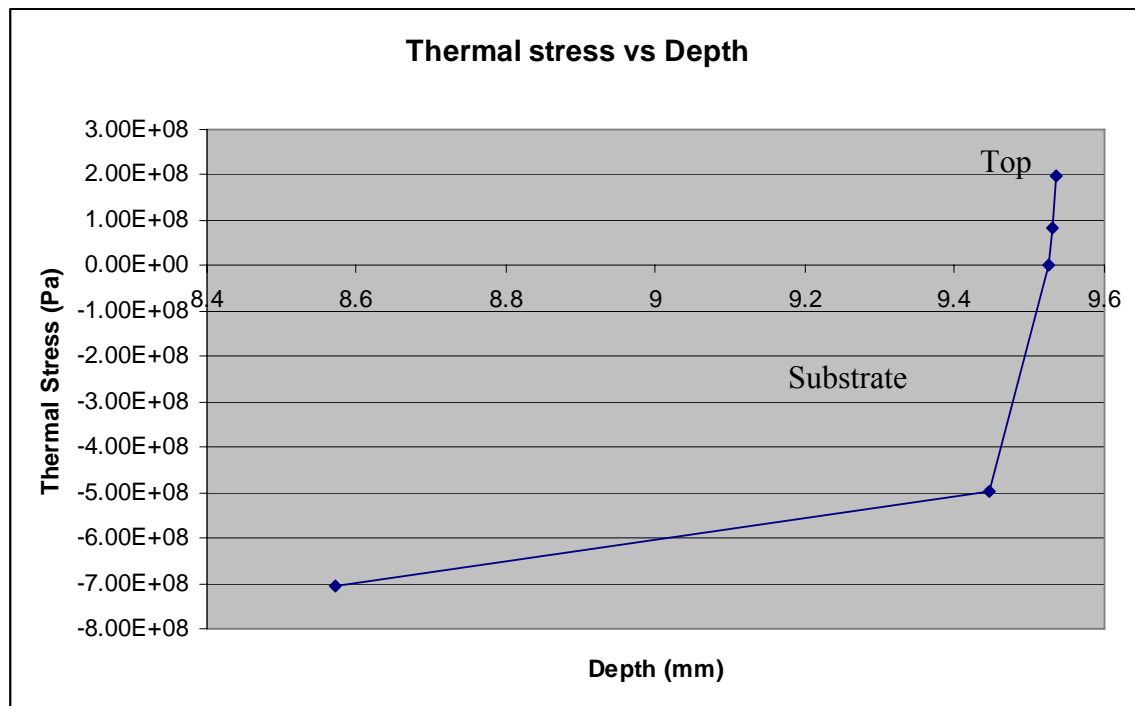


Figure 6.11 Thermal stresses developed above and below the coating-substrate interface after heating (based on the revised analysis).

The tensile stresses above the interface have a maximum value of 0.2 GPa which is well below the yield strength of DLC (varies between 5 and 9 GPa) [45]; this shows that the thermal stresses are small and hence cracks are non-existent or minimal.

The interface thermal stress values after the coating has cooled down to 300 K, were computed based on the differences in thermal expansion coefficients. Since the thermal expansion coefficient of DLC ($1 \cdot 10^{-6}/\text{K}$) is lower than aluminum 6061 T-91 ($23.6 \cdot 10^{-6}/\text{K}$), the thermal expansion mismatch will result in the formation of tensile stresses in the coating during cooling down. Magnitude of tensile stresses in the coating can be estimated from the following equation where the Young's modulus of DLC is 200 GPa.

$$\sigma = E_{DLC} (\beta_{DLC} - \beta_{Al}) (T - T_f) \quad (25)$$

Considering interface stress free temperature (T_f) as 735 K (from the revised analysis), there are compressive stresses created below the interface and tensile stresses above it. These tensile stresses can cause delamination of the coating if it exceeds that of the strength of diamond. Calculations show that at ambient temperature (300 K), the residual tensile stresses in the coating will be 1.96 GPa which are substantially lower than the yield strength of DLC.

6.5 Conclusions

Laser sintering of nanocrystalline diamond powders is an ultra-fast, non-equilibrium process that provides a unique opportunity to produce fairly thick DLC coatings without any graphite impurity at low substrate temperature. This technique is indeed very efficient when compared against the traditional chemical vapor deposition (CVD) technique, which is deemed as tedious and time-consuming operation. Finite element analysis of thermal energy transport provided the temperature distributions and inferred that sintering takes place at substantially lower temperatures (solid state).

Acknowledgements

The authors would specially like to thank Dr. Pranav Shrotriya for his help and advice. Thanks are also in part due to Dr. Wenping Jiang, Dr. Warren Straszheim, Mr. Hal Sailsbury and Mr. Scott Schlorholtz.

References

1. Jacobs, P. F. (1992). *Rapid Prototyping & Manufacturing: Fundamentals of Sterolithography*, Society of Manufacturing Engineers.
2. Bugada, G., Cervera, M. and Lombera, G. (1999). Numerical prediction of temperature and density distribution in selective laser sintering process. *Rapid Prototyping Journal*, Vol. 5, No. 1, pp. 21-26.
3. Childs, T. H. C. and Tontowi, A. E. (2001). Selective laser sintering of a crystalline and glass-filled crystalline polymer: Experiments and simulations. *Proc. Inst. Mech. Engrs*, Vol. 215, No. B, pp. 1481-1495.
4. Agarwala, M., Bourell, D., Beaman, J., Marcus, H. and Barlow, J. (1995). Direct selective laser sintering of metals. *Rapid Prototyping Journal*, Vol. 1, No. 1, pp. 26-36.
5. Zhang, Y. W. and Faghri, A. (1998). Melting of a subcooled mixed powder bed with constant heat fluxing. *International Journal of Heat and Mass Transfer*, Vol. 42, pp. 775-788.
6. Van der Schueren, B. and Kruth, J. P. (1995). Powder deposition in selective metal powder sintering. *Rapid Prototyping Journal*, Vol. 1, No. 3, pp. 23-31.
7. Macedo, Z. S. and Hernandez, A. C. (2002). Laser sintering of $\text{Bi}_4\text{Ti}_3\text{O}_{12}$ ferroelectric ceramics. *Materials Letters*, Vol. 55, No. 4, pp. 217-220.

8. Danilenko, V. V. (2005). Phase diagram of nanocarbon. *Combustion, Explosion and Shock Waves*, Vol. 41, No. 4, pp. 460-466.
9. Zhu, H. and Averback, R. S. (1996). Sintering Processes of two nanoparticles: a study by molecular-dynamics simulations. *Philosophical Magazine Letters*, Vol. 73, No. 1, pp. 27-33.
10. Arato, P., Bartha, L., Porat, R., Berger, S. and Rosen, A. (1998). Solid or liquid phase sintering of nanocrystalline WC/Co hardmetals. *Nanostructured Materials*, Vol. 10, No. 2, pp. 245-255.
11. Friedman, T. A., Sullivan, J. P., Knapp, J. A., Tallant, D. R., Follstaedt, D. M., Medlin D. L. and Mirkarimi, P. B. (1997). Thick stress-free amorphous-tetrahedral carbon films with hardness near that of diamond. *Applied Physics Letters*, Vol. 71, No. 26, pp. 3820 – 3822.
12. Liu, E., Blanpain, B., Shi, X., Celis, J. P., Tan, H. S., Tay, B. K., Cheah, L. K. and Roos, J. R. (1998). Tribological behavior of different diamond-like carbon materials. *Surface and Coatings Technology*, Vol. 106, pp. 72-80.
13. Liu, E., Shi, X., Tay, K., Cheah, L. K., Tan, H. S., Shi, J. R. and Sun, Z. (1999). Micro-Raman spectroscopic analysis of tetrahedral amorphous carbon films deposited under varying conditions. *Journal of Applied Physics*, Vol. 86, No. 11, pp. 6078-6083.
14. Liu, E., Gao, J. X, Zeng, A. P., Tay, B. K. and Shi, X. (2002). Tribological behavior of nanocomposite diamondlike carbon-aluminum films. *Material Research Society Symposium Proceedings*, Vol. 695, pp. 231-236.

15. Dimigen, H., Hubsch, H. and Memming, R. (1987). Tribological and electrical properties of metal-containing hydrogenated carbon films. *Applied Physics Letters*, Vol. 50, No. 16, pp. 1056-1058.
16. Chen, J., Deng, S. Z., Chen, J., Yu, Z. X. and Xu, N. S (1999). Graphitization of nanodiamond powder annealed in argon ambient. *Applied Physics Letters*, Vol. 74, No. 24, pp. 3651-3653.
17. Dabby, F. W. and Paek, U. C. (1972). High-intense laser-induced vaporization and explosion of solid material. *IEEE Journal of Quantum Electronics*, Vol. 8, No. 2, pp. 106-111.
18. Noguchi, S., Ohmura, E. and Miyamoto, I. (2003). Analysis on resin removal in laser drilling of printed circuit board. *Proceedings of the International Society for Optical Engineering (SPIE)*, Vol. 4830, pp. 46-51.
19. Mazhukin, V. I., Smurov, I. and Flamant, G. (1995). Overheated metastable states in pulsed laser action on ceramics. *Journal of Applied Physics*, Vol. 78, pp. 1259-1270.
20. Vail, N. K., Balasubramanian, B., Barlow, J. W., and Marcus, H. L. (1996). A thermal model of polymer degradation during selective laser sintering of polymer coated ceramic powders. *Rapid Prototyping Journal*, Vol. 2, No. 3, pp. 24-40.
21. German, R. M. (1990). Supersolidus liquid phase sintering. Part II: Densification theory. *International Journal of Powder Metallurgy*, Vol. 26, No. 1, pp. 35-38.
22. Nelson, J. C., Xue, S., Barlow, J. W., Beaman, J. J., Marcus, H. L., and Bourell, D. L. (1993). Model of the selective laser sintering of bisphenol – A polycarbonate. *Ind. Eng. Chem. Res.*, Vol. 32, pp. 2305-2317.

23. Nelson, J. C., Vail, N. K., Barlow, J. W., Beaman, J. J., Bourell, D. L., and Marcus, H. L. (1995). Selective laser sintering of polymer-coated silicon carbide powders. *Ind. Eng. Chem. Res.*, Vol. 34, pp. 1641-1651.
24. Incropera, F. P. and DeWitt, D. P. *Fundamentals of Heat and Mass Transfer*, Fourth Edition, John Wiley & Sons.
25. Yagi, S. and Kunii, D. (1957). Studies in the effective thermal conductivities in packed beds. *American Institute of Chemical Engineering Journal*, Vol. 3, No. 3, pp. 373-381.
26. Touloukian, Y. S. and Ho, C. Y. (1970-1977). Editions -*Thermophysical Properties of Matter, The TPRC Data Series (13 volumes on thermophysical properties: thermal conductivity, specific heat, thermal radiative, thermal diffusivity, and thermal linear expansion)*, Plenum Press, New York.
27. Wilks, J. and Wilks, E. (1991). *Properties and Applications of Diamond*, Butterworth-Heinemann Ltd, Linacre House, Jordan Hill, Oxford OX2 8DP.
28. Pierson, H. O. (1993). *Handbook of Carbon, Graphite, Diamond and Fullerenes*, Noyes Publications, Mill Road, Park Ridge, New Jersey 07656, U.S.A.
29. MatWeb.com, The Online Materials Database. <http://www.matweb.com>, *Properties of Aluminum 6061 T-91*, Retrieved – June, 8th, 2006.
30. Ouyang, J.H., Nowotny, S., Richter, A. and Beyer, E. (2001). Laser cladding of yttria partially stabilized ZrO₂ (YPSZ) ceramic coatings on aluminum alloys. *Ceramics International*, Vol. 27, pp. 15-24.
31. Malaczynski, G., Hamdi, A. H., ElmoursI, A. A. and Qiu, X. (1997). Diamond-like carbon coating for aluminum 390 alloy – automotive applications. *Surface & Coatings Technology*, Vol. 93, pp. 280-286.

32. Sih, S. S. and Barlow, J.W. (2004). The prediction of emissivity and thermal conductivity of powder beds. *Particulate Science and Technology*, Vol. 22, pp. 427-440.
33. Zaitsev, A. M. (2001). *Optical properties of diamond: A data handbook*, Springer, New York, pp. 13-14.
34. Seal, M. (February 20, 1960). Graphitization of Diamond. *Nature*, Vol. 185, pp. 522 – 523.
35. Evans, T. and James, P. F. (Jan. 21, 1964). A Study of the Transformation of Diamond to Graphite. *Proceedings of the Royal Society of London, Series A, Mathematical and Physical Sciences*, Vol. 277, No. 1369, pp. 260-269.
36. Wang J. B. and Yang, G. W. (1999). Phase transformation between diamond and graphite in preparation of diamonds by pulsed-laser induced liquid–solid interface reaction. *Journal of Physics: Condensed Matter*, Vol. 11, No. 37, pp. 7089–7094.
37. Vereshchagin, A. L. (2002). Phase Diagram of Ultrafine Carbon. *Combustion, Explosion, and Shock Waves*, Vol. 38, No. 3, pp. 358-359.
38. Lee, S. H., Lee, S. C., Lee, K. R., Lee, K. H. and Lee, J. G. (2002). Metastable Site in Amorphous Carbon Lattice Generated by Rapid Quenching of Liquid Diamond. *Nanotech, Vol. 2, Technical Proceedings of the 2002 International Conference on Computational Nanoscience and Nanotechnology*, pp. 466 – 469.
39. Reinke, P., Francz, G., Oelhafen, P. and Ullmann, J. (1996). Structural changes in diamond and amorphous carbon induced by low-energy ion irradiation. *Physical Review B*, Vol. 54, No. 10, pp. 7068-7075.
40. Nistor, L., Ralchenko, V., Vlasov, I., Khomich, A., Khmel'nitskii, R., Potapov, P. and Van Landuyt J. (2001). Formation of Amorphous Carbon and Graphite in CVD Diamond

- upon Annealing. *Physica status solidi. A, Applied Research*, Vol. 186, No. 2, pp. 207–214.
41. Qian, J., Pantea, C., Huang, J., Zerda, T. W. and Zhao, Y. (2004). Graphitization of diamond powders of different sizes at high pressure-high temperature. *Carbon*, Vol. 42, pp. 2691-2697.
42. Shamsa, M., Liu, W. L., Balandin, A. A., Casiraghi, C., Milne, W. I. and Ferrari, A. C. (2006). Thermal conductivity of diamond-like carbon films. *Applied Physics Letters*, Vol. 89, No. 161921, pp. 1-3.
43. Schneider, D., Schwarz, T., Scheibe, H. J. and Panzner, M. (1997). Non-destructive evaluation of diamond and diamond-like carbon films by laser induced surface acoustic waves. *This Solid Films*, Vol. 295, No. 1, pp. 107-116.
44. Luo, J. K., He, J. H., Fu, Y. Q., Flewitt, A. J., Spearing, S. M., Fleck, N. A. and Milne, W. I. (2005). Fabrication and characterization of diamond-like carbon/Ni bimorph normally closed microcages. *Journal of Micromechanics and Microengineering*, Vol. 15, pp. 1406-1413.
45. Gan, Z., Zhang, Y., Yu, G., Tan, C. M., Lau, S. P. and Tay, B. K. (2004). Intrinsic mechanical properties of diamond-like carbon thin films deposited by filtered cathodic vacuum arc. *Journal of Applied Physics*, Vol. 95, No. 7, pp. 3509-3515.

CHAPTER 7. General Conclusions and Future Work

Solid freeform fabrication (SFF) is emerging as a potential competitor for subtractive machining processes to make dies and molds. Its role in tooling industries is beginning to change from early proof of concept to currently real tools. However, rough surface, non-uniformity in deposited tracks, and residual stress limit reaching the maturity of this new technology. In this work, we have demonstrated that laser-based flexible fabrication (LBFF) that uses laser beams and quasi co-axial nozzle for powder delivery can improve surface finish, dimensional tolerance, and reduce distortion. LBFF not only offers the flexibility to design functionally graded dies and molds with tailored properties but also provides the feasibility to build up functional tools with geometry such as embedded structures that would be difficult to fabricate in conventional machining methods. Another conclusion is the use of nanoparticles in SFF to enhance the properties of dies and molds leading to their longevity as well as performance.

Hard coatings for light weight aluminum structures are severely limited. The best coating available for aluminum substrates is DLC applied through CVD processes. In this work, we have showed the formation of thick DLC coatings by a fairly simple laser sintering technique. This can have significant impact in automobile and space industries.

The principal results of the thesis are:

1. Nanoparticle-dispersed H13 steel molds have outperformed baseline H13 molds based on various tests that include Rockwell hardness, Vickers microhardness, corrosion test in 10% hydrochloric acid and plastic injection molding tests.
2. LBFF is capable of producing fully dense and functional parts. Functionally graded H13/NiCr/TiC mold insert was superior in resistance to stressed deformation and in dimensional stability at elevated temperature compared to an H13 only mold.
3. Laser sintering on electrostatically deposited nano-diamond powders, produced a near-dense and uniform layer of diamond-like carbon coating on aluminum 6061 T-91 substrate for a laser power of 200 W and scan speed of 254 mm/s. Microhardness of 22.5 GPa obtained for this sample comes under the category of super-hard materials. Fracture toughness values fall within the expected range for a DLC coating. Presence of DLC was confirmed with Raman scattering tests and X-ray diffraction. Scratch tests revealed a critical force for delamination, almost 4 times more than a sample that was not laser sintered.
4. Finite element solutions of steady and transient one-dimensional heat transfer problem revealed that laser sintering of nano-diamond powders begins to occur around 800 K followed by densification and then heating of the interface to nearly the melting temperature of aluminum. Residual stresses are much lower than the yield strength of diamond.

Future work is recommended in the following areas. 1) Accelerated tests of functionally graded inserts for corrosion resistance in static aluminum alloy melt or a thermal fatigue test

by alternatively immersing test sample into molten aluminum and water. Immersion of the insert in melts results in dissolution. Weight loss per unit area can be used as evaluation criteria for this test. Thermal fatigue can be justified by the inception of cracks resulted from cycled loads. 2) The deposition of nano-powder by means of LBFF is an area of interest but agglomeration of nanoparticles remains a concern. 3) Laser sintering of diamond nanopowder on aluminum-carbon fiber composite alloy substrates could produce much better substrate-coating bond. DLC coatings made on these types of substrates using other methods have shown improvement in tribological and mechanical properties. This could be due to the C-C bonds formed between the carbon in the deposition and the carbon in the substrate. 4) A heat transfer model that takes into account the thermo-physical and phase change properties of the diamond nanopowder bed as it collapses and becomes dense, as the laser sintering proceeds, could give a better understanding of the temperatures and stresses involved in this process.

APPENDIX A. Laser-based, Solid Freeform Fabrication Facility

In laser-based SFF process, a geometric CAD model of the part is mathematically sliced into very thin layers, resulting in a series of contours that describe the part boundaries in each layer. The model is then reconstructed one slice at a time by material addition. A thin layer of powder is raster-scanned with a laser beam to sinter the powder in areas to be occupied by the part. Successive layers of the powder are then deposited and sintered until the entire part is complete.

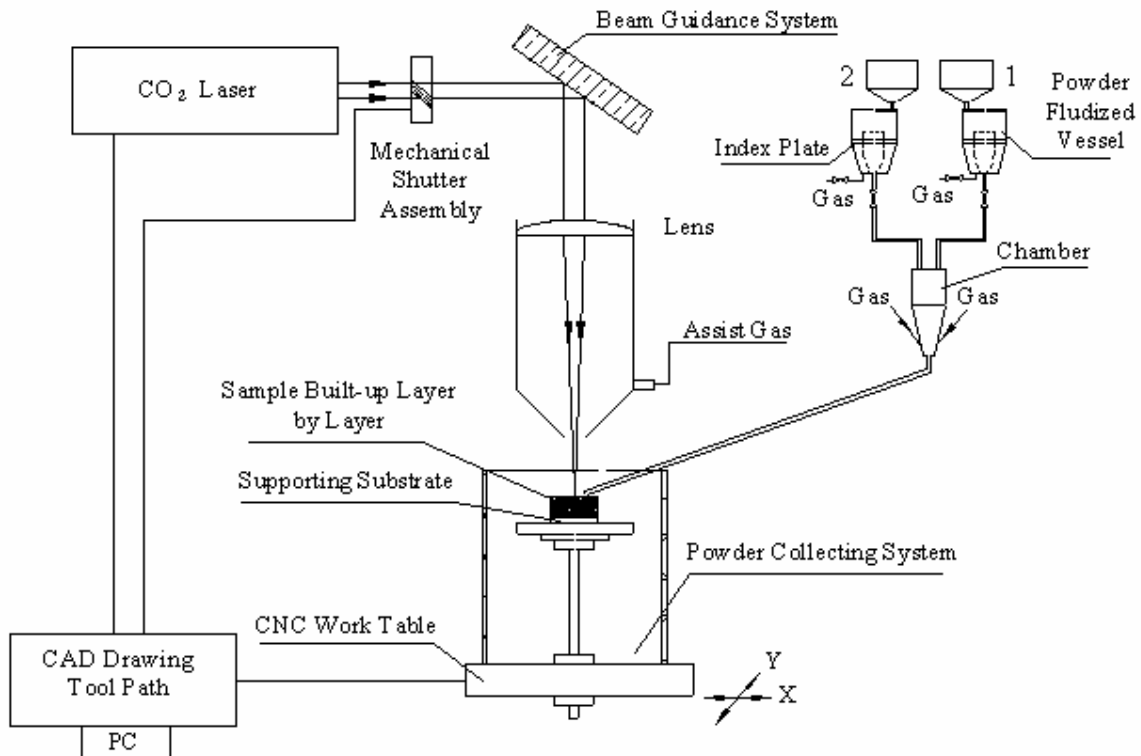


Figure A.1 A schematic of laser-based solid freeform fabrication process

Based on this concept, a multiple material SFF laboratory workstation was designed and built in the Mechanical Engineering department that uses a powder mixing subsystem consisting of two computer controlled screw feeders. The mix composition of powder is determined by controlling the relative flow rates of the two powders (Figure A.1). A motor driven impeller then mixes the powders. The mixing chamber then deposits the powder in a line for roller transferal to the part cylinder. This system has been integrated with a counter-rotating roller and part cylinder, similar to those in the commercial SLS process. Additionally, scanning and optimal control subsystems for a 2000 W CO₂ laser have been developed and tested. The laser experiments are usually performed with shaped beam profiles obtained by an off-axis mirror scanner or by focusing the beam through a cylindrical/spherical lens. A chamber with gas flow and low vacuum purge capabilities has been developed for atmospheric control. With this system, we have successfully fabricated test parts whose composition varies, allowing fabrication of functional gradient materials shown in Chapter 4.

APPENDIX B. Powder delivery system design and powder delivery rate calibration

B.1 Design of powder delivery system

Power delivery system is critical to the success of building parts from laser-based flexible fabrication method. The goals of designing such a system are to transport required amount of powders continuously and uniformly to laser-created molten area. The challenge is the irregular shapes of powder particles that make powder delivery very difficult even with the assistance of excited vibration. Task of powder delivery becomes even tougher with the powder sizes scaled down to nano-scale because 1) nano-sized particles have much higher ratio of surface-to-volume than micro-sized particles, and 2) nano-sized powders' atomic force are comparable to the mass of individual particles. These sharp changes of physical and dynamic properties further impact the balances among the criteria governing particle movement as they are among micro-sized particles. For example, adhesion force plays much more important role in nano-sized powders than it does in micro powders. Given traditional gas powder delivery practice, a system with a venturi was designed (Figure B.1). Pressure gas (argon, helium or nitrogen) is the driving force to move powder particles from venturi to an intended spot. As shown in Figure B.1, powders are driven down from the hopper by gravity, and are collected by "recesses" evenly distributed around the rotator of a metalmeter. The collected powders are dumped to the outlet side as the rotator runs at a preset speed, which is linearly proportional to the powder mass delivery rate. When pressure gas passes through the venturi, it sucks in the powders and delivers them along the path. Tests have shown this powder delivery setup works well for micro-sized powders.

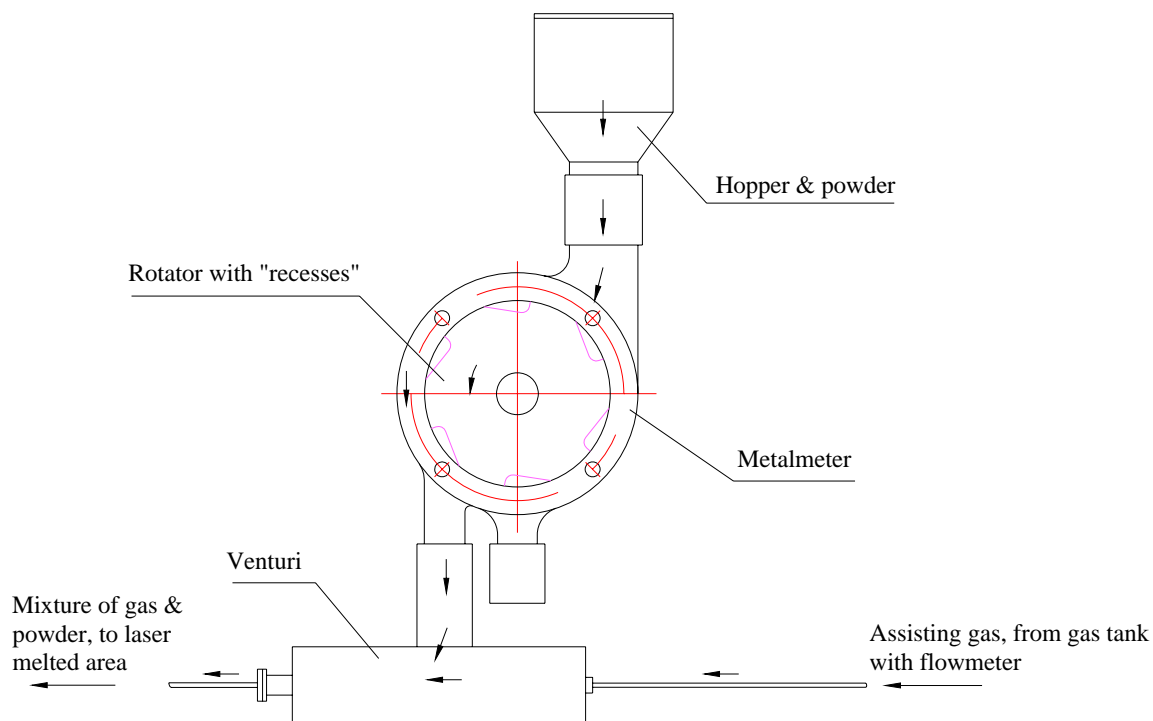


Figure B.1 A schematic showing the design of powder delivery system for laser-based flexible fabrication process.

B.2 Calibration of powder delivery rate

Powder delivery rate, Q , is defined as the total mass passing across a controlled section in unit time. It is usually represented in grams per minute or per second. Quantitative control of the powder delivered to a laser-melted zone is of great significance to ensure quality. Calibration is an effective way to check the uniformity of powder delivery. A block diagram for powder quantification is shown in Figure B.2. A capped glass vessel was used to collect powder. A stopwatch with an accuracy of 1/100 second was used to measure time, t , and a scale with an accuracy of 1/1000 gram to quantify the mass of powder, m , corresponding to the time Δt . At a setting (pressure or flow rate) for assisting gas, adjustment on the reading of metalmeter changes the revolution speed of the rotator, and further the powder delivery rate.

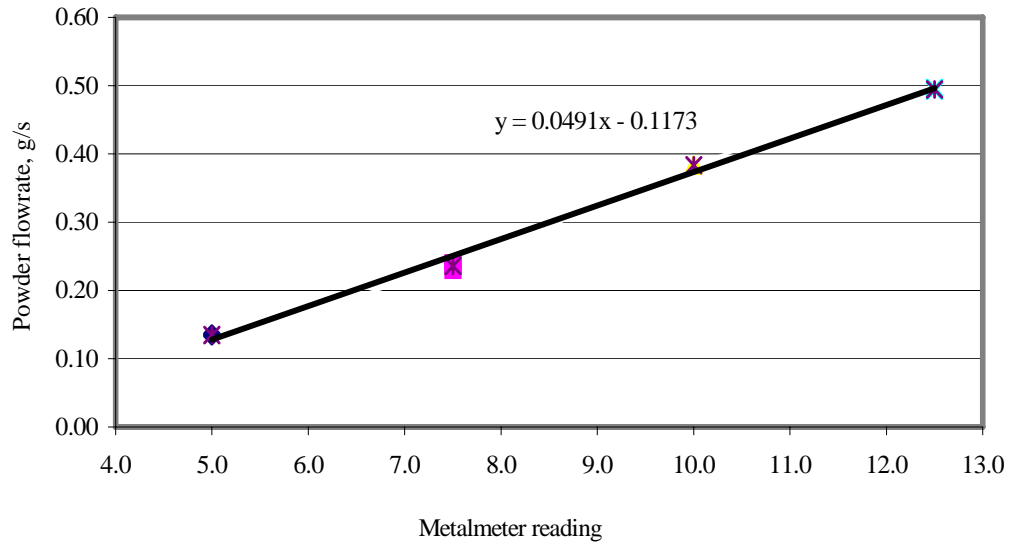


Figure B.3 Calibrated results of H-13 powder. (Assisting gas, argon, at flow rate of 10 CFH)

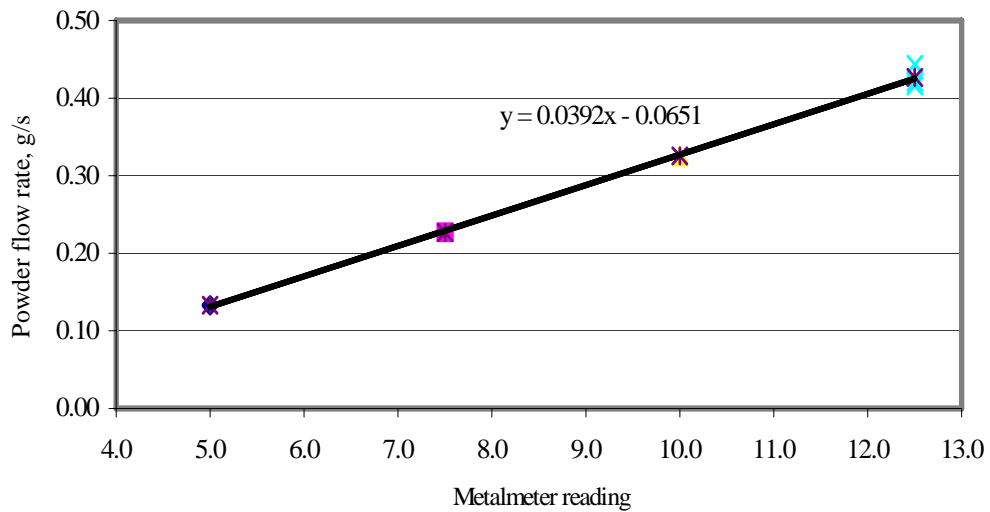


Figure B.4 Calibrated results of Ni-Cr composite powder. (Assisting gas, argon, at flow rate of 10 CFH)

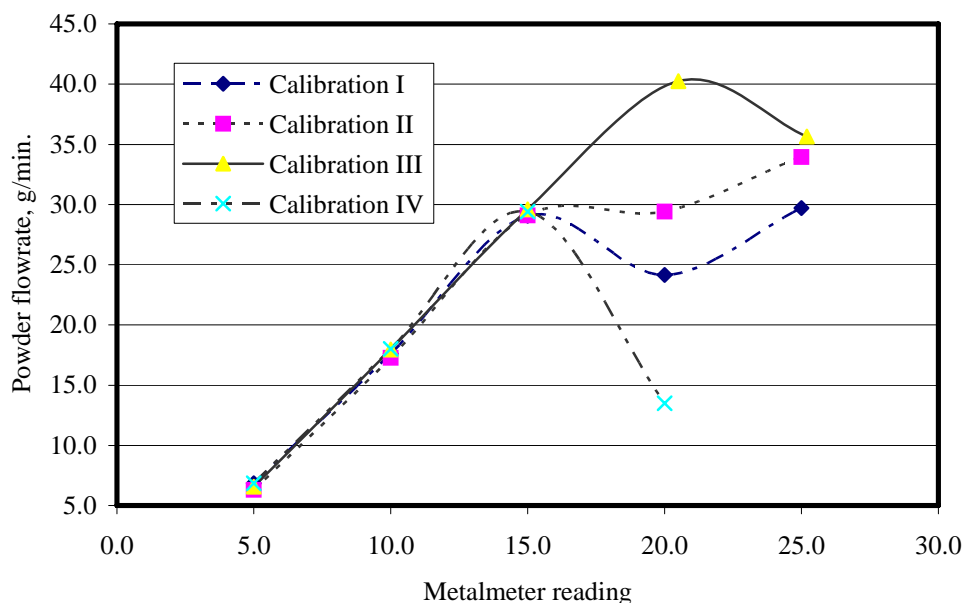


Figure B.5 Calibrated result inconsistency of Ni-Cr composite powder beyond readings 13. (Assisting gas, argon, at flow rate of 10 CFH)

The total uncertainty of powder delivery rate at a 95% confidence level can be estimated as less than 2.5% by use of theory of uncertainty propagation, with both bias and precision errors considered. Take H13 powder calibration corresponding to readings of 7.5 for an example, the estimation of uncertainty based on single-sample is summarized as follows.

The powder mass, m , is measured with a scale. Bias uncertainty depends on the scale calibration, and also to some degree on the magnitude of the mass measured relative the scale range. To this situation, an uncertainty of $\pm 0.5\%$ is justified, with a confidence of 95%. Precision uncertainty in mass measurement is by reading error in the scale and the other factors, and taken as $\pm 0.1\%$.

The time, t , is measured with a stopwatch. Synchronization between the powder delivery and watch actions will be the main uncertainty, which is essentially precision error. If time standard deviation is simply estimated as $\pm 2s$, and a total time period of 200s will be measured, then the standard deviation is $\pm 1\%$. The bias error can be assumed to be negligible.

Applying the uncertainty propagation theory [1], we have:

$$\frac{u_Q}{Q} = \left[\left(\frac{u_m}{m} \right)^2 + \left(\frac{u_t}{t} \right)^2 \right]^{1/2} \quad (\text{A-1})$$

The bias uncertainty is estimated as:

$$\frac{B_Q}{Q} = \left[\left(\frac{B_m}{m} \right)^2 + \left(\frac{B_t}{t} \right)^2 \right]^{1/2} = \left[(0.5)^2 + (0)^2 \right]^{1/2} = 0.50\% \quad (\text{at confidence of } 95\%)$$

Likewise, the standard deviation of Q is

$$\frac{\sigma_Q}{Q} = \left[\left(\frac{\sigma_m}{m} \right)^2 + \left(\frac{\sigma_t}{t} \right)^2 \right]^{1/2} = \left[(0.1)^2 + (1)^2 \right]^{1/2} = 1.00\%$$

The estimate for the single-sample precision uncertainty in Q is

$$\frac{P_Q}{Q} = \frac{1.96\sigma_Q}{Q} = 1.96(0.01) = 1.96\% \quad (\text{at confidence of } 95\%)$$

So the total uncertainty in Q is

$$\frac{U_Q}{Q} = \left[\left(\frac{B_Q}{Q} \right)^2 + \left(\frac{P_Q}{Q} \right)^2 \right]^{1/2} = \left[(0.005)^2 + (0.0196)^2 \right]^{1/2} = 2.02\% \quad (\text{at confidence of } 95\%).$$

References

1. Beckwith, T. G., Marangoni, R. D. and Lienhard, V, J. (1995). *Mechanical Measurements*. Addison-Wesley Publishing Company, New York.